OPTICAL METROLOGY OF ADAPTIVE MEMBRANE MIRRORS

THESIS

John W. Wagner, Captain, USAF

AFIT/GA/ENY/00M-05

DEPARTMENT OF THE AIR FORCE

AIR UNIVERSITY

AIR FORCE INSTITUTE OF TECHNOLOGY

Wright-Patterson Air Force Base, Ohio

APPROVED FOR PUBLIC RELEASE; DISTRIBUTION UNLIMITED

20000803 147

AFIT/GA/ENY/00M-05

OPTICAL METROLOGY OF ADAPTIVE MEMBRANE MIRRORS

THESIS

Presented to the Faculty of the School of Engineering and Management

of the Air Force Institute of Technology

Air University

In Partial Fulfillment of the

Requirements for the Degree of

Master of Science in Astronautical Engineering

John W. Wagner, B.S., M.A.
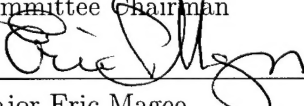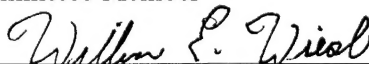
Captain, USAF

March 2000

AFIT/GA/ENY/00M-05

OPTICAL METROLOGY OF ADAPTIVE MEMBRANE MIRRORS

John W. Wagner, B.S., M.A.

Captain, USAF

Approved:

(signature)	_9 Mar 00_
Captain Gregory Agnes	Date
Committee Chairman	
(signature)	_9 MAR 2000_
Major Eric Magee	Date
Committee Member	
(signature)	_9 Mar 00_
Doctor William Wiesel	Date
Committee Member	

Acknowledgements

When I first discussed proposed thesis topics, I was given some advice to follow an established topic and avoid starting a research project. If I had followed this advice, I'm convinced there would have been more time for other schoolwork and family, but I would not have enjoyed this "first-ever" research. This effort would not have been possible without the help and support from several people. My advisor, Capt Agnes, provided program direction, support, and many incremental reviews which kept this effort productive. This program involved many academic areas and departments, and in all cases support was outstanding from the AFIT staff. The aero/astro laboratory staff, Mr. Jay Anderson, Mr. Bob Bacon, Mr. Dan Rioux, and Mr. Andy Pitts ordered needed parts, provided insight into material selection, and Dan's expertise in sub-micron polishing was utilized extensively on each membrane mounting ring. From the physics laboratory staff, Mr. Greg Smith provided interferometry advice, while Ms. Belinda Johnson, along with Mr. Jack Janning of JLJ, Inc., spent many hours developing the unique photoetching technique used for this PVDF film. From electrical engineering, Mr. Charles Powers provided lab space and room support, Mr. Bill Trop developed photomasks, and Mr. Joe Shaw developed a unique power source for the quad-square etched membrane. Mr. Russ Hastings of the AFIT model shop produced simply outstanding test tools from difficult schematics, and was able to accommodate every design revision.

I would especially like to thank the current "think tank" for membrane research, AFRL/DE, Mr. Dan Marker, Mr. Richard Carreras, and Dr. Jim Rotgé for providing aluminum coated Upilex, stretching ring designs, and research support. Dr. Rotgé provided continual guidance with system image formation, which was critical to this effort and much appreciated.

Finally, I would like thank my family for their understanding and support during this period. Jennifer, Jeff, and Jake, I thank you for providing the motivation each day to do my best, and I look forward to our "normal" life someday.

<div align="right">John W. Wagner</div>

Table of Contents

List of Figures

ix

List of Tables

AFIT/GA/ENY/00M-05

Abstract

Current space-based imaging platforms are significantly constrained in both size and weight by the launch vehicle. Increased payload size and weight results in increased cost and a decrease in launch responsiveness. The USAF Scientific Advisory Board (SAB) identified "Large lightweight structures for optics and antennas" as a revolutionary primary technology to be developed for the Air Force of the 21st Century. A membrane primary mirror in a space-based imaging system has the ability to overcome current payload constraints and meet evolutionary needs of the future.

The challenge of membrane optics in space is the process of implementing adaptive optics technology to the membrane surface that will provide at least rough order of magnitude imaging, where small aberrations can be removed downstream in the system.

The objective of this research was to develop a system to categorize surface properties of optical quality membrane material with the ability to interpret membrane mirror deformation. Coincident with this objective was the design and construction of membrane mirrors and associated test tooling, the design and application of in-plane zonal control for membrane mirrors, and mirror deformation analysis. The system provides wavefront analysis with both optical interferometry and Shack-Hartmann wavefront sensing, with good correlation, which compares favorably to Zygo interferometer data. Results from membrane static testing will be presented.

OPTICAL METROLOGY OF ADAPTIVE MEMBRANE MIRRORS

I. Introduction

1.1 Overview

Mankind has improved its quality of life dramatically by exploiting the advantages of placing objects in earth orbit. Satellites have saved countless lives by providing advance storm warnings of powerful hurricanes such as Andrew (1992), Opal (1995) and Floyd (1999). Andrew was the third most intense hurricane to strike the United States in the 1900's and the most expensive natural disaster ever in U.S. history ($26.5 Billion), but with advance storm warning from satellites, thousands of people escaped what would have been a deadly result. Although over 250,000 people were left temporarily homeless in Florida's Dade County, only 26 deaths were reported from the direct effects of Andrew(35). Prior to the extensive advance warning and continuous tracking offered by satellites, thousands were killed by significantly less powerful hurricanes, such as the 8000 people who perished in a 1900 hurricane which hit Galveston, Texas (35). In addition to safety, satellites improve our ability to communicate, navigate, study our Earth's resources, peer into the origins of the universe, and provide significant contributions to national security.

The ability to monitor potential adversaries is a critical satellite mission for the United States. To the United States Air Force, the goal is "Global Awareness" – to see in near real time everywhere on the surface of the Earth or in the air or near space, where any potential adversaries will know that they are under continuous surveillance at all times and under all conditions (7). This rapid flow of information and global coverage involves a presence that can only be realistically undertaken with satellites and space systems. Many systems have been built to monitor the environments both on the Earth and away from

1-1

the Earth. However, all operational systems have been constrained by the size and weight that the launch vehicle could place in orbit. Given size and weight constraints, to obtain the needed performance requirements involves significantly increased monetary costs and time to orbit.

The Hubble Space Telescope required the space shuttle to take it to orbit, and was constrained to an aperture of 2.4 meters by the diameter of the Shuttle cargo bay. It took a significant amount of time to grind and test the mirror to a 0.06μ m peak-to-valley surface roughness, cost \$1.6 billion to build, and the system was significantly flawed when deployed in 1990 (6). After repairs were made in 1993, Hubble produced profound images and continues to provide vast improvements over traditional terrestrial based astronomy. However, imagine the increase in performance if a significantly larger aperture could be used and its mirrors were controlled by adaptive mirror technology. There would be virtually no mirror grinding/polishing time, and earth observing satellites could be produced, stored, and launched on demand. Each satellite would be adaptable to any situation, could have significantly larger imaging surfaces, and be completely controlled with electronically actuated surfaces. The number of imagers on orbit could grow with the associated decrease in production costs of each satellite, providing a true "Global Awareness," and is the impetus behind the current push in large lightweight mirror technology.

This current push is due largely to recent developments in lightweight adaptive "membrane" optics. While these surfaces are relatively new in their use as optics, researchers have been testing inflatable deployable space structures since the late 1950's. Inflatable structures provide low cost flight hardware, high mechanical packaging efficiency, deployment reliability with low weight, and low associated launch costs – significant advantages over traditional hardware (12). Research and development into large inflatable apertures began in the late 1970's, funded by the U.S. Department of Defense and to a lesser extent by NASA, after micrometeoroid flux in space determined to be at least three orders of magnitude smaller than originally thought (4). In-flight tests of inflatable systems include the Echo balloon series in the 1960's, ballistic missile re-entry vehicle decoys in the sixties and seventies, the Contraves antennae and sun shades in the early 1980's, and the L'Garde Inflatable Antenna Experiment (IAE) in 1996.

Echo was NASA's first communications satellite project, and the first inflatable space-craft. It was essentially a reflective balloon which bounced incoming radio waves back to the earth, consisting of a 100 ft. diameter sphere made of aluminized polyester and inflated after it was put in a 800-900 nautical mile orbit. Two-way voice links "of good quality" were set-up between Bell Laboratories in Holmdel, NJ and the NASA station at Goldstone, CA (15). The next series of inflatables were inflatable re-entry vehicle (RV) decoys that were designed by the USAF to confuse the Soviet Antiballistic Missile (ABM) systems in the late 1960's. Fully instrumented inflatable RV decoys were successfully launched between 1968 and 1972 (4). More recent flexible/inflatable projects were conducted overseas, with the European Space Agency (ESA) sponsored development of reflector antenna and sunshade concepts. Offset reflectors for mobile communications and sun shade support structures for telescopes and large sensors were built and demonstrated in the late 1980's in sizes up to a 10x12 meter reflector antenna for land mobile communications (4).

These demonstrations have proven the viability of flexible and inflatable structures on orbit. Although these structures have been under study for forty years, only recently have thin membrane structures been designed and manufactured with geometric precision (11). The IAE (Figure 1.1) was the first concept to demonstrate a level of mature structures technology that could enable large imaging missions. An office desk sized container (7x3x1.5 ft) on the reusable NASA Spartan spacecraft was released from the space shuttle Endeavor on May 20, 1996. This container deployed the IAE after the shuttle backed away to a safe on-orbit distance, where struts inflated to 92 feet connected a dish which inflated to 50 feet in diameter (8). This dish was actually a 14 meter inflatable reflector with a designed surface precision of a few millimeters root-mean-squared (RMS) surface deviation supported by a 50 foot diameter inflated torus. The significance of a structure this large having an excellent surface precision of 1.5 mm RMS in the central eight meters of the aperture, was enough to initiate a strong interest in large inflatable membrane structures for use in space.

There have been several recent research developments in the field of membrane optics since the IAE demonstration. Surface quality measurements of 0.05λ RMS ($\lambda = 633$nm), or 31.7 nm deviation from a planar reference, correction of membrane aberrations by

Figure 1.1   Inflatable Antenna Experiment, STS-77

real-time holographic compensation, development of rigidization techniques for structural stiffness, and development of numerical tools for the study of pressurized axisymmetric membranes are some recent significant developments (23, 17, 12). The next logical step in the development of a membrane imaging system is active surface control of the membrane surface.

The USAF Scientific Advisory Board (SAB) identified "Large lightweight structures for optics and antennas" as a revolutionary primary technology to be developed for the Air Force of the 21st Century (7). More specifically, the SAB stated:

> A candidate solution to the current technology shortfall is to relax optical tolerances on the primary mirror... The primary collector might be non-rigid (floppy), monolithic or segmented, filled or sparse. It could be a very thin Mylar surface stretched over a skeleton structure that could be deployed like an umbrella. (7)

The SAB candidate solution could be pursued for a space image collection system. However, future system optical tolerances will logically become more stringent, a requirement that does not coincide with the inherent distortions of a membrane as a primary imaging optic. Any primary mirror distortion must be corrected downstream in the system. Further, operational spacecraft are subject to a variety of internal and external disturbances which would degrade an optical imaging platform. Therefore, if membrane structures are to

be utilized operationally for imaging surfaces, they must provide rough order of magnitude optical images–requiring a controllable membrane surface.

1.2 Problem

The challenge of membrane optics in space is the process of implementing adaptive optics technology to the membrane surface that will provide at least rough order of magnitude imaging (where small aberrations can be removed downstream in the system) and suppression of on-orbit vibrations to maintain a stable imaging platform. A candidate solution providing a controllable membrane surface is in-plane piezoelectric material such as polyvinylidene flouride (PVDF). To assess the performance of this material, experiments must be conducted which address both static and dynamic material surface properties.

1.3 Scope

The objective of this research involves the design and construction of a system that will categorize surface properties of optical quality membrane material and be able to interpret membrane mirror deformation. Coincident with this objective is the ability to understand the wavefront evolution through the system, the design and construction of membrane mirrors, the design and application of in-plane zonal control for membrane mirrors, and mirror deformation analysis.

The scope as identified above may seem large, as this thesis bridges many technical fields and requires the design and construction of not only an optical non-contact measurement system from scratch, but all the supporting hardware as well. This thesis, however, is a "groundbreaking" for AFIT in this new and promising research field. It is hoped that this thesis and the system(s) designed and built for this thesis, will add to and consolidate recent advancements in this field and provide both the U.S. Air Force and AFIT with a consolidated platform to further research in the high-payoff area of adaptive membrane mirrors.

1.4 Summary of Thesis

This thesis is organized as follows: Chapter 1, Introduction; Chapter 2, Review of the Relevant Literature; Chapter 3, Optical Wavefront Description; Chapter 4, Imaging System and Membrane Mirror Construction; Chapter 5, System Performance Results; Chapter 6, Conclusions and Recommendations; Bibliography.

The first chapter outlines the importance of this work to the U.S. Air Force and the benefits of pursuing this technology. Research into this field has the ability to significantly decrease the size and weight of space launch payloads while enabling satellite imaging systems with apertures orders of magnitude larger than any currently on orbit.

The second chapter mainly outlines recent advancements in the field of membrane optics while touching on past developments in inflatable systems and holographic correction systems which would be necessary elements of an imaging system with a lightweight membrane as its primary mirror. Chapter Two also discusses PVDF film properties and applications. No research was found which attempted to optically determine the deformation of a non-pressurized thin film membrane under PVDF control. Therefore, this thesis presents the first-ever testing and analysis of this type of surface.

Chapter Three delves into basic optical theory from refraction and reflection to interference, and begins with Maxwell's equations. This chapter was intended to provide the reader with the necessary theoretical understanding of wavefront propagation and interference. It does not substitute for optical texts, but may serve as a quick reference which bridges physical, geometrical, and adaptive optics.

Chapter Four provides subsystem hardware descriptions, functions, and placement within the system. It also discusses the test tools designed and developed for optical membrane tensioning and assembly. Calibration of the system is reported in Chapter 5, along with membrane imaging results. Conclusions and recommendations follow in Chapter Six.

II. Review of the Relevant Literature

2.1 Overview

Literature relevant to membrane mirror technology dates to the beginning of the space program with the inflatable Echo balloon series in the 1950's. Membrane and inflatable-type structures for support provide significant advantages to denser materials for satellite construction or space exploration by providing a greater capability within the size and weight limitations of space launch vehicles, inherently providing reduced launch costs, and enabling high-performance missions originally not feasible utilizing traditional technology. Examples include aggressive space missions involving components considerably larger than available launch cargo compartments: large space station components, large solar energy collectors, and large components for future Moon and Mars exploration (31).

Large, lightweight imaging platforms is an area of high potential payoff for membrane and inflatable technology. The use of a reflective membrane as the primary mirror in a space-based telescope is being explored. However, membranes present additional problems due to their flexible nature, which cross traditional engineering disciplines. The Air Force Research Laboratory (AFRL), Directed Energy (DE) directorate, found that even the terminology between the disciplines in membrane construction (optical, mechanical, and materials engineering) is different in each respective discipline and the scientific impact of a term in one field is not exclusive to that field (30). For example, surface roughness to a materials engineer is on the order of a millimeter, while surface variations to an optical engineer are on the order of a wavelength. Key questions in the new field of membrane research, such as minimum in-plane stress to achieve optical quality membranes, have only begun to be answered (30). Membranes have not been pursued as viable imaging technology until recently, due to aberrations resulting from the lack of structure, edge effects/wrinkling, thermal expansion, and local surface deformation, each with the ability to significantly degrade imaging capability.

Fortunately, adaptive optics has advanced steadily over recent years. The discipline of adaptive optics was developed to correct aberrated wavefronts, employing many of the same

mechanisms which cause wavefront errors. Many methods can be utilized for wavefront correction, including distorting another mirror to compensate for the variations in the wavefront (roughly illustrated in Figure 2.1), conjugating and thus correcting local index
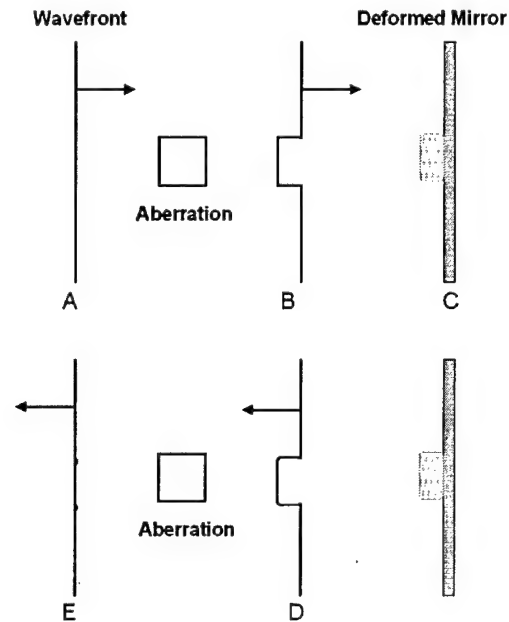
Figure 2.1   Wavefront Distortion and Correcting Mirror (Adapted from (42))

of refraction variations (corrective eyeglasses use this principle), or adding a correcting device to the primary mirror (42).

Mirror deformation in adaptive optics traditionally involves electromagnetic devices such as piston actuators on either continuous or segmented mirrors (Figure 2.2), piezoelectric ceramics, solenoids, or even wormgears (42). However, these systems involve added weight and complexity over the polished rigid primary mirrors used in space. Over the past fifty years, several contributing technologies have evolved to provide the technology base for membrane mirror research, enabling the capability for orbital membrane mirror operations. The literature relevant to this research is focused in three main areas: inflatable systems, membrane surfaces, and holography. Other literature research involved in wavefront propagation and analysis is reviewed and referenced in Chapter 3.

Mirror Plates

Actuators
in Piston

Actuators
in Piston
and Tilt
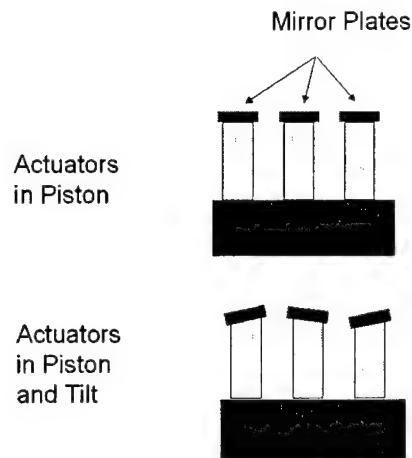
Figure 2.2   Segmented Adaptive Mirror

2.2 Inflatable Systems

2.2.1 Inflatable Characteristics.

Inflatable satellite technology has been the target of an increasing amount of research and development by the United States, representing a resurgence of this technology which was incorporated into some of the very first U.S. satellites in the early 1960's (Echo I, Explorer IX, Explorer XIX, Echo II, and Pageos I) (5). Inflatable devices represented the only way to put satellites of any size in orbit due to the limited capabilities of launch vehicles, even though inflatable technology was immature. According to Cassapakis (5), the U.S. Department of Defense investigated the use of inflatable space decoys for a variety of systems, and were found to be the optimum choice among various systems for the following reasons:

1. The typical weight reduction was 50% over the best competing mechanical system.

2. An inflatable can be packaged in a small volume, typically less than 25% of a mechanical erectable structure.

3. The inflatable structure is inherently strong. Inflatables are able to absorb loads over a large surface area, while mechanical systems typically have loads concentrated in points which must then be reinforced.

4. The inflatable has low production cost, with inexpensive tooling.

5. Inflatable systems have a high reliability of deployment.

6. Inflatables are easily adapted to symmetric shapes and curved surfaces in response to the inflation pressure.

7. Favorable dynamics exist for inflatables, as they are against a nearly constant restoring force (inflation pressure).

8. Inflatables have a favorable thermal response with large opposing continuous surfaces, with very low coefficients of thermal expansion in new polymers.

If inflatables and lightweight membranes offer so many advantages for use in space, and are simple and efficient, why do we find only a limited use of these systems today? Reasons given by Mikulas and Thomson (31) point to the industrial difficulty in fabricating high precision components from thin polymers/fabrics and the inherently high coefficient of thermal expansion in polymers. Further, Cassapakis (5) reported the most probable reason for the turn to mechanical systems from the inflatables in the early days of the space program was because it was the easy (though not optimum) solution – the tools to analyze large mechanical deployables existed, there were many engineers skilled in developing mechanical structures, and the micrometeoroid threat was unknown. However, improvements in fabrication and polymer research over the past few years, driven by a "faster, better, cheaper" way to overcome high launch costs, are leading to a resurgence in these systems. Satter and Freeland (39) mention that while inflatable structures have been identified as the "best new and innovative concepts" (in 1995), organizations such as L'Garde, Inc., Contraves, SRS, Aerospace Recovery Systems, ILC Dover, and Thiokol, have only recently demonstrated the design and manufacture of thin membrane structures with enough precision to be seriously considered for operational application.

Characteristics of inflatables, as presented by Mikulas and Thomson (31), fall into two major categories: pressure stabilized and rigidized. Pressure stabilized systems (or "balloon" type systems) are characterized by low weight and volume, giving orders of magnitude lower weights than mechanical structures, as the weight of a large inflatable system is usually calculated only by the weight of the film used (typically 80 percent of

the total weight). Pressure systems have additional benefits: they can be pre-flight tested on Earth using a light gas, they are storable and reliable on-orbit, and their dynamic response is not prone to resonance problems of traditional structures. Pressurized systems provide surface accuracy, as pressure removes local surface discontinuities, "perfecting" the surface. These systems have been demonstrated to 0.1 mm RMS. Pressure leakage caused by impacting space debris can be compensated by make up gas or by using high strength Kevlar coated with teflon for gas retention (31).

Rigidized inflatable systems are deployed by inflation and rigidized once in-space. Useful for structural elements, these systems are attractive by combining high material strength with no need for makeup gas. Mikulas and Thomson (31) point out two rigidizing techniques. The first involves a space-curing resin, where a chemically reactive layer is placed on one or both sides of the inflatable by impermeable films and cured either in a vacuum (space) by an ultraviolet light cure method. The second uses gelatin/fabric composites where a carrier (fabric) is impregnated with a specially formulated gelatin which rigidizes when the solvent (usually water) is evaporated from the gelatin. The gelatin/fabric process is considered reversible, as flexibility may be re-introduced after treating the rigid structure with water. Many of the above systems are currently being explored for space station use (31).

When considering inflatable technology for optical surfaces, there is a choice between a uniform inflatable element or modularized elements composed of inflatables. The single inflatable element has good packaging efficiency, but very accurate manufacturing is required, shape control is difficult, and the surface RMS error increases as the size of the reflector increases. A modularized inflatable reflector structure for optical imaging was chosen for investigation by Kato, Ohnishi, Muragishi, and Natori (24) in 1990, using nineteen cells on a 10 meter aperture, with hexagonal elements of about 2 meters. Their modular system utilized a deployable hexagonal statically determinate planar truss backup structure which provided shape correction of the reflector surface . Surface RMS error was reported as "sufficiently small" by using a non-contact sensor, but actual RMS values are unclear.

2.2.2 Inflatable Space Applications.

Satter and Freeland discussed the potential applications of inflatable structures in their 1995 paper to a variety of potential missions at that time, a few of which are summarized below (39):

- RF Interferometry: ARISE (Advanced Radio Interferometry between Space and Earth) is a concept for utilizing orbiting antennae (30 meter class) along with ground antennae to synthesize a highly sensitive RF interferometer with an effective baseline larger than the Earth's diameter to achieve high angular resolution of distant RF astronomical sources. The high precision required and resultant high weight of traditional mechanical structures would render this mission unfeasible. With inflatable technology advances, including resistance to micrometeoroids and low temperature rigidization techniques, this mission is made possible.

- Synthetic Aperture Radar (SAR) Mapping: Conventional mechanically deployable arrays require complex deployment and large rigid panels for support of the active array elements. The large stowed dimensions and high mass of these arrays also lead to a requirement for large launch vehicles. A concept known as LightSAR utilizes simple straight inflatable tubes supporting a flexible SAR array which can be folded for launch.

- Outer Planet Exploration: A solar power antenna combines the functions of a solar concentrator and RF communications antenna into a single aperture. However, the apertures required to provide sufficient spacecraft power with solar concentration can be up to 40 meters in diameter. This requires large, lightweight inflatable apertures with smooth, highly stressed reflector membranes and high reflectivity coatings, along with a precision, low-temperature rigidizable support structure.

Lou, Feria, and Huang explored the development of inflatable space SAR at the Jet Propulsion Laboratory, to the point of successfully fabricating, assembling, and ground testing a $\frac{1}{3}$ scale model with a roll-up inflatable SAR through NASA's Advanced Radar Technology Program (ARTP). Major components of this system include an inflatable frame made of four-inch diameter Urethane coated Kevlar tubes, a catenary tensioning system with Mylar cords and Kapton tape, Novaclad films with RF patterns formed by etching the copper coating of the Novaclad film, a central support platform of honeycomb panels and

aluminum core, and an inflation system supplying 5 psi to the inflatable tubes (27). Radar range test on this model show that excellent RF performance is achieved at significantly reduced mass and launch volume.

2.2.3 Inflatable Technology Demonstration.

An in-space demonstration of inflatable technology was conducted in 1996 with the L'Garde, Inc. Inflatable Antenna Experiment (IAE). Selected by NASA for an In-Space Technology Experiment Program (IN-STEP) flight demonstration, this program had three basic objectives (45):

1. Validate the deployment of a 14-meter diameter, inflatable, deployable offset parabolic reflector antenna structure in a zero-gravity environment

2. Measure the reflector surface precision (1-mm RMS goal) for several different sun angles and inflation pressures in a realistic thermal environment

3. Demonstrate a large size flight-quality structure can be built for a low cost and that it can be stowed in a very small container

The orbital sequence was designed to place the Spartan recoverable spacecraft carrier (containing and powering the IAE) in orbit with the space shuttle's remote arm. Once spacecraft attitude was stabilized by the Spartan attitude control system, the experiment was initiated by opening the cargo doors and allowing the spring loaded ejection plate to push the stowed inflatable structure from the canister. Nitrogen gas would then provide inflation to the structure. Due to high drag of the 14 meter structure and resultant increased separation from the shuttle, only one orbit was designed for the experiment. After one orbit, the IAE was ejected for re-entry and the Spartan carrier was recovered by the shuttle.

The deployment of the IAE on-orbit did not occur as designed due to an unpredicted amount of residual air in the stowed structure, which resulted in a near instant expansion of the torus (11). Additionally, the gas inflation system malfunctioned, resulting in only partial inflation which did not stretch the membrane reflector structure enough to allow measurement of the surface. However, the antenna support structure achieved complete deployment and maintained its configuration for the duration of the experiment. Further,

the deployment did not damage the antenna – indicating its degree of robustness, the interaction between a large inflatable and the space environment was established, and the mission was declared a success (11).

2.2.4 *Inflatable Gore Prediction Code and Surface Measurements.*

In conjunction with the IAE, L'Garde developed a finite element code to predict the on-orbit static and modal dynamic performance of inflatable antennae and inflatable solar concentrators. This code, called Finite Element Analysis of Inflatable Membranes (FAIM), is a geometric nonlinear finite element solver with nonlinear material capability interfaced to a RF antenna code, a ray-tracing code, and graphical processors which can predict the overall performance of membrane antennae and reflectors (33). Palizoc and Huang mention that the major question that must be answered in inflatable mirror development is, "What must be the initial shape of an inflatable shell structure such that it attains a smooth parabolic surface after experiencing large structural deformations(33)?" This "inverse" problem helps to develop preshaped gores which are joined to create the inflatable membrane. Palizoc (33) states an excellent comparison between FAIM to an analytical solution for a symmetric paraboloid.

L'Garde inflatable surface accuracy has been measured on many inflatables of varying diameters using a photogrammetric technique where tiny reflective targets on surface grid points are photographed from many positions around the reflector. The company discovered that surface errors consistently follow a nearly symmetric pattern resembling the script letter W (4). This cosinusoidal error pattern as a function of aperture radius results in a simple RMS error (ε) of the peak-to-peak deviation divided by $2\sqrt{2}$. L'Garde measured experimental antenna tests at microwave frequencies on a paraboloid 3 meters in diameter in an anechoic chamber at the Lockheed-Martin Denver laboratory in 1996, showing a close match to the Ohio State reflector antenna computational code (NECREF) and predictions using John Ruze's well known gain degradation due to surface roughness. The degradation equation was given by Ruze as (36):

$$G = G_0 e^{(-\bar{\delta}^2)} = \eta(\frac{\pi D}{\lambda})^2 e^{-(\frac{4\pi\varepsilon}{\lambda})^2} \tag{2.1}$$

where G is the gain degradation due to surface roughness from optimum gain G_0, η is the aperture efficiency (assumed unity with uniform illumination), D is aperture diameter, ε is the effective reflector tolerance, or RMS surface error on a shallow reflector (large $\frac{f}{d}$) which produces the phase front variance $\bar{\delta}^2$. L'Garde calculated a 1.6 mm RMS surface roughness with usable frequencies up to 7 GHz, and a loss not exceeding 1 dB (4).

2.3 Membrane Surfaces

2.3.1 Membranes as Space Reflectors.
Extremely thin surfaces are well known for their use in space reflector application. Mikulas and Thomson discuss the mesh material that was used as the reflector surface on most moderate precision reflectors, in sizes up to large 10 meter apertures such as the Russian deployed rib/mesh antenna on Salut 6 and the 30 foot diameter wrap-rib antenna made by Lockheed for the ATS-6 spacecraft. Mesh is considered useful for radio frequency (RF) antennae up to 30 or 40 GHz (31).

While useful for RF, mesh is not feasible as optical reflectors. A low-loss high-frequency reflecting surface must be solid, such as mirrors, panels, or reflective membranes. Of these three choices, Mikulas and Thomson mention membranes providing the most promise as they can be excellent reflectors, are pliable, and can be compacted for launch. Currently, the most prevalent approach of providing a deployable solid surface is to use an assembly of stiff panels (31). Many different concepts are undergoing development to optimize hinging, folding, stacking, and deploying these panels.

Stiff panels, however do not provide either the packing efficiency or weight reduction of a membrane surface. The three current primary methods for achieving a precise parabolic membrane shape are (2):

1. Casting a polymer film into an initially curved shape that deviates slightly from a parabola, so a slight inflation pressure will deform the membrane into the proper shape.

2. Seaming together many flat gores (similar to parachute construction) with precisely calculated shapes, and inflating.

3. Deforming Use an initially flat membrane, reducing the manufacturing variables.

The Air Force Research Laboratory (AFRL) uses the initially flat membrane for evaluation. The shape of this structure can be approximated for a Poisson's ratio of 0.4 as (2):

$$w = w_0(1 - 1.26\frac{r^2}{a^2} + 0.259r^4a^4) \tag{2.2}$$

where w is the deflection of a point at distance r form the center, a is the diameter of the membrane, w_0 is the deflection at the center, and the fourth-order term represents the undesirable deviation from a parabola, which could be corrected with adding control strains by piezofilms, shape memory alloys, etc.

2.3.2   Membrane Shape Prediction.   Shape correction in membrane imagery is required. Freeland states, "Precision space reflector applications are associated with accuracy beyond the customary tolerances of structural engineering" (12). There are many causes of surface error in membranes not present with stiff structures, some of which were mentioned in section 2.1, with a more complete list below (12):

- Material stiffness properties and areal variation

- Material thickness and areal variation

- Creep

- Moisture effects

- Material "wrinkling" or creasing due to handling and packaging

- Irregularities in the film fabrication process

- Analytical shape prediction

- Edge support (boundary) conditions

- Membrane inflation level

- Thermal distortions

- Gravitational effects in Earth testing

Freeland identified analytical shape prediction as an error source due to the difficulty in numerical analysis, with classic solutions existing for only the simplest configurations. Further, he stated that classic solution options are not well understood due to the approximations made to facilitate exact solutions (12). Computer algorithms have been written to model membrane deformation, which compare well with experimentation, using numeric shape solver iteration methods calculating the loaded shape, stress and strain state, determining the position of a point from the known adjacent point, and also include Hencky's (1915) approach to using a power series solution of a homogeneous isotropic linear elastic circular membrane under lateral pressure (12).

Freeland describes a software package called AM (Axisymmetric Membrane) which follows this method to model wrinkling and determining initial shapes which inflate to the desired pressurized system, and states the accuracy of AM surpassing RF applications with a precision applicable to optical frequencies (12). Results from this program were compared to other finite element analysis programs, FAIM and NASTRAN, with good correlation. Another program, a genetic algorithm by Bishop (2), was written to manipulate the boundary conditions and inflation pressure in an attempt to correct for shape aberrations caused by a thinned-out portion of the membrane. Modifying original software designed to optimize the placement of viscous dampers in trusses, this software models the system with a fourteen-digit chromosome, where the first thirteen define displacement at associated springs attached to the edge of the membrane. The algorithm found five comparably performing designs, and could be used to tailor boundary conditions to increase performance.

2.3.3   Membrane Shape Correction Using Piezoelectric Polymers.

On-orbit shape correction of inflatable membrane structures using piezo induced deformations was investigated in 1994 by Salama, Kuo, Garba, Wada, and Thomas. Experiments were conducted to study the local deformation in an inflatable membrane using piezoelectric deformation, or mechanical deformation of the material with an applied voltage. Piezoelectric material would optimize reflector performance in an inflated membrane after global focal length adjustments were made by adjusting the inflation pressure.

The Salama paper provides a concise picture of piezoelectric actuation. Piezoelectricity couples the electrical and mechanical properties of certain materials which have positive and negative dipoles. Polymers, for example, are composed of many randomly oriented dipoles which are permanently poled by application of a high voltage at high temperature. This locks in the piezoelectric effect along the poling direction. The coupled electromechanical relations take the general form (37):

$$D_k = d_{klm}^T \sigma_{lm} + \eta_{kn}^{\sigma\ T} E_n \tag{2.3}$$

$$\epsilon_{ij} = s_{ijlm}^{E\ T} \sigma_{lm} + d_{ijn}^T E_n \tag{2.4}$$

where D is the dielectric displacement vector, σ is the stress tensor, E is the electric field, d is the piezoelectric coefficient matrix, η is the permittivity, ϵ is the strain tensor, s is the elastic compliance. Superscript T indicates transpose, and other superscripts indicate that the coefficient in question is evaluated at a constant value of the superscript. We see in the second equation the strain tensor depends on the stress tensor and the electric field through the elastic compliance and the piezoelectric coefficients.

Salama measured piezoelectric film deformation with eddy current sensors, and recorded lateral membrane deformation at inflation pressures ranging from 0.1 to 0.5 psi, finding deformation ranging from 0.1μm to 0.09μm, with a larger rate corresponding to lower inflation pressure. Their numerical analysis involved the comparison of piezoelectric strains ($d_{31}E_3$ and $d_{32}E_3$ in equation 2.4) to thermal strains of the form $-\alpha_{31}\Delta T$ and $-\alpha_{32}\Delta T$, where ΔT is the change in temperature and α_{31} and α_{32} are the anisotropic expansion coefficients in the 1 and 2 directions (37). Salama computed deformation iteratively, finding a good correlation between test, computational, and analytical analysis as shown in Figure 2.3, and displacement vs. drive voltage as shown in Figure 2.4. From this figure, the maximum displacement recorded by Salama was 0.001", or 25.4 μm.
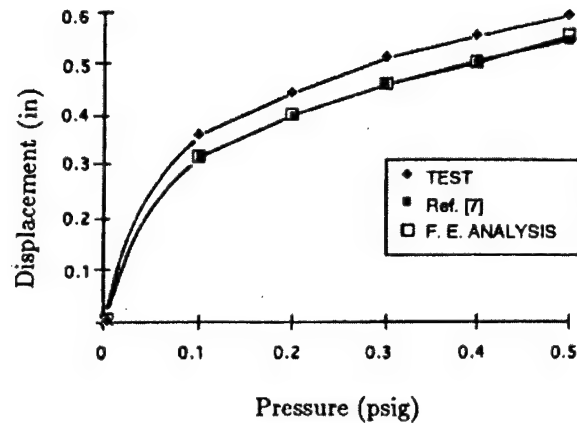
Figure 2.3   Test, Analysis, and NASTRAN computation of Inflated Circular Membrane
(37)
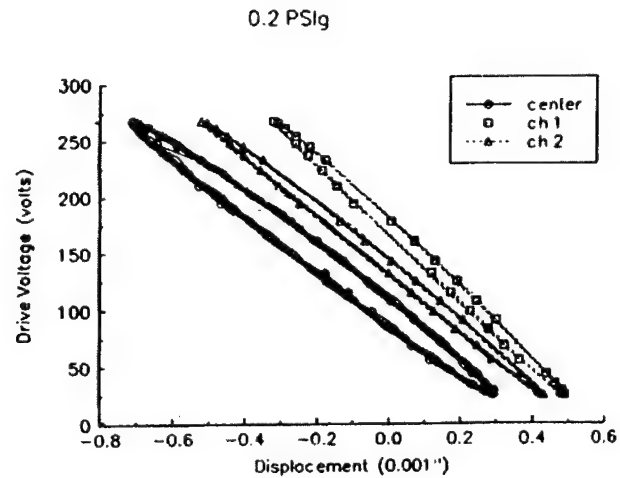
Figure 2.4   Piezoactuated (PVDF)Deformation of 0.2 PSIg Inflated Circular Membrane
(37)
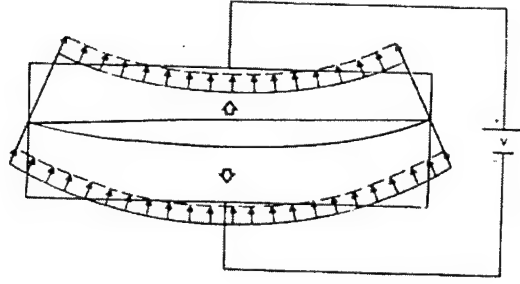
Figure 2.5   Voltage Application and Resultant Bending of PVDF Bimorph (26)

Two thin sheets of lightweight piezoelectric polymers such as polyvinylidene flouride (PVF_2 or PVDF), known as a bimorph, were analyzed by Kokorowski, where the metallic coating on one surface of the bimorph enables a controllable optical element and also served as the optical surface. With two pieces bonded with opposite polarities, for an applied voltage as shown in Figure 2.5, the contraction of the top element and the expansion of the bottom element will cause a bending effect, while the thickness change will be opposite in each sheet, causing a zero net change in bimorph thickness. Kokorowski describes the basic equations that govern the electro-mechanical behavior of piezoelectrics are thermodynamic equations of state (26):

$$T_i = C_{ij}^D S_j - h_{ni} D_n \qquad (2.5)$$

$$E_m = -h_{mj} S_j + \beta_{mn}^S D_n \qquad (2.6)$$

where i and j are indices running from 1 to 6, m and n run from 1 to 3 (x to z), h_{ni} are piezoelectric constants, T_i and S_j refer to the components of the stress and strain tensors, and E_m and D_n refer to the components of the electric field and the electric displacement field. These two matrix equations represent 9 equations with 18 unknowns, which is reduced by simplifying assumptions. Kokorowski derived the relationship between the displacement of the middle surface of the PVDF and the applied voltage as:

$$\bar{\nabla}^2 \psi_0(x, y) = -(\frac{4}{\alpha_0 h^2}) \phi(x, y) \qquad (2.7)$$

where $\psi_0(x,y)$ is the displacement of the middle surface, $\phi(x,y)$ is the electric potential at the top surface of the bimorph (found by integrating the electric field), and α_0 is a constant defined for convenience which includes five independent elastic coefficients.

Sato, Ishida, and Ikeda developed a deformable mirror system using single sheet, or "unimorph", PVDF film and a laminar glass mirror cut into a triangular shape with base and height of 25 mm. Deformation of the optical surface was measured with collimated He-Ne laser light reflected by the mirror and passed through a holographic spatial filter to generate precise wavefronts. After compensation by holographic filter, deformation values were obtained using a lest-mean-square error estimation (38). Maximum recorded deformation was 20 μm from a 500 Volt input.

2.3.4 Membrane Surface Quality and Strain Requirements.

AFRL has demonstrated membrane surface roughness to be less than one micron over an eleven inch diameter surface, using a Twyman-Green and a Zygo interferometer to generate and interpret interference fringes (23). Two membrane materials were analyzed by AFRL: Upilex, a polyimide film made by UBE Industries, Ltd., and a membrane material made by SRS, Inc., which produced the best surface flatness numbers (23). With these materials, the AFRL group deformed an initially flat membrane into a parabolic shape using two different techniques. The first involved pre-strain of the membrane and an applied central vacuum, while the second used a plunger to deform the center of the membrane along the optical axis (48). The membrane was mounted over two concentric rings, as illustrated in Figure 2.6A. Membrane pre-strain was created by reducing pressure in the annulus region (Figure 2.6B). With adequate pre-strain, the membrane surface was pulled radially taught which decreased surface roughness. Vacuum was then applied to the central region, which produced a near-spherical shape. The pre-strain, which created a uniform biaxial strain state in the central region of the membrane had the effect of removing the "sags" in the central region near the inner ring which added aspherical components. The group found the membrane final shape to be sensitive to a variety of mechanical influences. To achieve planar membrane shape, both rings were coplanar and the surfaces of the mounting rings were manufactured to optical tolerances. Using Upilex membrane film,
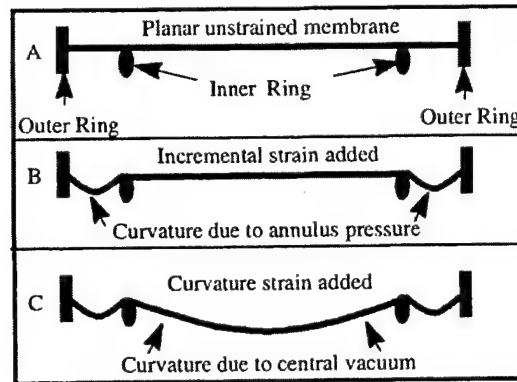
Figure 2.6   AFRL Membrane Pre-strain (48)

characterized by a Poisson ratio of $v = 0.4$, Young's modulus of $E = 900 \times 10^6$ kgf/m^2 or 1280 ksi, and a 125μm thickness, the AFRL group measured maximum axial deviation of the membrane from a reference sphere as a function of pre-strain, measured with a Shack-Hartmann wavefront sensor using a 66x88 lenslet array, as a function of f-number (Figure 2.7) (48). The plunger technique, using a two-inch diameter plunger displaced only 0.0022 inches, moved the membrane past spherical to near-parabolic, and provided improved shape control despite obstructing the center of the membrane region.

Both of these techniques imparted strain to the membrane, addressing minimum strain requirements for an optical membrane. With increased membrane strain, global wavefront variations are reduced. The effect is a decrease in local wavefront tilt across the surface. Local tilt in the membrane can arise from a variety of sources: deterministic shape, boundary conditions, inhomogeneous materials, thickness variations, wrinkling, and surface roughness (29). Proper membrane mounting can significantly decrease initial local tilt and provide a good initial membrane surface. However, there may be significantly more tension required for a proper imaging surface, dependant on the material used. AFRL found that their membrane mounting/assembly technique produced an 0.05% of initial strain based on the membrane response to annulus vacuum pressure (48).

AFRL used a Twyman-Green interferometer to map surface topography using a He-Ne laser at $\lambda = 543$ nm, where a bright-dark fringe series represents 271.5 nm of surface deviation (considering the factor of two in reflection) (23). Manual vacuum pump strokes
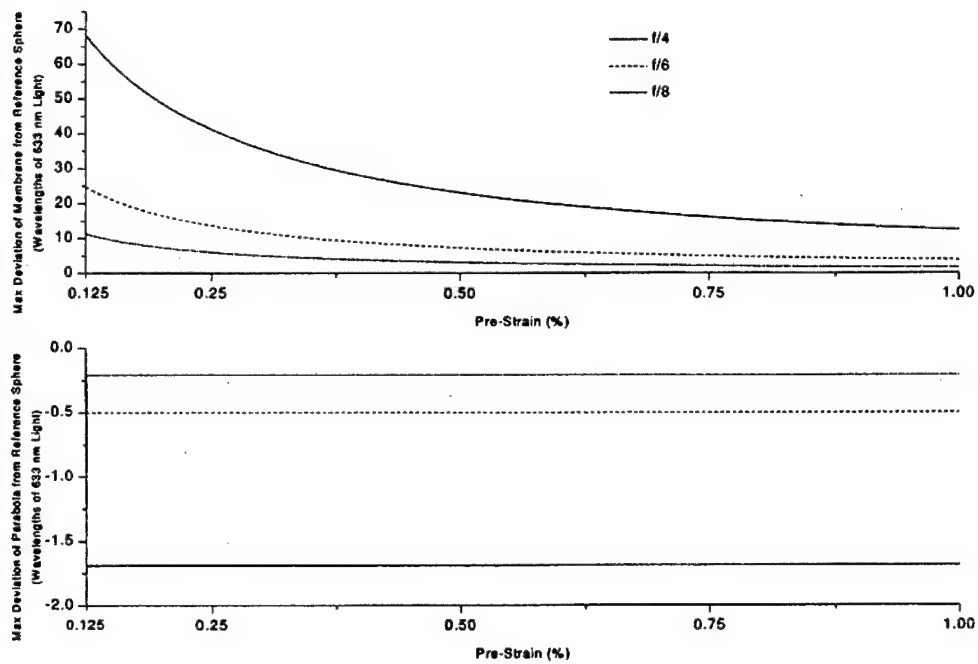
Figure 2.7   Membrane Deviation from Reference (48)
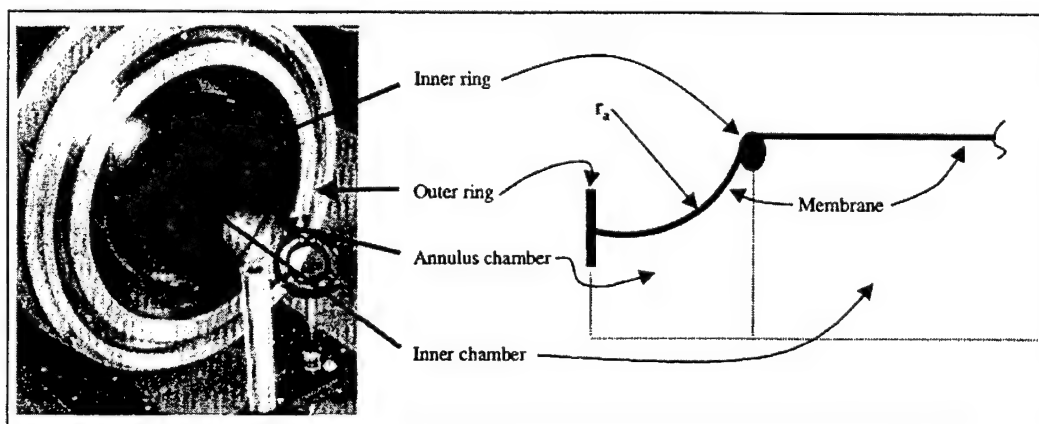
Figure 2.8   AFRL Incremental Membrane Strain (29)

were added to the annulus, which improved surface roughness as observed by decreasing fringe density, until adding additional strokes did not alter the surface (Figure 2.9). The

125 micron UPILEX: 0 to 40 strokes of annulus vacuum. As strain in imparted, the surface wrinkles are pulled out, resulting in a smoother surface profile.
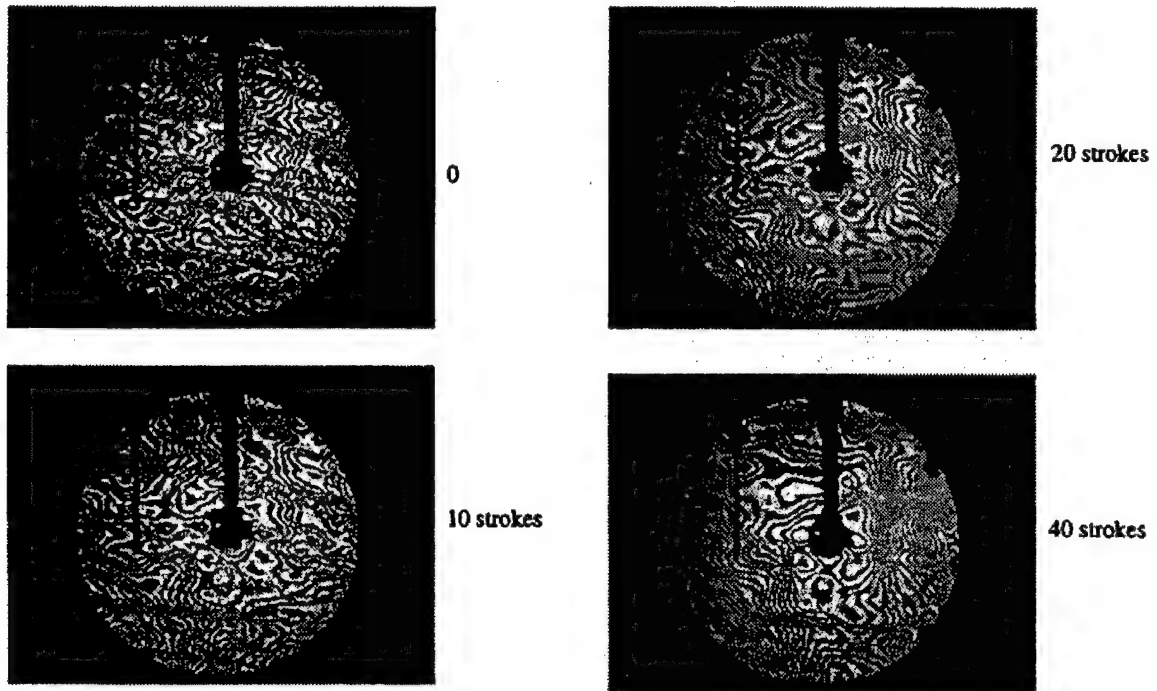
Figure 2.9   Fringe Density as Function of Increased Membrane Tension (29)

group found that optimal strain for the 125 micron Upilex case tested was 40 strokes, or near 0.25% incremental strain (29). Optimum strain will of course vary based on material properties, and should be designed low to minimize structural demands.

2.4   Holography

The use of lightweight membranes as primary mirrors in a space imaging system has many advantages. The major disadvantage to the implementation of membranes in an operational imaging system is the potential for significantly higher aberration over traditional polished mirrors. This wavefront distortion created by distortions in the membrane surface, must be somehow removed for accurate imaging. A holographic correction tech-
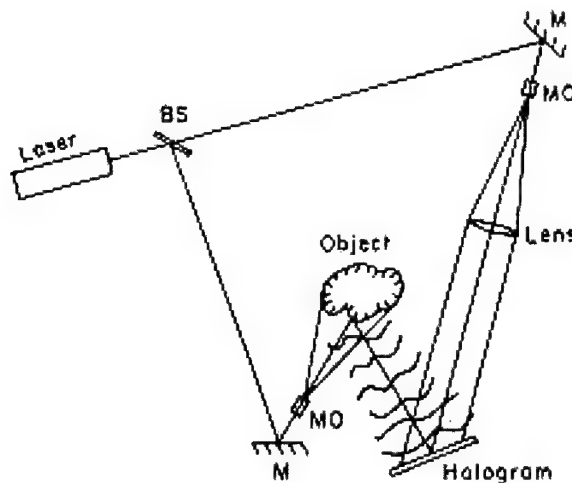
Figure 2.10   Traditional Holograpy Setup (13)

nique was developed in the 1970's to remove static phase distortions from an imaging system, using holographic plates (44). Holography is integral to the eventual use of optical membranes, and to the recent push in experimenting with flexible membranes both in the United States and around the world. Researchers at the University of Strathclyde in Glasgow, Scotland are using large membrane mirrors in volumetric imaging. The Vavilov Laser Physics Institute in Saint Petersburg, Russia, is studying the correction of membrane mirror aberrations with real-time holography. The Surveillance Technologies Branch of AFRL has demonstrated that membranes can yield a near diffraction limited image when corrected with real-time holography (30).

A typical holography setup uses a beamsplitter to divide a laser beam into an object wave and a reference wave. The object wave is expanded with a lens in order to illuminate the entire object, which reflects (some) light onto the hologram plate. This reflected light, containing multi-dimensional object information combines with the reference wave, as shown in Figure 2.10, creating an intensity distribution on the hologram plate (traditionally a high resolution silver halide film plate), and forms a hologram recording which is then developed (13).

Advances were made in the 1990's to use real-time holographic systems using photosensitive devices, specifically a liquid crystal optically addressed spatial light modulator
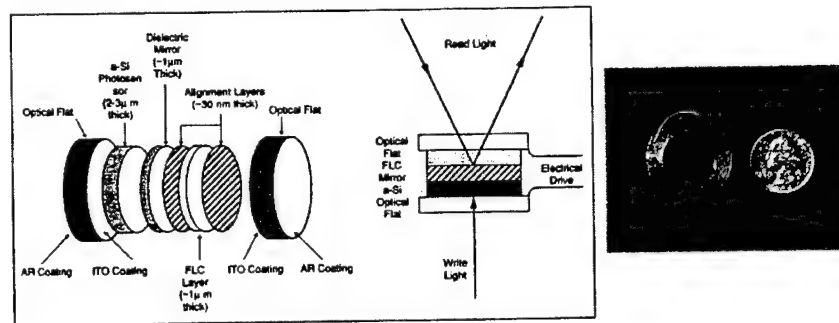
Figure 2.11   Exploded View and Photograph of an OASLM (19)

(OASLM), consisting of a photoconductor and a thin liquid crystal layer situated between an pair of transparent electrodes as shown in Figure 2.11. Current OASLM's can achieve refresh rates of near 1 kHz, with 100 nJ writing energy and 25 mm apertures (19). However, according to Gruneisen, the shortcoming of the OASLM is its limited diffraction efficiency (only has high as 40%), where recent computer-generated blazed phase holograms were demonstrated to a 90% diffraction efficiency (18). AFRL has shown that real time holographic aberration compensation can correct up to 20 waves of wavefront aberration (10.6μm) with a computer generated blazed hologram on a 50 mm area of a lightweight membrane primary mirror. An illustration of this technique is shown in Figure 2.12, where Guthals (19) corrected images of an Air National Guard base with 12 waves of mirror warp ($\lambda = 532$ nm).

2.5   Summary

In summary, inflatable technology is not new. However, the use of membranes as an optical system has moved from the futuristic to the possible. Technological advancements in polyimide manufacturing to create optical quality membrane material (such as Upilex), along with advancements in adaptive optics and imaging systems have only recently made research in this area productive. The past research in this area forms a solid base for future experimentation with optical quality membrane mirrors.

Uncorrected   **Corrected**

**Experimental
Results
(12λ astigmatism,
35nm bandwidth)**

**Simulation
(12λ astigmatism,
35nm bandwidth)**
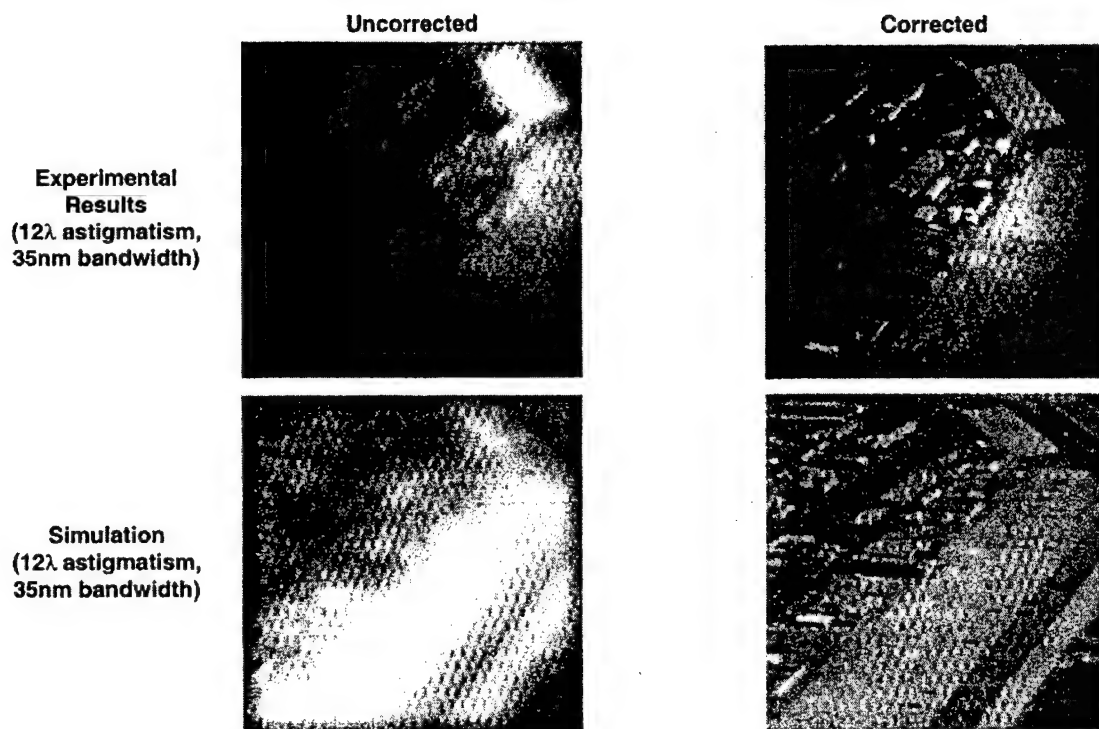
Figure 2.12   Observed and Simulated Grey Scale Images of ANG Base with Holographic
Compensation (19)

2-21

III. Optical Wavefront Description

3.1 Overview

The discussion in this chapter establishes wavefront propagation, evolution of a wavefront through a medium and interference. The primary purpose of optical metrology is determining the aberrations present in an optical component or optical system. The primary method used throughout the optical industry to determine these aberrations is Interferometry, which is able to characterize optical systems to fractions of a micron. Recent developments in Shack-Hartmann wavefront sensing is enabling optical characterization to an even greater accuracy than with the interferometer. This chapter is intended to provide a technical overview of wavefront analysis methods, and an understanding of wavefront aberrations which can be mapped to membrane mirror quality and degree of deformation.

3.2 Optical Wavefront Development

3.2.1 Electromagnetic Wave Propagation.
The work of Scottish physicist James Maxwell and optical developments since his work in the late 1800's removed any doubt of the electromagnetic nature of light. We know from the classical study of physical optics that light travels in electromagnetic waves, and in quantum mechanics we understand that both light and material particles display wave-particle properties. The wavefront is defined as a surface of constant phase or constant optical path length.

Mathematically, basic harmonic wave propagation along a ray in the x direction can be described as:

$$u = u_0 sin\phi = u_0 sin[2\pi\frac{(x-ct)}{\lambda}] = u_0 sin[k(x-ct)] \qquad (3.1)$$

where the field amplitude u is cyclic, phase ϕ refers to the phase at some point in the cycle (when $\phi = 90, u = u_0$), $(x - ct)$ represents a progressive wave traveling at speed c in the positive x-direction, and k is a positive constant known as the wave propagation number(k$= \frac{2\pi}{\lambda}$), as shown in Figure 3.1 (14)(21).

3-1
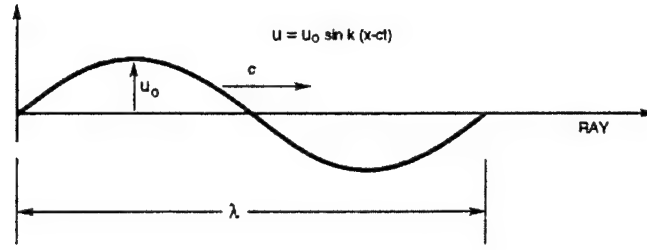
Figure 3.1   Wave Propagation (14)

The set of integral equations that describe electromagnetic disturbances, known collectively as Maxwell's Equations, are essentially Faraday's Induction Law, Gauss's (Electric) Law, Gauss's (Magnetic) Law, and Ampre's Circuital law, respectively:

$$\oint_C \mathbf{E} \cdot dl = -\iint_A \frac{\delta \mathbf{B}}{\delta t} \cdot d\mathbf{S} \tag{3.2}$$

$$\oiint_A \mathbf{E} \cdot d\mathbf{S} = \frac{1}{\epsilon} \iiint_V \rho dV \tag{3.3}$$

$$\Phi_M = \oiint_A \mathbf{B} \cdot d\mathbf{S} = 0 \tag{3.4}$$

$$\oint_C \mathbf{B} \cdot dl = \mu \iint_A \left[\mathbf{J} + \epsilon \frac{\delta \mathbf{E}}{\delta t} \right] \cdot d\mathbf{S} \tag{3.5}$$

where $\mathbf{E}$ and $\mathbf{B}$ are the electric and magnetic field vectors, respectively, $\oint_C \mathbf{E} \cdot dl$ is the electro-motive force taken around the closed curve C corresponding to the conducting loop l, $d\mathbf{S}$ is the surface normal vector to the area (A) surrounded by a closed conducting loop, μ and ϵ are the permeability and permittivity, respectively, of the medium in which the

disturbance is propagating, ρ is charge distribution density, V is the volume enclosed by A, Φ_M is the magnetic field intensity, and $\mathbf{J}$ is the current density.

With mathematical manipulation using Gauss' divergence theorem and Stokes' Theorem, we can arrive at the differential form of Maxwell's equations, which form the starting point from which all classical electromagnetic effects can be explained – including the nature of light (25). These equations are:

$$\nabla \cdot \mathbf{E} = \frac{\rho}{\epsilon_0} \tag{3.6}$$

$$\nabla \cdot \mathbf{B} = 0 \tag{3.7}$$

$$\nabla \times \mathbf{E} = -\frac{\delta \mathbf{B}}{\delta t} \tag{3.8}$$

$$\nabla \times \mathbf{B} = \mu_0 \left(\mathbf{J} + \epsilon_0 \frac{\delta \mathbf{E}}{\delta t} \right) \tag{3.9}$$

In the special nonconducting medium of free space (vacuum) which is uncharged ($\rho = 0$), non-conductive ($\sigma = 0$, where Ohm's law states $\mathbf{J} = \sigma \mathbf{E}$), has a zero relative permittivity or dialectric constant ($K_E = 0$), and a zero relative permeability ($K_M = 0$), the differential form of Maxwell's equations take on the form of the three-dimensional wave equation,

$$\frac{\delta^2 p}{\delta x^2} + \frac{\delta^2 p}{\delta y^2} + \frac{\delta^2 p}{\delta z^2} - \frac{1}{v^2}\frac{\delta^2 p}{\delta t^2} = 0 \quad or \quad \nabla^2 p - \frac{1}{v^2}\frac{\delta^2 p}{\delta t^2} = 0 \tag{3.10}$$

resulting in two concise vector expressions for electric and magnetic fields. Each component obeys equation (3.10), above,

$$\nabla^2 \mathbf{E} = \epsilon_0 \mu_0 \frac{\delta^2 \mathbf{E}}{\delta t^2} \tag{3.11}$$

$$\nabla^2 \mathbf{B} = \epsilon_0 \mu_0 \frac{\delta^2 \mathbf{B}}{\delta t^2} \tag{3.12}$$

which is true provided the speed of the electromagnetic wave is equal to $\sqrt{\mu_0 \epsilon_0}$. This was experimentally demonstrated by the time of Maxwell's work, by the experiments conducted by Armand Fizeau in 1849 and others, with the speed of the electromagnetic wave in free space:

$$v = \frac{1}{\sqrt{\epsilon_0 \mu_0}} \equiv c \approx 2.9979 \cdot 10^8 \quad m/s \tag{3.13}$$

By the end of the 1800's, Maxwell's electromagnetic wave model of light was firmly established. Due to the coupling of electric and magnetic fields in free space (Maxwell's equations still apply to their respective solutions), either equation (3.11) or (3.12) may be used to analyze optical waves. Electric field study is the traditional one chosen for this task (and will be used henceforth in this discussion), which is described by

$$\mathbf{E}(\mathbf{r}, t) = E_0(\mathbf{r}, t) sin[\omega t - (\mathbf{k} \cdot \mathbf{r} + \varphi)] \tag{3.14}$$

where E_0 is the amplitude of the harmonic disturbance moving in the positive $\mathbf{r}$ direction, ω the angular temporal frequency $(2\pi\nu)$, $\mathbf{k}$ is the wave propagation vector, which is the result of the dot product of the wave propagation number, k, and $\hat{s}$ ($\mathbf{k} = k \cdot \hat{s}$) where $\hat{s} = (\hat{x}, \hat{y}, \hat{z})$ is the direction of wavefront propagation passing through a point, and φ is the initial phase of the wave (which is characteristic of the source, as the phase position of the wavefront at the origin is not unique, but is assumed zero in this study, however). The position vector from the point is written as $\mathbf{r} = x\hat{x} + y\hat{y} + z\hat{z}$. Together ($\mathbf{k} \cdot \mathbf{r}$ =constant), they describe a plane in space over which the phase ϕ of the beam varies sinusoidally, creating plane waves, with a plane perpendicular to $\hat{s}$, as shown in Figure 3.2. Electric and magnetic field orientation in a plane wave is illustrated in Figure 3.3.

Any three dimensional wave can be expressed as a combination of plane waves, and any given time, the surfaces joining all points of equal phase are known as wavefronts.
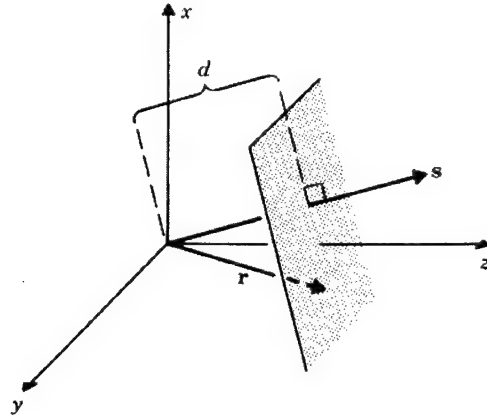
Figure 3.2   Propagation of a Plane Wave (25)
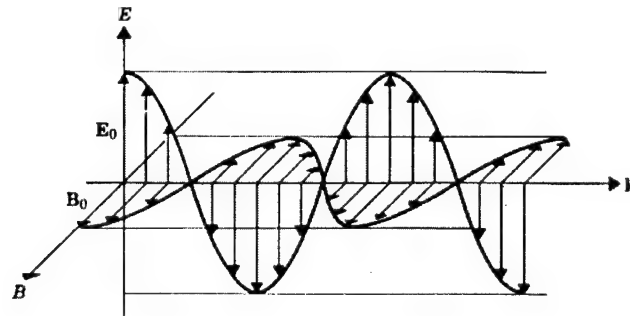
Figure 3.3   Plane Wave Electromagnetic Field (25)

Alternatively, and more commonly, the electric field is represented by its complex (Euler) representation:

$$\mathbf{E}(\mathbf{r}, t) = E_0(\mathbf{r}, t) e^{j(\varphi(\mathbf{r}, t) + k \cdot r - \omega t)} \tag{3.15}$$

Each of the above equations are equivalent solutions to the second-order, homogeneous linear partial differential equation (3.11), the wave equation, for a wave propagating in the x-direction. The simplified representation of the above uses Φ to represent the entire phase term:

$$\mathbf{E}(\mathbf{r}, t) = E_0(\mathbf{r}, t) e^{j\Phi(\mathbf{r}, t)} \tag{3.16}$$
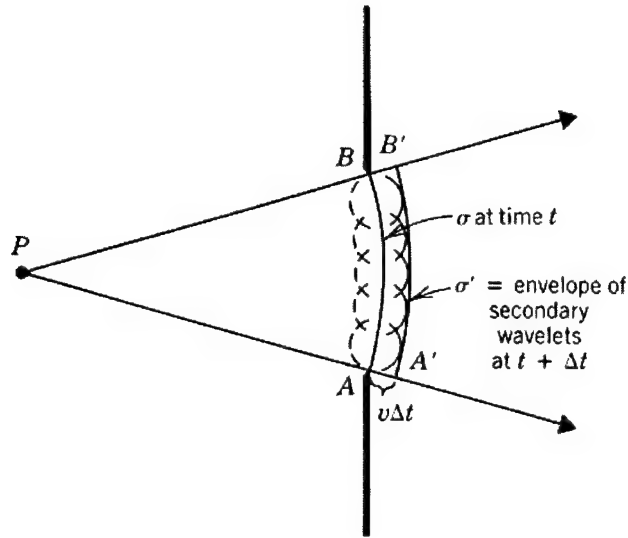
Figure 3.4   Huygen's Principle of Wave Propagation (25)

The wavefront is thus a two-dimensional map of the electric field amplitude and phase. Wavefront propagation occurs according to Huygens-Fresnel Principle, which states that every point on a propagating wavefront serves as the source of spherical secondary wavelets with the same frequency and speed as the primary wave. The wavefront at some later time is the envelope, or superposition of these wavelets, shown in Figure 3.4.

3.3   Wavefront Interference

3.3.1   Superposition.   While equation (3.16) is a solution to the wave equation, other solutions are possible. For example, if $\mathbf{E}_1$ and $\mathbf{E}_2$ are each separate solutions to the wave equation, then $(\mathbf{E}_1 + \mathbf{E}_2)$ is also a solution, following what is known as the superposition principle. Therefore, two or more unique overlapping waves will not permanently distort or destroy another, but will simply add to or detract from each other. For any point in space, the disturbance at each point is the algebraic sum of individual waves at that point,

$$\mathbf{E}(\mathbf{r}, t) = \sum_{i=1}^{n} \mathbf{E}_i(\mathbf{r}, t) \tag{3.17}$$

3-6

where $\mathbf{r} = x\hat{\mathbf{x}} + y\hat{\mathbf{y}} + z\hat{\mathbf{z}}$ is the wave propagation vector in 3-space. This principle forms the basis for interference, which occurs when two or more coherent (temporal and spatial) light beams are superimposed, with white light as the sum of interfering coherent light of various wavelength. The superposition principle can be seen in the Figure below, showing the phase angle difference between two sinusoids. In Figure 3.5, we see constructive interference of the two in-phase waves, resulting in increased amplitude (ψ), and in Figure 3.6, we see destructive interference resulting in nearly zero amplitude (21).

$$\psi_1 = 1.0 \sin kx$$
$$\psi_2 = 0.9 \sin kx$$
$$\psi = \psi_1 + \psi_2$$
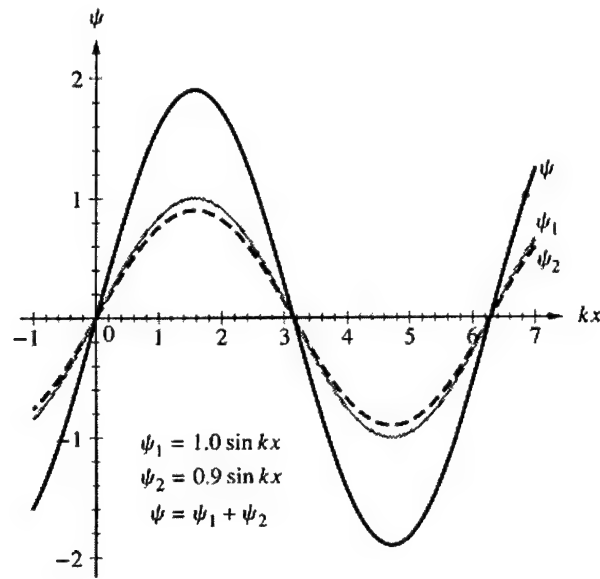
Figure 3.5   Constructive Interference (21)

3.3.2 Irradiance.   The optical electric field disturbance ($\mathbf{E}$) varies in time beyond optical sensor detection ability – from 4.3×10^{14} Hz to 7.5×10^{14} Hz (21). Rather than observing the electric field disturbances directly, optical detection occurs instead by measuring the intensity, or irradiance (I) of the electric field. Irradiance or amount of energy transported by the wave, is measured with a wide variety of sensors or photodetectors (including the naked eye). The irradiance at any point is proportional to the time averaged value of the magnitude of the electric field vector (3.14),

$$I = \epsilon_0 c < E^2 >_T \tag{3.18}$$
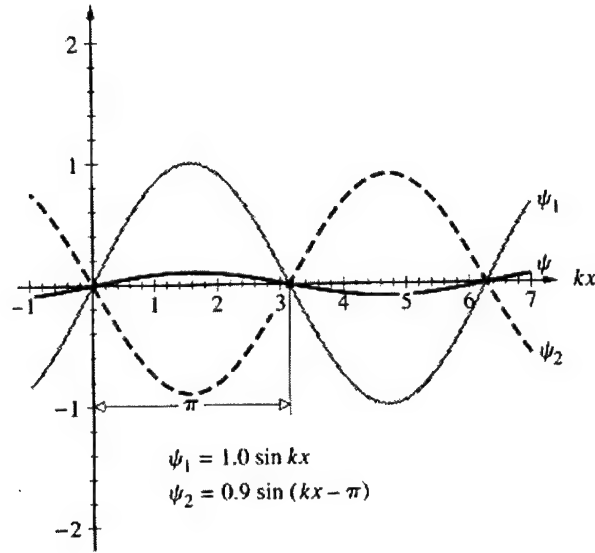
Figure 3.6   Destructive Wave Interference (21)

or

$$I = \epsilon v < E^2 >_T \qquad (3.19)$$

in a linear, homogeneous, isotropic dielectric. Modern photodetector equipment such as CCD's rely on semiconductor detectors. If optical irradiance impacts the sensor region, absorption of a photon generates an electron in the conduction band and a hole in the valence band, leading to a photocurrent in response to the absorbed photon, forming an electronic image representation (16).

3.3.3   Beam Interference.
Two interfering beams of temporally and spatially coherent light, or two coherent interfering wavefronts, can be represented using 3.17 and 3.19 (neglecting the constants) as

$$I = \mathbf{E}^2 = (\mathbf{E}_1 + \mathbf{E}_2) \cdot (\mathbf{E}_1 + \mathbf{E}_2) \qquad (3.20)$$

or

$$I = <\mathbf{E}_1^2>_T + <\mathbf{E}_2^2>_T + 2<\mathbf{E}_1 \cdot \mathbf{E}_2>_T \tag{3.21}$$

with the first two terms simply the time average of the magnitude of the respective electric field intensities squared, or ($<\mathbf{E}_n \cdot \mathbf{E}_n>$, which are the average energy densities of each of the two beams considered independently. The latter term in the above equation is caused by interference. The sign of the interference term may be positive or negative depending on constructive or destructive interference.

The vector nature of the electric field must be emphasized. The scalar product of this term yields:

$$2<\mathbf{E}_1 \cdot \mathbf{E}_2>_T = 2|\mathbf{E}_1||\mathbf{E}_2|\cos\theta \tag{3.22}$$

where θ is the angle between the two vector fields. The direction of the electric field is the important factor in beam interference. For example, interfering parallel beams with perpendicular electric field vectors will not produce interference. The interference term in this case would be zero ($\theta = 90°$) and no interference would result.

3.4   Light and Matter Interaction

When electromagnetic waves of light interact with matter, there will be a combination of transmission, reflection, and refraction of the electromagnetic wave. These are results of absorption and re-emission of electromagnetic radiation by electrons of atoms and molecules, each absorbing and re-emitting photons of the same frequency, causing elastic scattering of the light in all directions.

3.4.1   Medium Density and Index of Refraction.   A more dense medium will retard the wavefront with significantly more photon re-emission and scattering, corresponding to a progressive phase lag over a wavefront in a less dense medium. This translates to a reduction in wave velocity, with a given wave crest requiring a longer
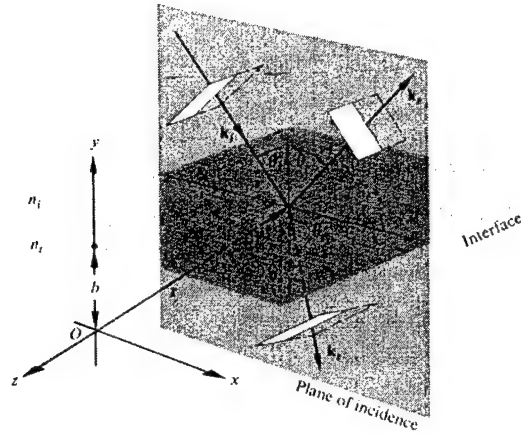
Figure 3.7   Refraction and Reflection of a Plane Wave at Media Boundary (21)

time to arrive at a specific point. This wavefront velocity is given by

$$\nu = \frac{c}{n} \tag{3.23}$$

where n is the index of refraction for a given substance. Examples of n include: air = 1.00029, water = 1.333, and crown glass = 1.52.

3.4.2   Reflection.   When a wave intersects the boundary between matter of increasing densities where there is a sharp discontinuity (an air-glass boundary, for example), a portion of the wave is transmitted through the interface and a portion is reflected on the interface.

If the wave incident on the interface is inclined from the perpendicular at some angle (θ_i), there will be an equal angle of reflection (θ_r) which forms the first part of the Law of Reflection. The second part of the Law of Reflection states that the incident ray, the perpendicular to the surface, and the reflected ray all lie in a plane called the plane of incidence as depicted in Figure 3.7 (21).

The principles of electromagnetic theory stated in Section 3.2 apply to wave propagation through and reflected from an interface of differing densities, forming the boundary conditions. Electrons at the interface are forced to vibrate at the frequency of the incident wave. Therefore, scattered light (transmitted and reflected) has the same frequency as the

incident light. Amplitudes of the transmitted and reflected light vary, however, according the Fresnel Equations:

$$r_\perp \equiv \left(\frac{E_0 r}{E_0 i}\right) = \frac{n_i \cos\theta_i - n_t \cos\theta_t}{n_i \cos\theta_i + n_t \cos\theta_t} \qquad (3.24)$$

$$t_\perp \equiv \left(\frac{E_0 t}{E_0 i}\right) = \frac{2n_i \cos\theta_i}{n_i \cos\theta_i + n_t \cos\theta_t} \qquad (3.25)$$

$$r_\parallel = \frac{n_t \cos\theta_i - n_t \cos\theta_t}{n_i \cos\theta_t + n_t \cos\theta_i} \qquad (3.26)$$

$$t_\parallel = \frac{2n_i \cos\theta_i}{n_i \cos\theta_t + n_t \cos\theta_i} \qquad (3.27)$$

where r and t are the amplitude reflection and amplitude transmission coefficients, respectively, describing the amount of light (amplitude) transmitted through or reflected from the interface between the two media. The π phase shift on reflection when the component of the electric field perpendicular to the plane-of-incidence would translate to a reversal in signs of $r_\perp$. The E-Field orientation and phase shifts are important in any interference application and in analyzing interferometer output. The electric field vectors must be aligned for interference. Though the beams need not be in phase (as this is what produces the observable interference pattern), the clearest interference patterns exist when the interfering waves have equal or nearly equal amplitudes. The pattern resulting from interference will produce alternating dark and light zones, called fringes. The central regions of equal amplitude fringes correspond to complete destructive and constructive interference (21).

Combining beams of the same frequency for interference would yield a composite harmonic wave of the same frequency as its constituents, though its amplitude and phase may be different. The phase difference between the interfering waves as contained in the interference term (3.21) describes the constructive or destructive interference of the combined wavefronts, seen as interference fringes. This phase difference could arise from a difference in the initial phase angle (which we assumed to be zero), or a difference in path

length traveled by the two waves. The path length difference in these two waves (equation (3.14) is described as

$$\delta = (\mathbf{k} \cdot \mathbf{r}_1 + \varphi_1) - (\mathbf{k} \cdot \mathbf{r}_2 + \varphi_2) \tag{3.28}$$

With the waves initially in phase, we have

$$\delta = \frac{2\pi}{\lambda}(\mathbf{r}_1 - \mathbf{r}_2) = \frac{2\pi}{\lambda_0}n(\mathbf{r}_1 - \mathbf{r}_2) \tag{3.29}$$

where $n(\mathbf{r}_1 - \mathbf{r}_2)$ is the optical path difference (OPD).

3.4.3   Refraction.

In addition to reflection at the density interface, the transmitted wave will decrease in velocity, as stated above. This velocity decrease forms the basis for refraction, which is the "bending" of the wavefront if it intersects the denser medium at some (θ_i) measured from the perpendicular to the medium. If the index of refraction is determined, the refraction of the optical wave will deviate from the perpendicular to the surface according to Snell's Law:

$$n_i \sin \theta_i = n_t \sin \theta_t \tag{3.30}$$

where n_t and θ_t are the index of refraction and angle of transmission through the transmitting medium. Snell's law forms the first part of the Law of Refraction. Similar to the Law of Reflection, the second part of the Law of Refraction states that the incident, reflected, and refracted rays all lie in the plane-of-incidence. According to Snell's law, the ray entering a higher density (or higher index of refraction) medium bends towards the normal, and a ray entering a lower density medium bends away from the normal. Light follows the Law of Refraction by traversing the path of the shortest possible time, or Fermat's principle. Light would therefore travel the shortest optical path length (OPL) from point A to point B, qualitatively describing diffraction. Optical path length is defined as the

distance traveled (s) through index (n), or:

$$OPL = \int_A^B n(s)ds \qquad (3.31)$$

Refraction at sperical surfaces (Figure 3.8) involves refracting the wavefront toward the normal and producing an image location. With the paraxial approximation (Section 3.4.6), Snell's law can be used to derive what is known as the lensmaker's formula for a thin lens,

$$\frac{1}{s_0} + \frac{1}{s_i} = (n_{lens} - 1)\left[\frac{1}{R_1} - \frac{1}{R_2}\right] \qquad (3.32)$$

where s_0 is object distance from the surface at its vertex, s_i is image distance from the surface at its vertex, and R is the radius of curvature of the lens surface. The image distance for a spherical surface as the object distance approaches infinity is the focal length of the lens, therefore

$$\frac{1}{f} = (n_{lens} - 1)\left[\frac{1}{R_1} - \frac{1}{R_2}\right] \qquad (3.33)$$

and

$$\frac{1}{f} = \frac{1}{s_0} + \frac{1}{s_i} \qquad (3.34)$$

which is the thin lens law or the Gaussian lens formula.

3.4.4 Matrix Methods . A way to model refraction and reflection through a system of optical elements involves the use of matrix multiplication methods. This equates to mathematically propagating a beam or ray through a system to evaluate its performance, refracting at each lens and propagating from element to element. Snell's law for refraction at an interface (3.30) and the thin lens approximation, enables the refraction equation (21):

$$n_{t1}\theta_{t1} = n_{t1}\theta_{t1} - P_1 y_1 \qquad (3.35)$$
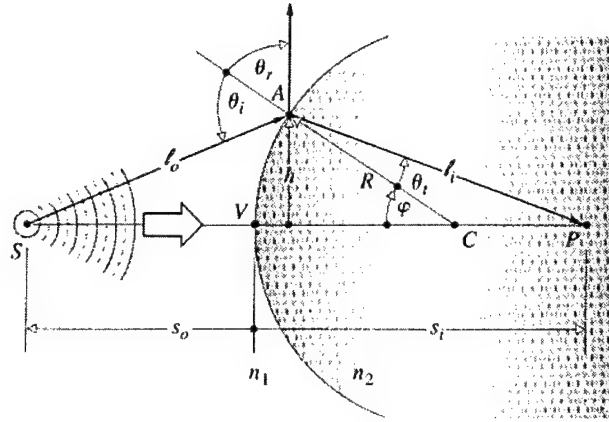
Figure 3.8   Spherical Refraction (21)

where P_1 is the power (inverse focal length) of a single refracting surface, given by:

$$P_1 = \frac{(n_{t1} - n_{i_1})}{R_1} \tag{3.36}$$

and power of a lens can is determined from the lensmaker's equation 3.32:

$$P_{thinlens} = (n_t - n_i) \left[\frac{1}{R_1} - \frac{1}{R_2} \right] \tag{3.37}$$

Refraction at a surface can then be recast into matrix form as

$$R_1 = \begin{bmatrix} 1 & -P_1 \\ 0 & 1 \end{bmatrix} \tag{3.38}$$

from the refraction equation, and axial propagation can be represented by the transfer matrix:

$$T_{21} = \begin{bmatrix} 1 & 0 \\ \frac{d_{21}}{n_{t1}} & 1 \end{bmatrix} \tag{3.39}$$

A system matrix can be formed which models refraction at the surface of a medium and translation through the medium by multiplying the refraction and translation matrices together. For example, refraction through a lens from surface 1 to surface 2 is modeled

3-14

by A, where $A = R_2 T_{21} R_1$. Additional optical elements may be modeled by additional multiplications of refraction and translation matrices. Once the system matrix is formed, the system can be modeled as a thin lens to determine image locations using the thin lens law after determining principle system planes. Finding principle system planes for a thick lens, or an entire optical system, equates to modeling the system as a thin lens at the location of the principle plane. The location of principle system planes can be calculated (21) from the system matrix. Similar to equation (3.38), the power of the thick lens or system of lenses is the M_{12} term in the matrix

$$M = \begin{bmatrix} M_{11} & M_{12} \\ M_{21} & M_{22} \end{bmatrix} \tag{3.40}$$

From the system matrix, the location of the principle plane from the vertex of the first optical element encountered by the wavefront in the system (with propagation in air, n=1) is determined

$$H_1 = \frac{1 - M_{11}}{-M_{12}} \tag{3.41}$$

and the location of the principle plane from the vertex of the last optical element encountered by the wavefront as

$$H_1 = \frac{M_{22} - 1}{-M_{12}} \tag{3.42}$$

After principle plane locations are determined, the image distance can be calculated for the system using the Gaussian lens formula 3.34 with object and image distances calculated from principle plane locations.

3.4.5 Wavefront Distribution and Imaging.

The Huygens-Fresnel principle (Section 3.2), describes the wavefield and how it propagates from an aperture. This principle in rectangular coordinates, as shown in Figure 3.9, calculates the wavefield across the (x,y) plane, parallel to the origin (ξ, η) plane and at a normal distance z which pierces the origin of both planes.
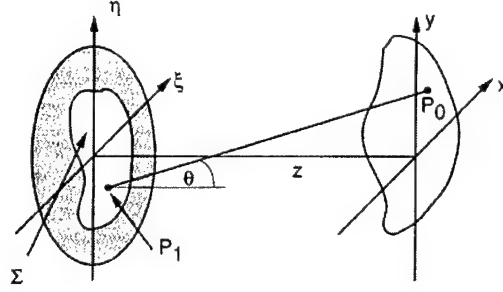
Figure 3.9   Huygens-Fresnel Principle in Rectangular Coordinates (16)

The Huygens-Fresnel principle can be stated mathematically as

$$E(P_0) = \frac{1}{j\lambda} \int \int_{\Sigma} E(P_1) \frac{e^{(jk\mathbf{r}_{01})}}{r_{01}} \cos\theta \ ds \tag{3.43}$$

where $E(P_0)$ and $E(P_1)$ represent the electric field at point P_0 in the object plane and at point P_1 in the image plane, θ is the angle between the outward normal $\hat{n}$ and the vector $\mathbf{r}_{01}$ pointing from P_0 to P_1, $\cos\theta = \frac{z}{r_{01}}$, and the observation distance $r_{01} = \sqrt{z^2 + (x-\xi)^2 + (y-\eta)^2}$, which is assumed to be many wavelengths from the aperture $(r_{01} \gg \lambda)$.

3.4.6   Images Without Aberration.   The wavefront-image description for this application which relates point locations in the object to point locations in the image is achieved using polar coordinates with circular apertures due to the circular object and image.

Karl Friedrich Gauss first described "perfect" image formation (in quotations due to its theoretical nature), where the ideal image would be formed from a point source. The wavefront would be spherical and, if imaged by a "perfect" lens, the image would be perfectly formed at the image distance from the lens. This wavefront is known as the Gaussian wavefront, or paraxial, as "perfect" image formation according to a first-order approximation which small values of φ in Figure 3.8 leads to $\sin\varphi \approx \varphi$ of the sin power series. This small region near the vertex of the imaging lens is the paraxial region.
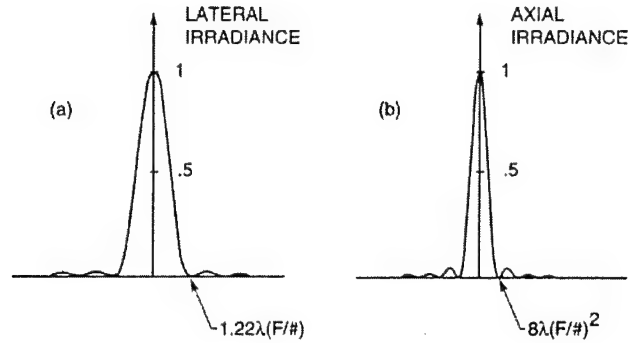
Figure 3.10   Lateral (a) and Axial (b) Diffraction Limit Intensity Pattern (Airy Pattern)

In theoretical geometric optics, a perfect imaging system could manipulate a wavefront originating from a point source and converge it to an image point. Only a spherical wavefront can converge to the image point, and if the wavefront is less than spherical (aberrated), the resultant image would lose resolution, as the image formed by a wavefront with aberrations is spread out in some volume about the ideal image point.

In actuality, or physical optics, image quality is limited. A point source will not image to a perfect point source but will have some finite size. This is the diffraction limitation of physical optics. This lateral irradiance (Figure 3.10), or diffraction-limited image, is known as the point spread function (PSF) with the Airy disk as the core:

$$Airy \ \ Disk \ \ diameter = 2.44 \cdot \lambda \cdot (f/\#) \qquad (3.44)$$

where (f/#) is the F-number of the system, or

$$(f/\#) = \frac{focal \ length}{aperture \ diameter} \qquad (3.45)$$

3.5   Describing the Wavefront

The OPD from the reference spherical or planar wavefront and the abberated (actual) wavefront is described mathematically by a function $W(x, y)$ over the exit pupil in
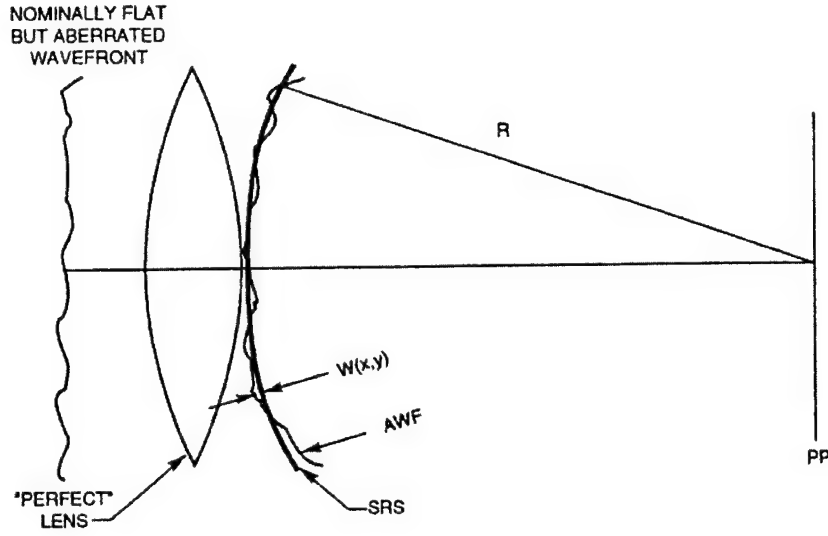
Figure 3.11   Aberration in an Optical System (14)

the optical system, and is shown in Figure 3.11. This function can be described by a polynomial. There are two sets of polynomials which are used by optical designers and professionals to describe imaging in optical systems, the Seidel and Zernike polynomial series.

3.5.1   Seidel Polynomial Series.

The Seidel polynomial series arises from the departure of first order theory when rays from outside the paraxial region of the lens are used to formulate an image. Obviously $\sin \varphi \approx \varphi$ is not adequate outside the paraxial region, and $\sin \varphi$ must include more terms from the sin power series. Siedel aberrations (also called the primary aberrations) are the variations in the wavefront from third-order theory, given by the expansion

$$\sin \varphi = \varphi - \frac{\varphi^3}{3!} + \frac{\varphi^5}{5!} \tag{3.46}$$

The Seidel polynomial is

$$W = \Sigma_{i,j,k} \bar{H}^i \rho^j \cos^k \phi \tag{3.47}$$

3-18

using the polar coordinate system (Figure 3.12a)where ijk defines the particular aberration term in the series where the subscripts refer to the powers on the other factors in the term. The factor $\bar{H}$ is the fractional image height, a normalized value as shown in Figure 3.12b. Both fractional image height, $\bar{H}$, and the fractional pupil radius, ρ, range in value from
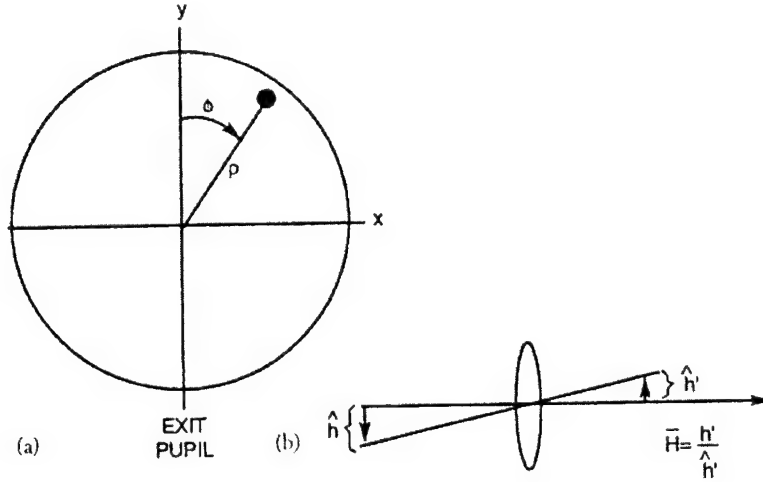
Figure 3.12   Seidel Aberration Coordinate System in: (a) Exit Pupil and (b) Image

0 to 1. The most familiar aberrations are the Seidel: spherical, coma, astigmatism, field curvature and distortion, which are the five lower terms in the Seidel polynomial (i+j=4). Focus, spherical aberration, coma, and astigmatism are shown in Figure 3.13.

3.5.2   Zernike Polynomial Series.
To identify and categorize existing wavefronts, the Zernike polynomial series is used. This polynomial series is

$$W = \sum_i Z_i R_i(\rho) G_i(\psi) \tag{3.48}$$

where dimensionality is maintained by the coefficient Z which is the particular aberration in the series, ψ is the angle in the exit pupil measured from the x-axis instead of the y-axis (14). The first nine Zernike polynomials are written as:

$$W(\rho, \psi) = Z_0 + Z_1 \rho \cos \psi + Z_2 \rho \sin \psi + Z_3(2\rho^2 - 1) \tag{3.49}$$
$$+ Z_4 \rho^2 \cos 2\psi + Z_5 \rho^2 \sin 2\psi + Z_6(3\rho^2 - 2)\rho \cos \psi$$
$$+ Z_7(3\rho^2 - 2)\rho \sin \psi + Z_8(6\rho^4 - 6\rho^2 + 1)$$

with the aberrations corresponding to these terms listed in Table 3.1, and illustrated graphically in Figure 3.14.

Table 3.1   Aberrations of the First Nine Zernike Terms

Z_0	piston
Z_1	x-tilt
Z_2	y-tilt
Z_3	focus
Z_4	astigmatism at 0 deg & focus
Z_5	astigmatism at 45 deg & focus
Z_6	coma & x-tilt
Z_7	coma & y-tilt
Z_8	spherical & focus

Zernike polynomials have a number of useful properties:

1. They are orthogonal over the unit circle. If the region of the interferogram is a circle, in the Zernike fit over the circle, the values of the coefficients will not change if more terms are added to the expansion.

2. Several of the Zernike polynomial terms are analogous to Seidel aberrations (focus, spherical, coma, etc.) and have meaning in optical testing.

3. The Zernike polynomial coefficients are directly related to the root-mean-squared (RMS) wavefront error. Each Zernike term minimizes the RMS wavefront error to the order of that term. Adding other aberrations of lower order can only increase the RMS error (40).

The Zernike polynomials provide a convenient way to express wavefront data in polynomial form, and are often used for this purpose. However, they may not be the best polynomials to represent test data. For example, Zernike polynomials would be of little use in air turbulence or testing conical optical elements (40).

3.5.3 Peak-to-Valley and Root Mean Squared.

Zernike and Seidel polynomials can describe wavefront aberrations in terms of the third-order, where wavefront aberration is specified by stating the number of waves each of the third-order aberrations produce. If a single third-order aberration is present, this is of significance. However, for more complicated aberrations where many different aberrations are present, it is useful to use peak-to-valley (PV) wavefront aberration. PV aberration is the maximum departure of the actual wavefront from the reference wavefront in both positive (peak) and negative (valley) directions. Since PV is simply the maximum wavefront error of the test aperture, it is useful to use the root-mean-squared (RMS) aberration description where deviation in the actual wavefront from the reference is averaged over the entire aperture area. This provides more accurate image information, as an optical system with a large PV would perform better than one with a smaller PV but higher RMS than the first.

3.5.4 Strehl Ratio.

The Strehl ratio is a rato of intensity at the Gaussian image point in the presence of aberration divided by the intensity that would be obtained if no aberration were present. This is given mathematically by:

$$SR = \frac{1}{\pi^2} | \int_0^{2\pi} \int_0^1 e^{i2\pi\Delta W(\rho,\theta)} \rho \, d\rho \, d\theta |^2 \qquad (3.50)$$

where ΔW is the wavefront aberration (in waves) relative to the reference sphere for diffraction focus. When aberrations are small, the Shrehl ratio is independent of the nature of the aberration, since third-order and higher powers of $2\pi\Delta W$ can be neglected, and would be smaller that the ideal value of 1 by an amount proportional to the variance of the wavefront deformation (40).

3.6   Wavefront Measurement Devices

Wavefront measurement devices are collectively known as wavefront sensors. However, there are two classes of sensors, those which use interference to measure the wavefront those which rely on other techniques. The primary technique which does not rely on interferometry is the Shack-Hartmann sensing method which is referred to in this analysis as a "Wavefront Sensor."

3.6.1   Interferometers.

An interferometer is a device used to measure very small changes in wavelength, refractive index, or distance by interfering visible electromagnetic radiation waves (light beams). Modern interferometry involves analyzing fringe patterns with computer analysis programs which perform Seidel and Zernike polynomial curve fits to characterize the wavefront.

Optical interferometry has been developing for over 300 years. Its origin dates to the late 1600's with the explanation by Boyle and Hooke of the fringes seen in a thin air film between two glass plates in contact (Newton's Rings). Interferometry experiments aided the development of the wave nature of light, the rejection of the "luminiferous aether" theory and the foundation of the special theory of relativity. The measurement of wavelength of radiation became the meter standard and microscopic examination of optical components and reflecting surfaces became possible due to interferometry, along with the development of modern coherence theory (25). Interferometry also enabled the development of spectroscopy, holography, stellar interferometry (Michelson successfully used interferometry to measure the diameters of Jupiter's satellites in 1890), and microtopography. Modern applications include the development of modern highly reflective and anti-reflective coatings, accurate measurement of gas densities, the development of the ring laser gyroscope, and many other applications (20).

Interferometers are generally divided into two categories, wavefront splitting and amplitude splitting. In wavefront splitting, separate portions of the original wavefront are used as sources of secondary waves, which are superposed to produce interference. Examples include: Fresnel's mirrors, where light from a point source is reflected at two mirrors making a small angle with each other and interference fringes are observed in the

region where the two beams overlap; Young's double slit experiment, where an interference pattern emerged from sunlight passed through a narrow slit as a cylindrical wave, then separated by two narrow slits, and Lloyd's mirror, where a wave emitted from a point source creates fringes as part of the wave illuminates a flat mirror at near 90° which interferes with the rest of the wave (20).

Amplitude splitting interferometers are the laboratory instrument of choice due to the availability of a coherent light source (laser) and surfaces which both reflect and transmit part of the incident light – beam splitters. Each split beam has a lower amplitude than the incident beam, due to the split in amplitude, and if the light remains coherent upon recombination, interference fringes will develop. Examples of single-beam amplitude splitting interferometers include (21, 25, 20):

- Interference in a plane parallel plate upon incident radiation at some angle, where fringes appear to an optical path length difference when part of the beam is reflected off the top surface of the plate and part of the beam is transmitted through the plate and is reflected off the bottom surface

- Interference in a plate of varying thickness or non-uniform film illuminated at near normal incidence, where fringes develop due to the OPD over the material thickness

- The classic Michelson Interferometer, where a splitter divides the incident wave into two waves which reflect off mirrors (one is movable to achieve variable OPD) and then re-combines the waves which produces an interference pattern at a detector

- The Twyman-Green Interferometer, a collimated light adaptation of the Michelson, which is among the most effective testing tool in Optics

- The Mach-Zender Interferometer, consisting of two beam splitters and two totally reflecting mirrors, where an OPD is introduced by a slight tilt of one of the beam splitters and has been extremely effective in measuring gas-density patterns

- The Sagnac Interferometer, where the beam is split into two oppositely directed identical paths, each forming a closed loop and then reunited at the detector

3.6.2 Wavefront Sensors. A method of direct wavefront measurement without interfering light beams is an adaptation of the Hartmann test developed in 1900 (42). Hartmann developed an opaque mask with holes placed behind the element under test, where each hole acted as an aperture and the image produced was an array of spots. The position of the spots provided an indication of the local wavefront tilt at each hole, providing a categorization of the wavefront at the mask. R.B. Shack developed lenses in 1971 which focused the spots and reduced diffraction effects of the holes, modifying the Hartman test to what is now known as a Shack-Hartmann wavefront sensor (often shortened to Hartmann sensor, or simply wavefront sensor).

The Hartmann wavefront sensor is composed of imaging equipment (CCD camera), a mask with lenses known as a lenslet array, and a data processor. The lenslet array effectively divides the wavefront and an array of quadcells determines spot position (correlated to wavefront tilt), as illustrated in Figure 3.15 The main drawback of the Hartmann sensor is the high degree of precision required for instrument alignment to ensure accurate measurement of wavefront tilt. However, there are significant advantages of this method, including: wide dynamic range, high optical efficiency, white light capability, no 360° ambiguity, and the ability to use either continuous or pulse sources (42).

3.7 Summary

The discussion in this chapter is intended to provide a basic understanding of electromagnetic wave propagation through a medium and enable a basic understanding of how these waves can represent the surface properties of a membrane mirror or any optical surface. Interferomery and Shack-Hartmann wavefront sensing techniques are used to determine wavefront aberrations, which can be mathematically represented with either the Seidel or Zernike polynomial series. These aberrations are expressed as Zernike polynomials by computer based interferometry programs and wavefront sensors, and are calculated by either the location of interference fringes on an interferogram or by focus spot deviation in a wavefront sensor lenslet array. Each of these wavefront sensing techniques will be

utilized in this research to determine membrane mirror surface properties and deformation with applied voltage.

DEFOCUS

$$W_d = W_{020}\,\rho^2$$

SPHERICAL ABERRATION

$$W_s = W_{040}\,\rho^4$$

COMA

$$W_c = W_{131}\,\bar{H}\rho^3\cos\phi$$

ASTIGMATISM

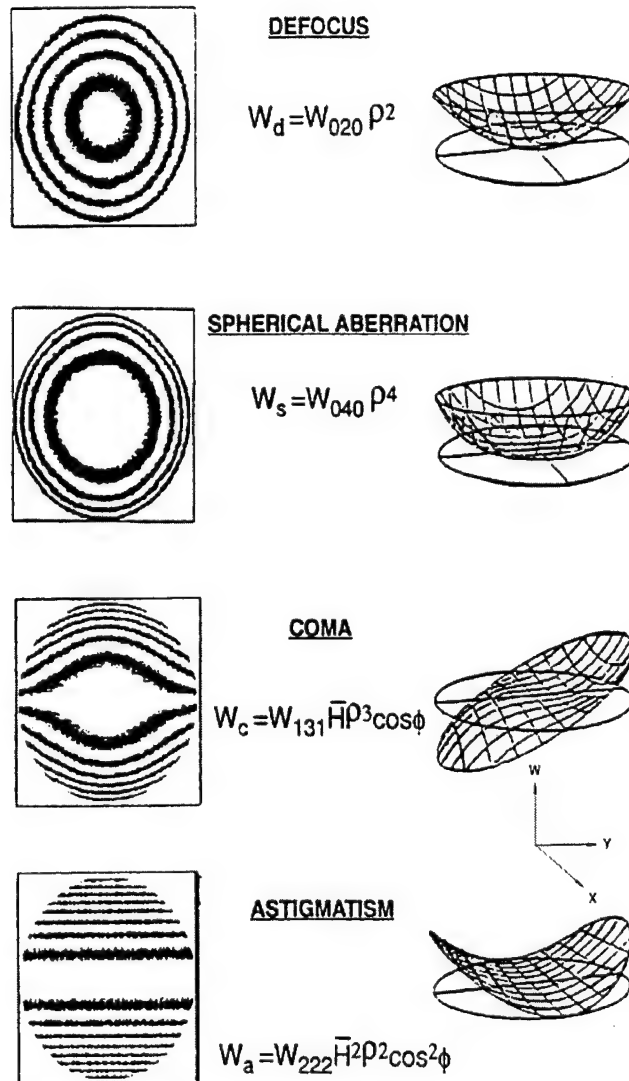$$W_a = W_{222}\,\bar{H}^2\rho^2\cos^2\phi$$
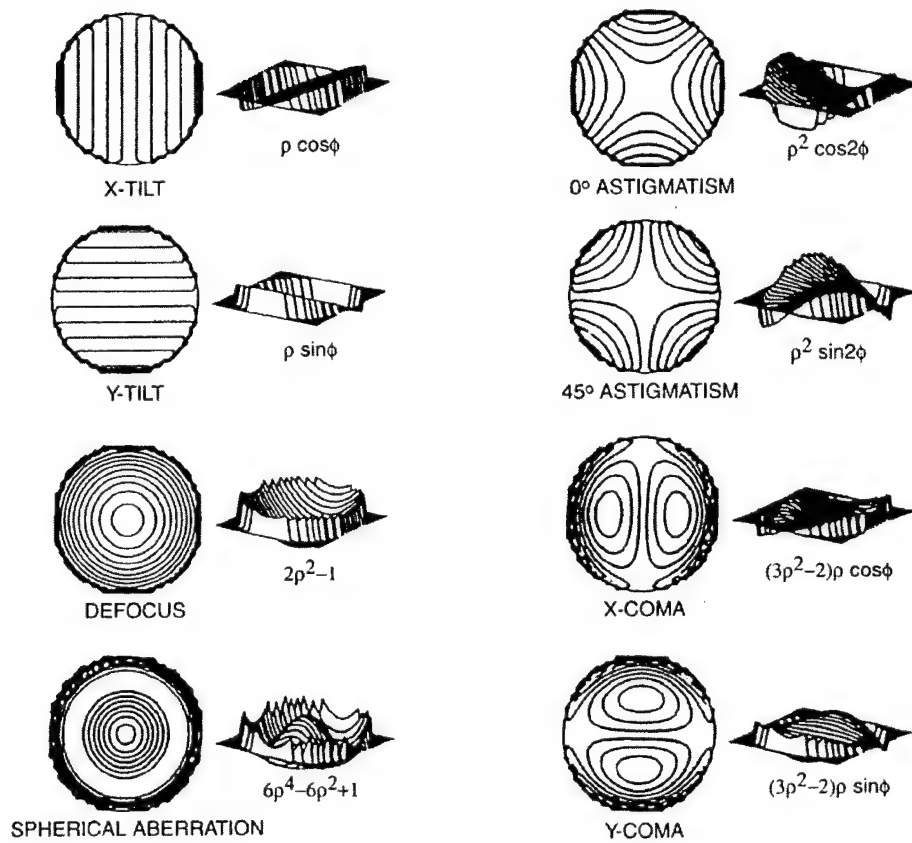
Figure 3.13   Seidel Aberrations (14)

Figure 3.14   Zernike Polynomials 1-8 (14)
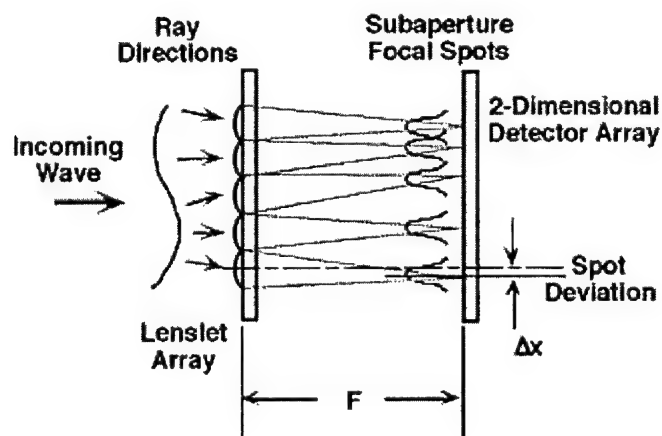
Figure 3.15   Shack Hartmann Wavefront Sensing Technique (47)

IV. Imaging System and Membrane Mirror Construction

4.1 Overview

The imaging system designed for non-contact measurement of membrane mirror surfaces and mirror deflection was based on the Twyman-Green interferometer, illuminated by a Helium-Neon laser. The laser is expanded in the system to allow measurement of up to 12 inch membrane mirrors. The optical setup was designed to output collimated light to allow interchangeability with either a CCD camera for interferometry, or the Adaptive Optics Associates (AOA) Wavescope for Shack-Hartman wavefront sensor measurements. The primary goal in selection of imaging system components and system construction was to build a system which could utilize either sensing technique and provide negligible aberration from the optical components in the test system to accurately represent the test surface.

Optical quality controllable membranes were constructed by stretching Upilex, a polyimide film with 3 nm surface flatness (3), with a stretching ring and bonding a PVDF film to the stretched Upilex. A mounting ring was then bonded to the composite with epoxy, and placed into a 6 inch diameter tip/tilt controllable optical mount. The PVDF film has a nickel-copper electrode, which was etched into patterns after dipping the sheets into photoresist and exposing the desired pattern. Control wires were bonded to the PVDF patterns using conductive epoxy and various types of tape.

4.2 Optical Components

This section provides a description of the components used in the optical system, and illustrates the limits these individual components place on the system as a whole. The system layout is as shown in Figure 4.1, with component descriptions below.

Interferometer Layout

Figure 4.1   Optical System Block Diagram

4.2.1 System Power Source.

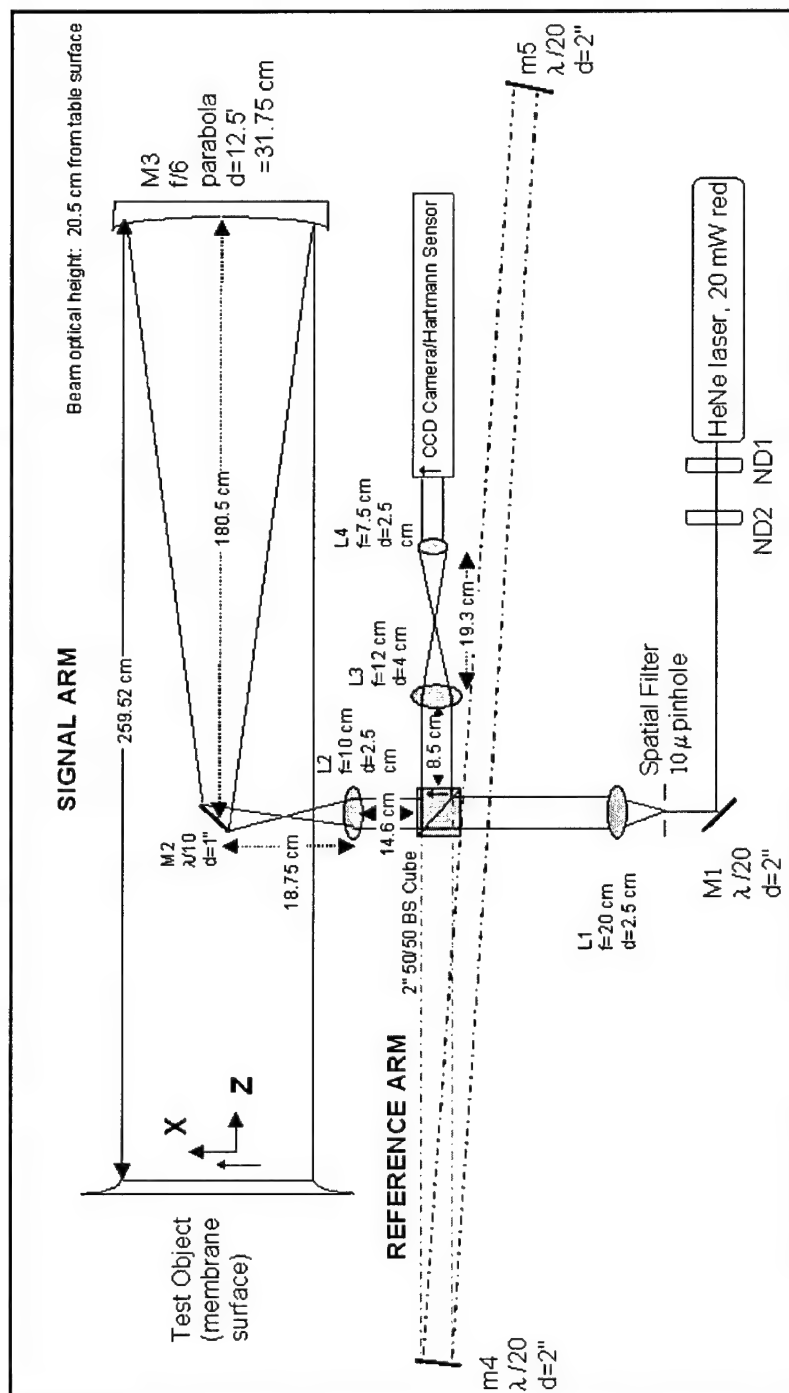A Uniphase Helium-Neon laser was used as the system light source, providing coherent monochromatic light for the interferometry and Hartmann wavefront sensor applications. This laser has a wavelength (λ) of 632.8 nm, is rated to 20 mW with a locally measured nominal output power of 11 mW, beam divergence of 1.2 mr (milliradians), coherence length of 23.4 cm, beam diameter of 0.68 mm and was manufactured in December, 1989. The total number of use hours on this laser when chosen for this application was unknown, but a delay in beam emission from power application was noted, which is an end-of-life symptom.

Wavefront measurements are measured either in microns or fractions of the laser wavelength, and laser type therefore plays a role in the resolution of the system. Coherence length is an important factor in laser choice in an interferometry application, as it is the length in space over which the wave is sinusoidal and its phase can be reliably predicted. If the coherence length is not at least as long as the path length difference in an interferometer, no interference would occur, interference fringes would not appear, and hence no surface measurements would be obtained. For this system, the reference arm path length was adjusted by changing positions of M4 and M5 (Figure 4.1) to the signal arm path length of 940 cm. Based on the coherence length of the laser, these paths could (ideally) only vary within 23.4 cm to obtain interference.

Two circular variable neutral density filters are used to adjust laser beam intensity through the system. These filters are 127 mm in diameter, manufactured by Newport Corporation, with optical density gradient increasing in a counterclockwise direction from 0.05 to 1.0. These filters are represented in Figure 4.1 as ND1 and ND2, and are shown in Figure 4.2. These filters were previously used on other AFIT experiments and the quality was unknown. Experimentation revealed a significant reflection on the input side of the filter, which should have been decreased by an anti-reflective coating. Input reflections did not create a significant problem with experiment results, as the filter mounts used have a tip/tilt capability to ensure the reflected portion of the beam was tilted away from the laser output to avoid the creation of a resonant cavity.
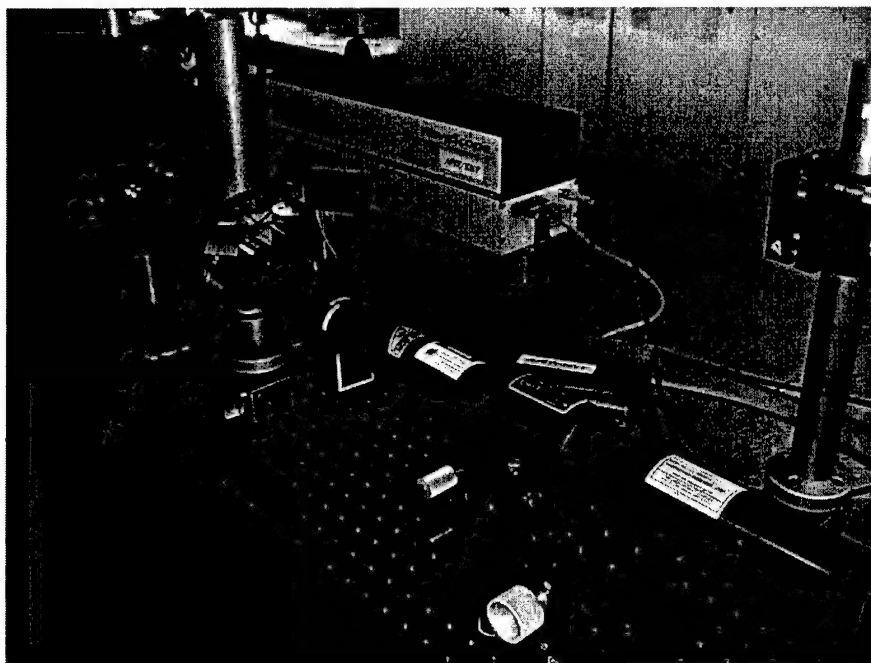
Figure 4.2   Uniphase 20 mW Laser and ND Filters

4.2.2 Turning and Reference Mirrors.   The reference mirrors used in this system are Newport laser line dielectric mirrors coated to optimize reflection at a 632.8 nm wavelength to greater than 99% reflectance from $0 - 45$ deg. Mirror diameter is 2 inches, with a surface flatness of $\frac{\lambda}{20}$ (32 nm) using Zerodur®, a glass-ceramic material with zero nominal thermal expansion. The surface flatness of these mirrors maintains an accurate and unaberrated wavefront, critical for accurate comparison of the test surface to a planar reference. Additionally, these mirrors are $10 - 5$ scratch-dig, which ensures low beam scatter and high performance. These mirrors are represented as M1, M4, and M5 in Figure 4.1, and one is pictured in Figure 4.3.

4.2.3 Spatial Filter.   The function of a spatial filter is to remove intensity fluctuations, or scattering in a laser beam, caused by air particles and/or optical defects, and produce a nearly perfect Gaussian profile. The methodology is to first focus the beam with a microscope objective, producing an image of the source with imperfections defocused in an annulus about the optical axis, and then pass the focused beam through a pinhole which removes most of the noise as shown in Figure 4.4 (32). The spatial filter

4-4
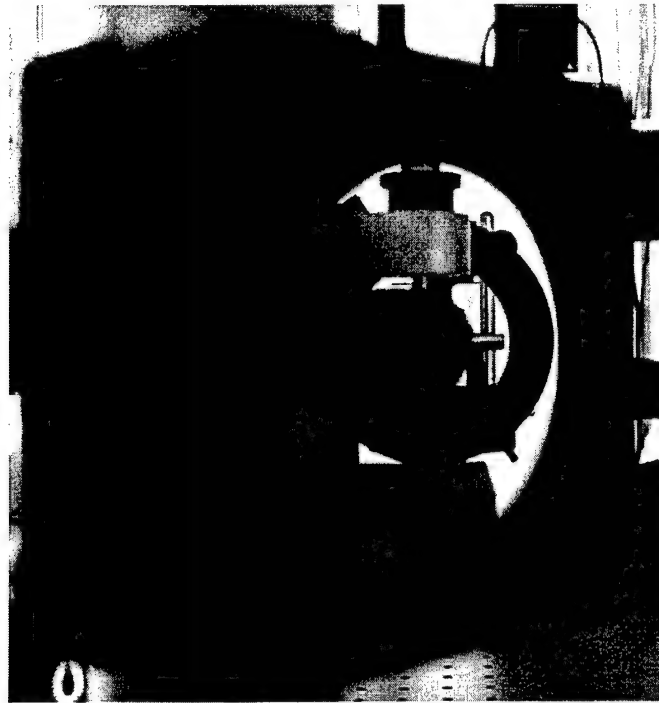
Figure 4.3   2-inch Lambda/20 Reference Flat

provides initial beam expansion in this system, expanding the Airy disk until it is captured by the first lens in the system (L1), which collimates the beam at a 2.5 cm diameter. The spatial filter used in this system is a Newport Model 900, with 3-axis micrometer adjustments which allow for optimum alignment while permitting simple changes of pinholes and objectives. The spatial filter is represented in Figure 4.1, and is pictured in Figure 4.5.

While the spatial filter is necessary to remove noise from the beam, or "re-Gauss" the intensity profile, it can also serve as a source of frustration if the objective power and pinhole size are not chosen properly. The fraction of laser power passed by a pinhole of diameter D is:

$$\frac{P(D)}{TotalPower} = 1 - e^{-\frac{1}{2}\left(\frac{\pi a D}{\lambda f}\right)^2} \tag{4.1}$$
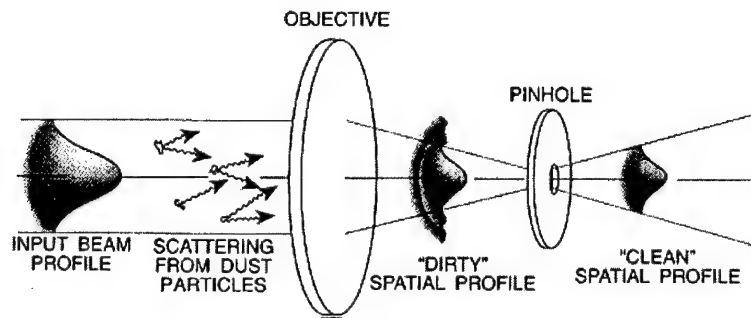
Figure 4.4   Spatial Filtering (32)
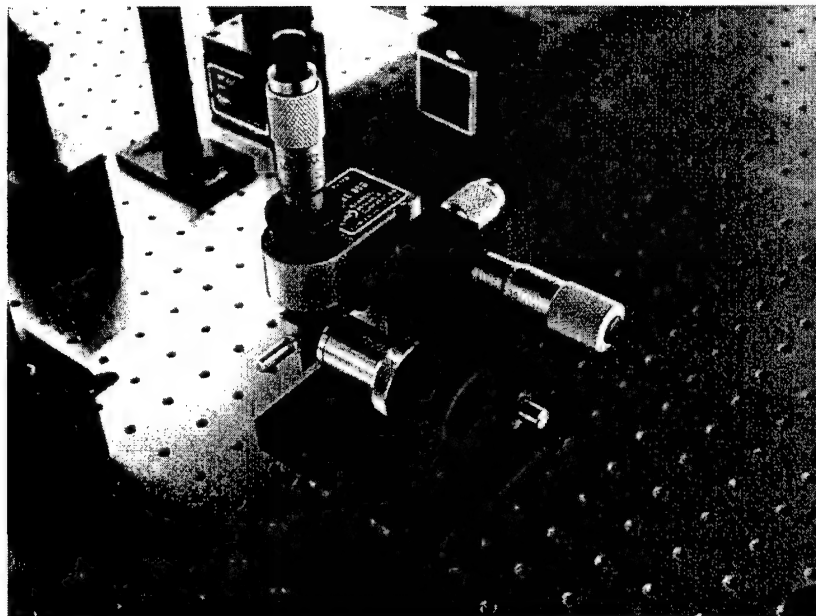
Figure 4.5   Spatial Filter
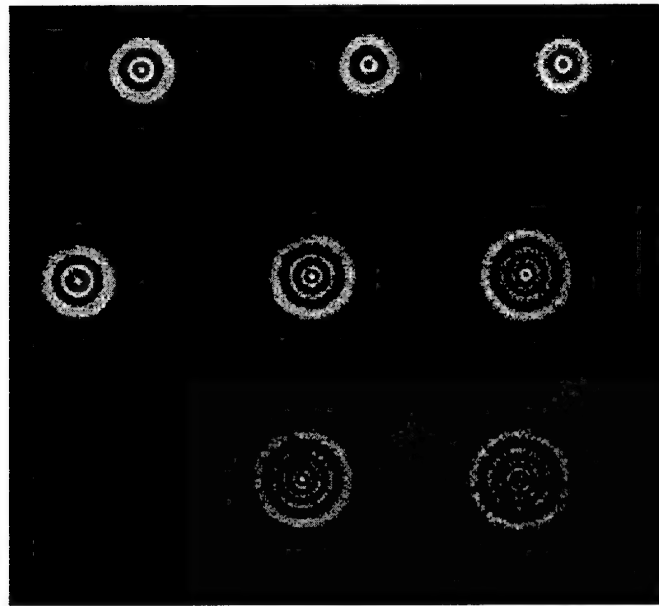
Figure 4.6   Fresnel Rings/Aperture Diffraction

Newport recommends an optimum pinhole of diameter D_{opt}, passing 99.3% of beam energy while blocking spatial wavelengths smaller than 2a, the diameter of the initial beam (32):

$$D_{opt} = \frac{F\lambda}{a} \qquad (4.2)$$

where F is the objective lens focal length and a is the beam radius input to the objective lens. The standard objective for the Newport Model 900 for He-Ne applications is a 10x objective with a focal length of 9 mm, leading to an optimum pinhole diameter of 31μm using the laser described in section 4.2.1. The AFIT Physics Department found through experimentation that a 20x objective produces the best results using He-Ne laser, but produced excessive Fresnel rings in this system as depicted in Figure 4.6, significantly degrading image quality. A 10x objective was then used with a 10μm pinhole, producing good results. Using a lower power objective and a smaller pinhole allowed only the center of the primary lobe to pass through the system, which reduced diffraction ringing and created more uniform illumination.
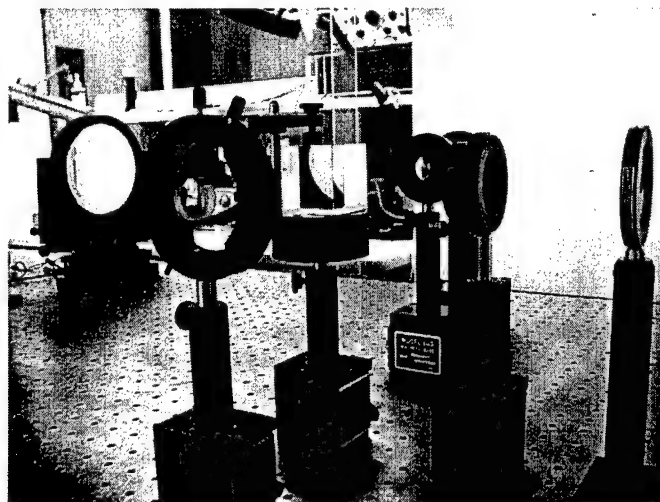
Figure 4.7   Intermediate System Optics

4.2.4 System Optics.   The lenses in this system provide a telescopic expansion and reduction of the laser beam from the original beam diameter to 12.5 inches and eventually produce a collimated 10 cm beam output to the detector.

The first lens, L1, is an Edmund Scientific Achromatic doublet (part 32917), 2.5 cm in diameter with a 20 cm focal length. L1 provides the system with 2.5 cm diameter light by collimating the expanding beam from the spatial filter and transmitting it to the beam splitter. Achromatic doublets are composed of two optical elements cemented together, and are used in the system to limit spherical aberration. Achromatic doublets also limit chromatic aberration, which does not apply to this system, illuminated by a monochromatic source.

The next optical element is a two-inch, BK-7 glass, 50-50 cube beam splitter (Edmund H32704), as shown in Figure 4.7, with surface flatness of less than 316 nm ($\frac{\lambda}{2}$). An anti-reflective coating ($\frac{1}{4}$ wave MgF_2) was factory applied to the outside surfaces and the hypotenuse was multilayer dielectric coated to minimize reflections. During system operation, however, internal reflections were apparent which created additional (ghost) interference fringes. The splitter then transmits half of the beam intensity to the reference mirrors (M4-M5) and half to the signal arm.
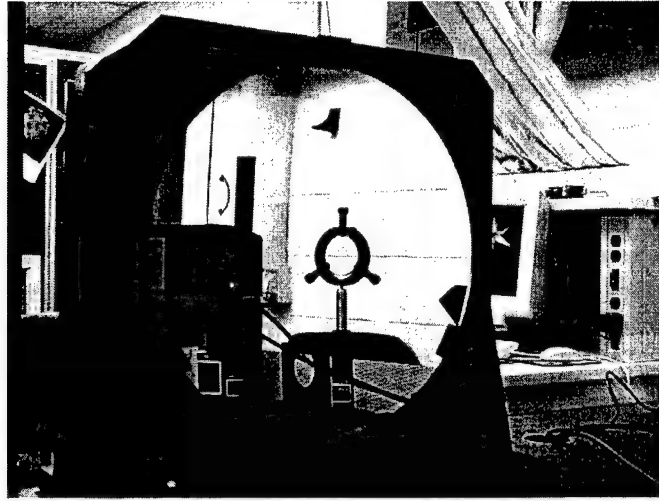
Figure 4.8   Parabolic Imaging Mirror

A 2.5 cm diameter, 10 cm focal length achromatic doublet (Edmund 08056) functions as the beam expander from 1 inch to 12.5 inches. The beam is transmitted from L2 through focus (an iris is used at the focus point as an aid for beam alignment) to a one-inch Zerodur® turning mirror (M2), as pictured in Figure 4.7, coated with enhanced aluminum for increased reflectance and has a surface flatness of $\frac{\lambda}{10}$ (Edmund H32101). The beam continues expansion from M2 to a 12.5 inch diameter parabolic mirror (M3, Edmund H85335), with a focal length of 190.5 cm. L2 is designed to focus the beam for expansion coincident with the M3 focus point, ensuring beam collimation from M3 to the test object. A tip-tilt parabolic mirror mount (Edmund 36480) aids in alignment of M3. Alignment of M3 is relatively simple: the reflected intensity from M3 is adjusted with tip-tilt control to ensure the reflection from M3 on the iris between L2 and M2 is centered in the iris aperture.

If the L2 and M3 focus points are aligned, the beam has expanded to the diameter of the parabolic mirror and is sent perfectly collimated to the test object, or membrane surface (figure 4.9). Collimation must be verified as discussed in Section 4.4.2. The test object reflects this beam back through the system to the beam splitter which then recombines the reference and signal beams in the imaging leg of the system. The splitter sends these two beams to L3, a 4 cm diameter achromatic doublet (Edmund 32921) which focuses the

Figure 4.9   Imaging Leg to Test Object

beam over 12 cm. The beam travels through focus to a 2.5 cm achromat(Edmund 32325) which recollimates the beams and sends the combination to an imaging device.

4.3   Imaging System

4.3.1   Interferometry.   The imaging device used for the interferometry application is a remote-head COHU RS-170 CCD camera with a $\frac{1}{2}$ inch CCD array offering 550 lines of resolution. This electronically sampled image is sent to an Imagenation CX-100-30 precision image capture board with industry leading sampling jitter of only ±3 ns for detecting image details at the sub-pixel level and video noise less than one least significant bit out of 256 grey levels (10). The video data is then computer processed and displayed while simultaneously output to a Panasonic video monitor. The additional video monitor provides real-time feedback during the alignment process, critical to maximizing interference fringe position and contrast.

Information from the CX-100-30 serves as input to the APEX interferogram analysis software by Lambda Research Corporation. APEX provides surface property calculations by automatically finding the centers of fringes and calculating the aberrations present in interferograms. The program has an advertised accuracy of 0.02 fringes RMS, repeatability of 0.01 fringes RMS, and provides a complete set of analysis functions including MTF, PSF,
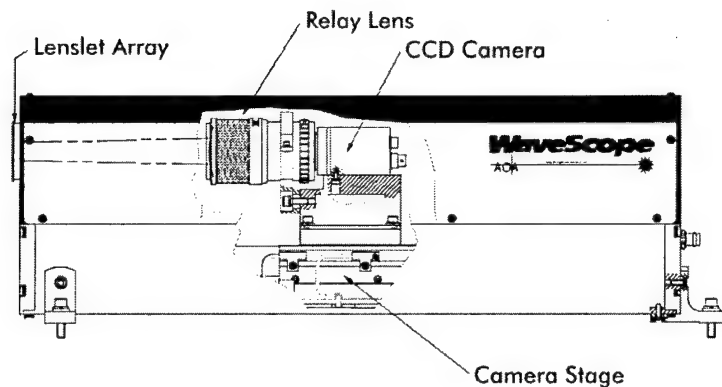
Figure 4.10   Wavescope Sensor Schematic (47)

and slope error (1). The program outputs Zernike polynomial terms along with peak-to-valley, irregularity, and RMS calculations over the aperture. Additionally, the wavefront under test can be subtracted from a reference wavefront to compensate for interferometer errors or to enable null testing. APEX provides graphical output of the wavefront including: contour, contour with X/Y cross-section, 3-D isometric, and standard cross-section plots.

4.3.2   Hartmann Wavefront Sensor.   The Adaptive Optics Associates Wavescope sensor serves as the Hartmann Wavefront Sensor used in this system. A remote sensor head consists of a lenslet array and relay lens, a translating RS-170 CCD camera, and camera stage (Figure4.10). Power for the sensor is provided from a sensor head controller module which provides fusing and EMI filtering and includes the module which drives the sensor head camera stage motor (47). Data from the sensor head is input for a personal computer which serves as user interface and display and performs wavefront calculations. The sensor head and monitor display unit are shown in Figure 4.11. The Wavescope system has advertised performance of (46): wavefront tilt measurements up to 430 waves (632.8 nm) PV, absolute accuracy of less than $\frac{1}{20}$ of a wave, relative accuracy of less than $\frac{1}{50}$ of a wave.

Wavescope is somewhat of a breakthough in industrial adaptive optics due to the translation of the CCD camera which traces the path of the Hartmann spots through each monolithic lenslet module (MLM) during calibration. This enables a significant increase in dynamic range, and is the reason this instrument can track aberrations of hundreds of

4-11
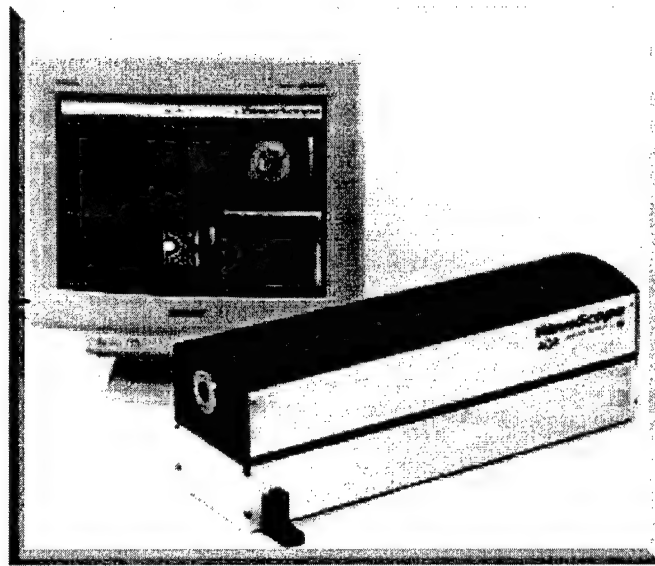
Figure 4.11   Wavescope Sensor Head and Display

waves with fractional wave accuracy (46). A choice can be made between three monolithic lenslet module (MLM) arrays to allow dynamic range adjustment. The MLM primarily used in this setup for static measurements was the 300μ m array, providing good spatial sampling and tilt sensitivity and moderate dynamic range. Choices for lenslet arrays are base on aperture size of the array, with choices of 133μ m, 300μ m, and 480μ m, as shown in Figure 4.12. These lenslet positions are the points where the wavefront is sampled and wavefront slopes are calculated. With a membrane mirror, deviation of the wavefront from a plane wave is the most important consideration, and could be fairly significant. The Shack-Hartmann technique assumes the subaperture sample is approximated by a tilted plane wave, and as curvature of the wavefront increased, the corresponding subaperture deviation increases. However, if there is overwhelming wavefront curvature, the origin of the Hartmann spot may be different from true wavefront tilt. A practical rule-of-thumb given by AOA is to examine the spot images of the chosen MLM array and if they are symmetric over the pupil and do not display any astigmatic ("plus" pattern) or coma ("comet" pattern) aberrations, the measurement is accurate and the asymmetric components of the subaperture wavefront are roughly less than $\frac{1}{4}$ to $\frac{1}{2}$ wave (47).

4-12

Figure 4.12   Wavescope Lenslet Arrays

4.4   System Setup and Alignment

4.4.1   Power source and Primary Optics.

The first step in the system setup is establishing a stable optical platform. A twelve foot Newport optical table was cleaned and floated with a Newport air supply pump to isolate the table from room vibrations. An enclosure was assembled around the table to isolate the optical system from air currents in the room, as shown in Figure 4.13.

The first optical component required for system assembly was M3, the 12.5 inch parabolic mirror. This mirror is the primary imaging mirror, and is placed where it will best image the test object. The center of M3 in its mirror mount determines the optical axis of the remaining system, as beam expansion from M2 must center about this point to ensure collimation of the beam from the parabola to the test object. The height of the optical axis was determined to be 20.5 cm above the table surface.

Once this height is determined, all remaining elements are adjusted to this height. The system laser is adjusted to this height with a Newport (Model 806) laser tip/tilt adjustment mount. The laser provides the alignment index to properly align mirrors M1 and M2 which are placed next. Placement distance from the parabola and the laser is determined from the M3 focal length. If a cartesian coordinate system is placed on the center of the test object as shown in Figure 4.1, M2 is placed a focal length of M3 away

4-13
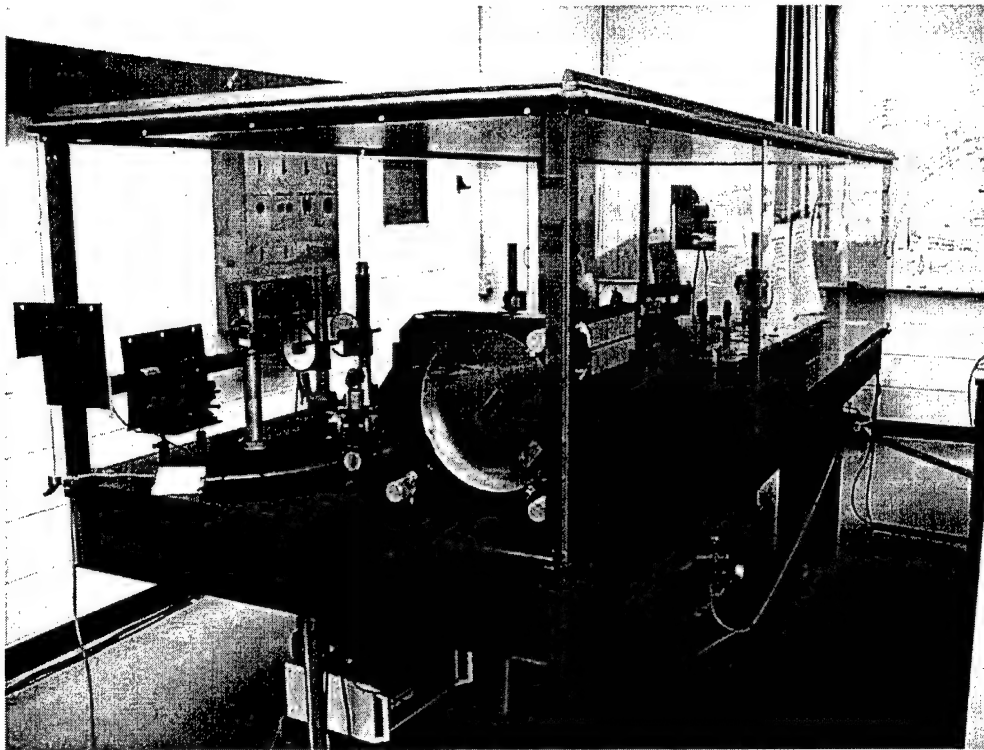
Figure 4.13   Optical System with Enclosure

from M3 minus the focal length of L2, as the focus of the parabolic mirror must align with L2. Mirror M1 is placed further along the negative x axis, in-line with both M2 on the x axis and the laser along the z axis. Beam height from the laser to M1, M2 and M3 is easily determined by running an adjustable iris centered on the optical axis, here 20.5 cm, along the path and correcting for any deviations with tip-tilt control of M1 and height adjustment of M2.

The beam splitter cube is then place in the system between M1 and M2 at the optical axis height. The split portion of the beam is sent to a reference mirror (M4) at the end of the optical table. The reference leg is not complete at this point, as an additional reference mirror is required for the reference leg to match the optical path length of the signal arm. Mirror M5 is added 259.5 cm from M3 to equal the signal arm path length of 940 cm. The cube must be level to ensure the optical height from the table is maintained. Variations in cube tip will contribute additional wavefront aberration to the test object image, and will complicate signal beam and reference beam alignment. The beam is verified to be level in

4-14

the system with the aid of one or more irises adjusted to center on the optical axis height and sampling beam travel.

4.4.2 Collimation and Expansion.

Once the beam is level, intermediate optics are added for beam expansion and collimation. The spatial filter is placed first to remove beam variations in the system and provide initial beam expansion. The spatial filter (figure 4.5) is placed in the beam with the objective completely defocused. The pinhole is adjusted with x and y axis micrometers until light emerges. Then the objective is slowly brought into focus with the z axis micrometer while simultaneously adjusting the x and y micrometers to for optimum light transmission.

Expansion of the Airy disk from the spatial filter is stopped by the aperture of L1 which is placed in the z-plane of the spatial filter and the beam splitter cube. The lens L1 is adjusted in the x direction until a collimated beam at the diameter of L1 (2.5 cm) is produced and verified by a shear plate or collimation tester. Proper alignment includes collimated beam output from both transmit sides of the beam splitter. Therefore, the beam should be collimated from L1 to the splitter, from the splitter to M4, and from the splitter to L2. Further, if the input to the splitter is truly collimated, and the splitter induces no focus to the wavefront, the beam between M4 and M5 should remain fairly collimated.

Collimation is verified by using a shear plate. A shear plate acts as a shearing interferometer, using flat glass with one side inclined at a slight angle, or wedge. The basic method of shearing interferometry involves displacing the wavefront laterally by some amount and obtaining the interference pattern between the original and displaced wavefronts. A flat glass plate with planar parallel sides will allow wavefront displacement when tilted in the beam. A wavefront will be reflected on both the front and rear surfaces of the lens as shown in Figure 4.14 when the wavefront is incident at 45 deg to the plate. Fringes will appear in the overlapping portion of the beam. If the wavefront is not planar, near vertical fringes will result. As the wavefront radius increases, the wavefront becomes more planar until it matches the planar faces of the plate and the fringes move towards horizontal (Figure 4.15(a)). The wavefront is considered collimated when the fringes are
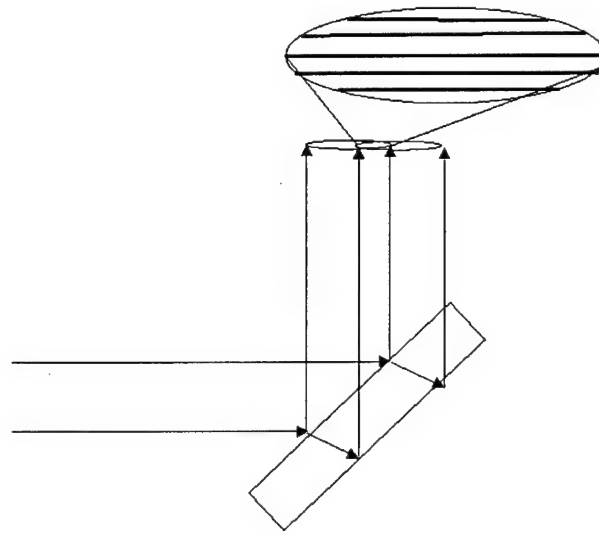
Figure 4.14   Lateral Shearing Interferometer

horizontal and parallel to the direction of shear as shown in Figure 4.14 and Figure 4.15(b).
As the wavefront radius expands through the point of wavefront collimation, fringe tilt
moves past parallel as shown in Figure 4.15(c). The shear plate used in this research was
the Continental Optical (CT-50), which has a reference bar along parallel in the glass for
easy fringe matching and includes a wedge angle on one of the glass planes which separates
the sources vertically for increased fringe spacing and thus instrument sensitivity. The
CT-50 collimation tester and planar glass lens used to test system collimation are shown
in Figure 4.16.

The next optical element in the system expands the 2.5 cm collimated beam produced
by L1. Lens L2 is placed to focus its output (10 cm focal length) at the focal length of
the parabola. The beam expands through focus and is turned to the parabola with the
one inch diameter M2. A visual aid in alignment involves covering the parabola with lens
paper which diffuses the light, showing the extent of parabola illumination. When the
beam is the diameter of M3, there will be a near collimated 12.5 inch output towards the
test object. This is verified with the shear plate and adjusted by slight adjustments in the
x direction to M2.

4-16

Figure 4.15   Lateral Shearing Interferograms ((28))

Figure 4.16   Collimation Test Lenses

The splitter combines the output of the signal and reference arms into the image plane. Lens L3 focuses this image to reduce the beam diameter in size from 2.5 cm diameter, and lens L4 collimates the beam at a 1 cm diameter, the input diam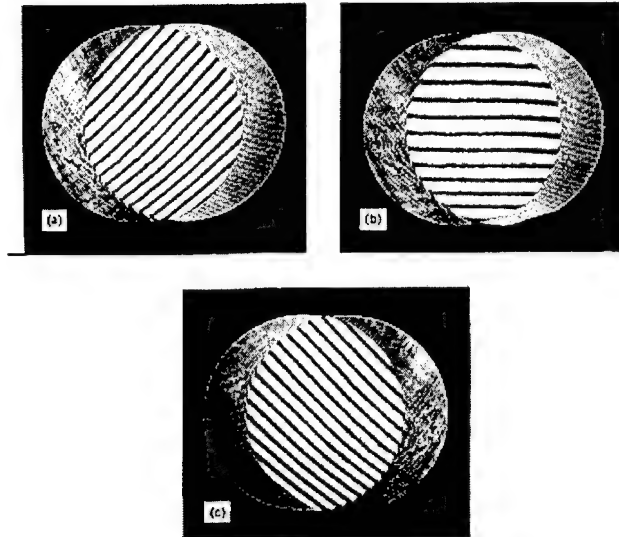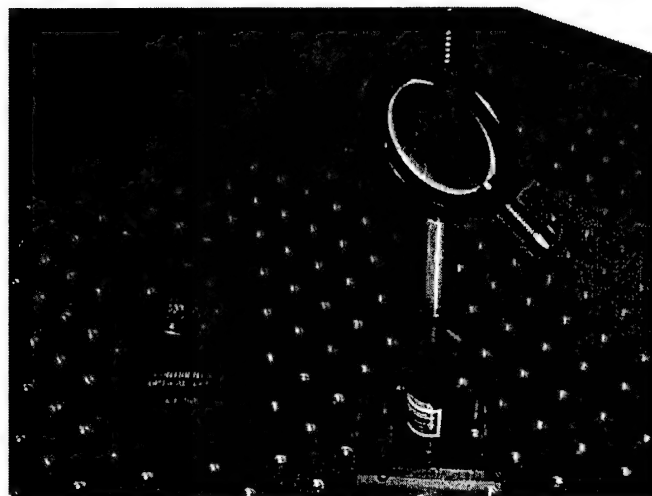eter for the Wavescope system. Again, collimation must be verified with a shear plate. The distance between L3 and L4 is a function of the individual focal lengths and the required output beam diameter.

This optical system generates finite image location, and determining this location is critical for proper placement of the imaging device, whether the CCD camera or Wavescope sensor head. Image location is found from matrix analysis methods (Section 3.4.4), and verified with an AFRL ZEMAX imaging system analysis model. Using the 2x2 refraction and transfer matrices, a system matrix was composed (Appendix A), principle image planes were calculated, object distance was entered, and image location was calculated using Mathcad. This model makes a very useful tool when either changing optics or distances between optics, as the output indicates whether an image will be formed in the image plane (positive value), and where to place the detector in the image plane. For the primary system setup, the image was located 6.3 cm to the right of L4. Actual adjustment of both the CCD camera and Wavescope confirmed this value. A stairstep pattern was cut from paper and covered part of the mirror at the test object location. When the step image was sharply defined, the mirror was in focus. A cursory ZEMAX Optical Design software model of this system was built which confirms this calculation.

4.5 Membrane Mirror Construction

Membrane mirrors were constructed for this research using Upilex membrane material coated with reflective aluminum bonded to a thin polyvinylide flouride (PVDF) sheet which provided mirror actuation with applied voltage.

4.5.1 Material Properties.
Upilex polyimide film, made by Ube Industries Ltd. (Japan), is a 125 μ m thick film used in aerospace applications with average surface roughness less than 3 nm (3). It has a high tensile modulus ($930\frac{kg}{mm^2}$), low water absorption, high radiation and chemical resistance, and low heat shrinkage (43). Upilex is somewhat

transparent, and was therefore coated with aluminum to enhance reflectivity. Coated Upilex material used in this research were unused portions of the material used in recent AFRL studies (23).

The PVDF film sheets used were manufactured by Measurement Specialties, Inc. The PVDF used in this research had the following properties (34):

Table 4.1   PVDF Material Properties

Young's Modulus	$2 - 4x10^9 \frac{N}{m^2}$
Piezo Strain Constant	(d_{33}): $23x10^{-12}\frac{C/m^2}{N/m^2}$
Electromechanical Coupling Factor	(K_{31}): 0.12
Maximum Operating Voltage:	$30\frac{V}{\mu m}$ (1560V for this thickness)
Thickness of Material	$52\mu m$
Typical Electro-Mechanical Conversion(s)	$25, 33x10^{-12}$m/V (1,3 direction)

4.5.2 Membrane Tensioning and Assembly.   Membrane tension was found to be the single most important element in mirror design and assembly. Without appreciable, uniform tension, a large wavefront deviation will result from the non-planar membrane surface which will not allow the system to image the surface (as discussed in Chapter 5). The first step in membrane tensioning was the design and construction of a membrane stretching test tool, patterned after an AFRL/DE design (9). The stretching ring test tool was constructed of 7075 T-6 aluminum, and provided a bonding surface to the membrane material after providing a uniform radial stretch. The 14 inch diameter stretching ring was designed to provide an epoxy application surface with excess epoxy runoff areas and a mount for a $\frac{1}{2}$ inch O-ring to extend 0.020 inches from the aluminum stretching ring surface, depicted in Figure 4.17 and shown in Figure 4.18, shown after seven stretching cycles. Grooves were cut in the wall of the O-ring support area to prevent rolling of the O-ring in the stretching ring mount given stretching ring pressure, resulting in O-ring expansion and membrane stretch radially away from the center.

Evaluation of the membrane mirror in the system could only realistically be accomplished with tip-tilt control to properly align the mirror in the system. Six inch membrane mounting rings were designed and fabricated to fit the Newport SL15ABM kinematic mir-

Stretching Ring

Side View: **Exploded View:**

O-Ring Rotation Stop

O-Ring Area

Membrane Contact Surfaces

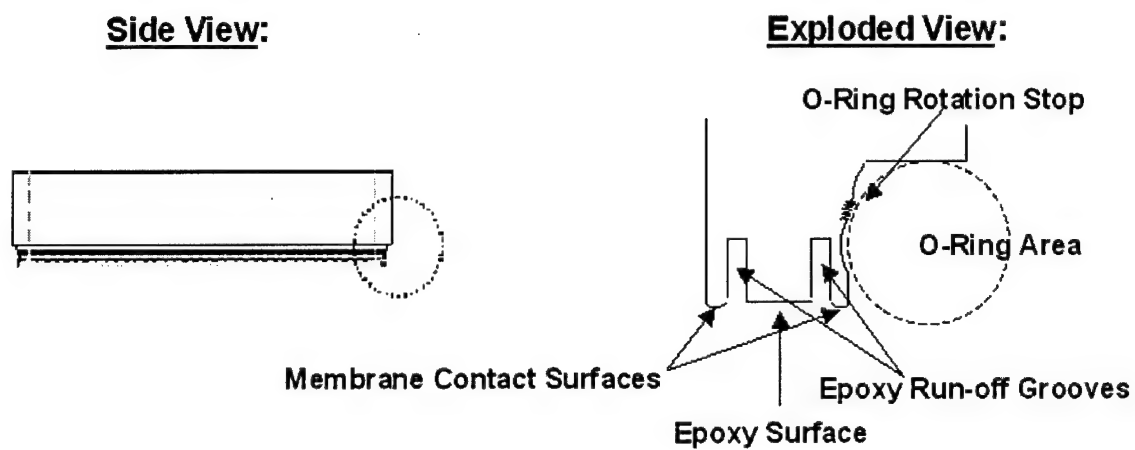Epoxy Run-off Grooves

Epoxy Surface
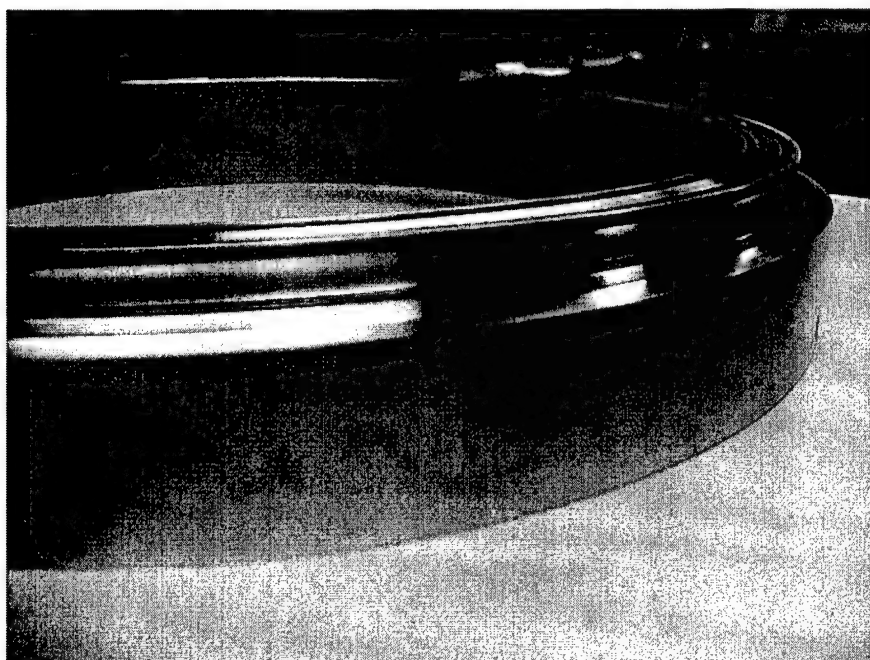
Figure 4.17   Stretching Ring Schematic

Figure 4.18   Stretching Ring after Seven Cycles

ror mount. These rings were designed (Figure 4.19) with an epoxy area and excess runoff, which is of increased importance to imaging the membrane. Excess epoxy build-up would create membrane surface distortions that could result in severe wavefront distortion. The membrane contact surface of the mounting rings was polished planar to sub-micron tolerances using a vibrating orbital polisher (Figure 4.20), which reduced mechanical distortion of the membrane due to the membrane mount. The rings incorporated additional design considerations for mechanical support of electrical wiring, to include a wire support trench cut across the depth on the outside diameter, and three screw-in aluminum wire support straps on the back of the rings.

The mounting procedure involved placement of aluminum coated Upilex material on a table covered with a pane of clean, flat glass. Slow-cure epoxy was applied to a clean (mechanical surfaces cleaned with acetone) stretching ring. A stretching O-ring was fabricated (vulcanized) from $\frac{1}{2}$ inch cord stock, and integrated to the aluminum stretching ring. The assembly provided a uniform stretch to the membrane material (Figure 4.21), due to O-ring outward radial roll when the stretching ring was pressed to the glass. Grooves in the stretching ring (Figure 4.18) added a "bite" to the O-ring ensuring outward roll vice O-ring slip simply inside the mounting ring support. Sixty pound weights provided a constant downward force on the stretching ring throughout its sixteen hour cure.

After a complete cure, the stretched membrane assembly was inverted to a drumhead configuration and the rear (uncoated) Upilex surface cleaned with acetone. The bonding side of the PVDF controller film was coated with 3M Super-77 spray adhesive, then bonded to the Upilex. Bond discontinuities were minimized by rolling a six inch rubber printmaking brayer for at least two minutes during bond cure, as shown in Figure 4.22. The mounting ring is the final element to be bonded to the assembly. Epoxy was applied to the center epoxy channel on the ring (Figure 4.23, then the ring was placed at the center of the drum-head and weighted with additional rings as shown in Figure 4.24 during the sixteen hour epoxy cure. The membrane was cut outside the diameter of the stretching ring to remove the mounting ring. The mounting ring was then trimmed and placed into a kinematic mirror mount. Two mounts were used in the overall process: one

Membrane Mounting Ring

optically flat
surface
(front)

14 cm

15.2 cm

2.5
cm

Membrane Contact Side

0.038
cm
.015"

0.5 cm

.2 cm   .2 cm

.2 cm   .4 cm   .2 cm

Epoxy Surface

2.5 cm

2.462 cm

2.0 cm

Membrane Contact Surface
(Optically Polished)

1.2 cm

Material: 7075T6 Aluminum
15.2 cm outer diameter
14 cm inner diameter
2.5 cm deep
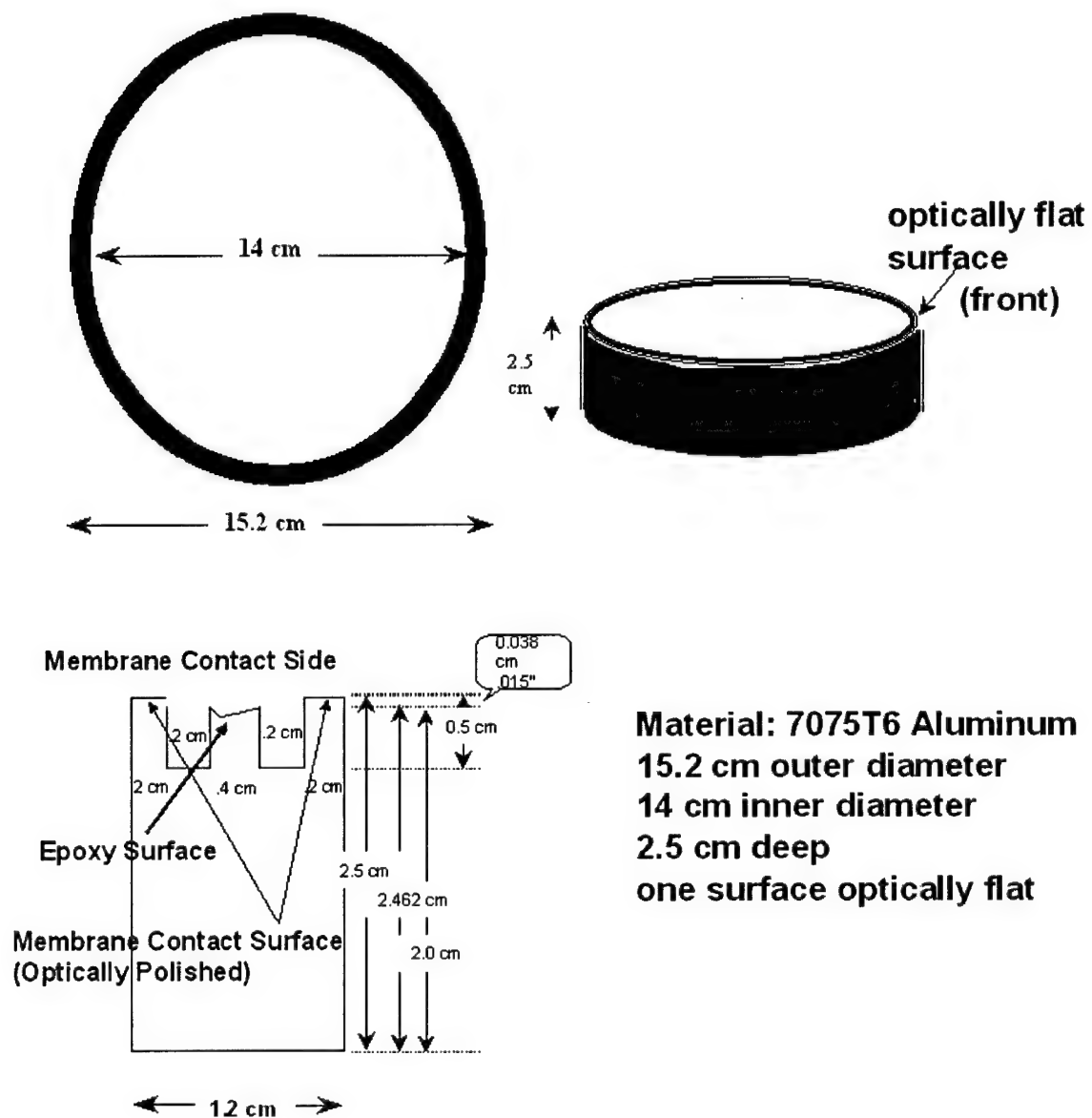**one surface optically flat**

Figure 4.19   Membrane Mounting Ring

Figure 4.20   Mounting Ring Surface Polishing
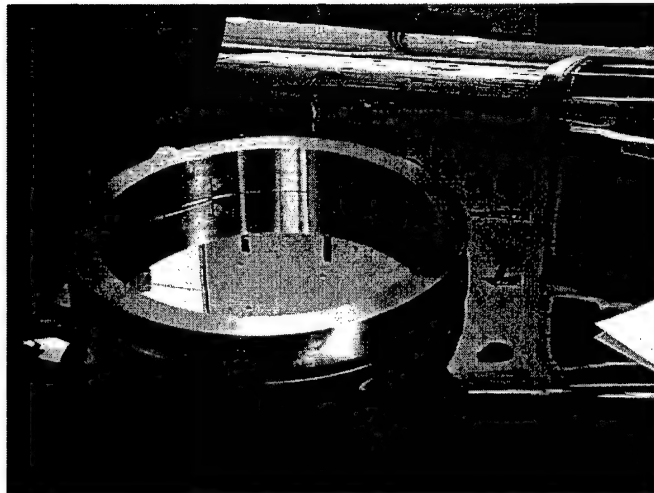

Figure 4.21   Stretching Ring Operation

Figure 4.22   PVDF Bonding to Membrane

Figure 4.23   Epoxy Application to Mounting Ring

Figure 4.24   Mounting Ring Cure

was used to provide a mount to bond electrical actuation wiring to the membrane, and the other used in the optical system for membrane surface characterization and deformation.

The importance of bonding the mounting ring to a stretched surface must be emphasized. It was found through experimentation that the mounting ring should be bonded directly to the Upilex film. Three failed attempts to create a full aperture PVDF controlled membrane resulted due to a mounting ring bond to either a non-planar surface or a surface without enough tension. The non-planar condition was created by bonding a small portion of the ring over a thin copper foil strip, placed to contact the PVDF electrode on the bonded side. Surface discontinuities and "print through" of the foil strip prevented obtaining any image information. In two other attempts, the mounting ring was bonded directly to the PVDF area, which meant the bond of the Upilex to mounting ring was held by the Super-77 only once the mounting ring separated from the stretching ring. This bond allowed a shear lag through the bond layer, reducing the prestrain induced by the stretching ring. The Upilex then relaxed, inducing surface deformation which produced large wavefront aberrations when illuminated. These aberrations were too large to return a coherent image of the surface, and no surface data could be obtained. Membrane data could only be obtained after the PVDF film was trimmed past the inside diameter of the

mounting ring as shown in Figure 4.24, where the mounting ring is cured directly to the Upilex, retaining the prestrain when cut from the stretching ring drum-head.

4.5.3 Membrane Control.
Mirror control was provided by a 52μm thick sheet of PVDF film, as mentioned in the above sections. This film expanded in one (unimorph) direction with applied voltage. This research was designed to develop a system to determine of the degree of membrane deformation. Therefore, different designs were incorporated in an attempt to gauge the level of membrane control. The promising property of a PVDF film contoller is the ability to localize control through electrode etching. Similar to developing electronic circuit boards, a photoetching process was used to remove portions of the NiCu conductive surface on one side of the film, which isolates electronic potential within any enclosed area.

The challenge was to develop a photoetching process for film sheets of at least six inches. Printed circuit boards are much more rigid and usually of much smaller dimensions. Therefore, a new method was developed to place a uniform coat of photoresistant on a 5.5 x 8 sheet of PVDF, where the sheet was clamped, weighted, and placed in a modified metal container (22). The chemical cure process of photoresist occurs when exposed to air. To create a uniform coat on the PVDF film, a clock secondhand motor was used to slowly pull the film from the photoresist container. The photoresist was then dried on the film at 65 deg C for 30 minutes, with care taken to not expose the film to sunlight or excessive room light.

Three patterns were developed for experimentation and expanded to a 20 x 20 size (Figure 4.25) due to meet the minimum 5x reduction size on AFIT's photomasking development camera for a 4 x 4 plate. A 40 minute exposure with 10 minute developing time was used to obtain necessary image contrast using Kodak high resolution plates (41).

The photomask images were exposed on the photoresist coated PVDF film with a 40 second exposure to a 350 Watt Mercury lamp using a Karl Suss mask aligner. This procedure removed the photoresist in the desired pattern area, which would then be subjected to an etchant to remove the conductive NiCu in that region. The development and
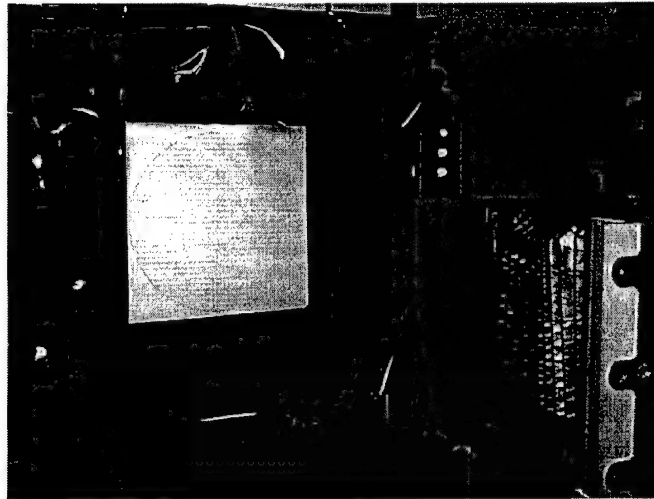
4-26

Figure 4.25   Photomask Imaging

exposure times were found after many trial runs, with the exposure above producing good line definition when examined under a microscope.

The patterns tested involved a center square and multiple squares as shown in Figure 4.26. The exposed PVDF film (Figure 4.27) was put into a 65 deg C oven for 45 minutes to remove any residual water prior to placing in an etching solution of Ferric Chloride and deionized water, mixed at a 3:1 ratio (respectively). The ratio was determined from trial runs to achieve a 25 second etch rate. It was found that longer etch rates were destructive to the desired pattern due to water lifting the photoresist. After microscope verification ensured proper pattern etch, acetone was used to remove the remaining photoresist from the PVDF film. The film was then cleansed with water and patterns tested for continuity with a multimeter. If the etched patterns separated the current path, they were entered into the bonding process.

Membrane control was attempted with etched PVDF film patterns. A challenge within this process was proper wire bonding to the PVDF pattern areas which provided a good wire bond but did not resist membrane motion or add to the deviation of "print through" the membrane. Several techniques were attempted, including soldering at various temperatures, soldering the wire to thin copper tape then bonding the tape to the membrane, employing conductive epoxy, and using various types of tape to bond the wire
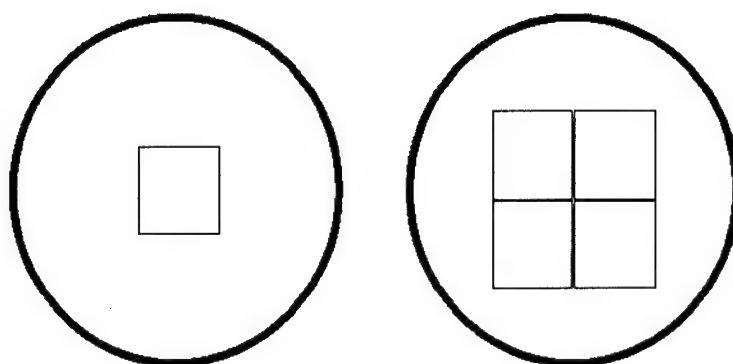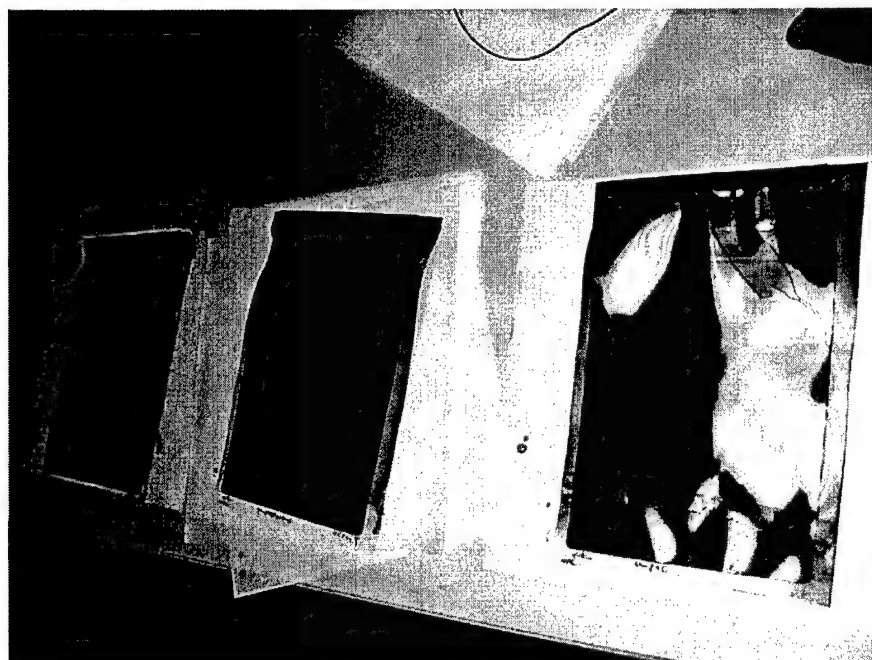
Figure 4.26   PVDF Etch/Test Patterns

Figure 4.27   Exposed Patterns in Photoresist on PVDF

to the surface. The method of providing voltage to the front of the membrane, which was bonded to the Upilex surface, was to run an extra strip of the PVDF out from the inside diameter of the mounting ring and use conductive epoxy to bond a wire to this strip. The strip became the ground plane for safety considerations, as it could come into contact with the mounting ring. This completely removed the ground wire from any possible print through. To excite regions of the membrane with positive voltage, however, wires were required to be bonded directly to the region in the rear of the membrane imaging surface. The wire straps designed in to the mounting ring offered mechanical support in reducing wire print through, however all methods exhibited print through problems except single wire strands bonded with transparent tape.

4.6 Summary

A Twyman-Green non-contact surface imaging system was constructed which allows measurement of up to 12 inch membrane mirrors. The optical setup was designed to output collimated light to allow interchangeability with either a CCD camera for interferometry, or the Adaptive Optics Associates (AOA) Wavescope for Shack-Hartman wavefront sensor measurements. System calibration results are discussed in Chapter Five.

Optical quality controllable membranes were constructed with non-adaptive control and varying degrees of adaptive control, determined by dividing the PVDF control film into regions using a photoeching technique. Each mirror assembly will be discussed in the following chapter.

V. System Performance Results

5.1 Overview

A large diameter (12.5") optical surface analysis system was designed, built, and tested. A known glass mirror surface was imaged by the system, which produced comparable results using two different wavefront analysis methods, interferometry and Hartmann wavefront sensing. These results compared favorably to tests of the same surface with a Zygo interferometer. Several membrane mirrors were constructed and analyzed by the system, proving both membrane mirror control and zonal membrane mirror control is possible with a PVDF film controller and applied voltage. Significant insight into membrane mirror construction and tensioning was obtained, which provides focus to any future research in this area.

5.2 Optical System Calibration and Performance Results

After component placement and system alignment, calibration of the system was conducted by testing system metrology performance against a known source. This system was calibrated using a Newport six inch round (60Z40) mirror with surface flatness of $\frac{\lambda}{20}$, which was placed in a kinematic mirror mount (Newport SL15ABM) with micrometer adjustment. The system produced straight and well-spaced interferometric images when a wavefront tilt was applied as shown in Figure 5.1. The APEX interferometry program produced output as shown in Figure 5.2, and wavefront map (Figure 5.3). Surface metrology characteristics were calculated using both the APEX interferometry program, the Wavescope Shack-Hartmann wavefront sensing technique, and compared to the AFIT Physics Department's Zygo Interferometer. The results compared favorably, and are listed in Table 5.1. Wavescope data is found in Figure 5.4, indicating Wavescope calculation areas, and Wavescope calibration data is in Appendix B.

These results indicated minimum aberration from optical elements within the system. The repeatability with different techniques and excellent comparison to the Zygo Interfer-
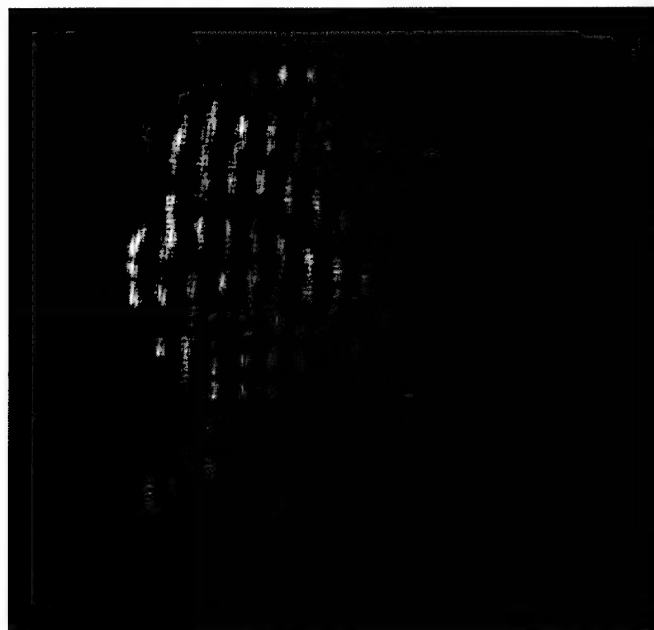
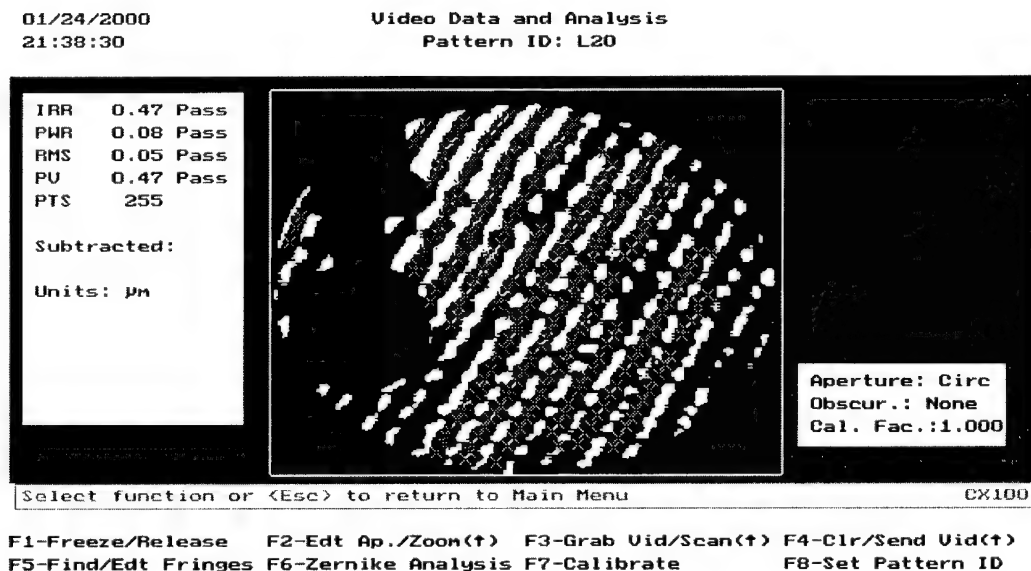Figure 5.1   Reference Mirror Interference Fringes

Figure 5.2   APEX Reference Mirror Surface Calculation
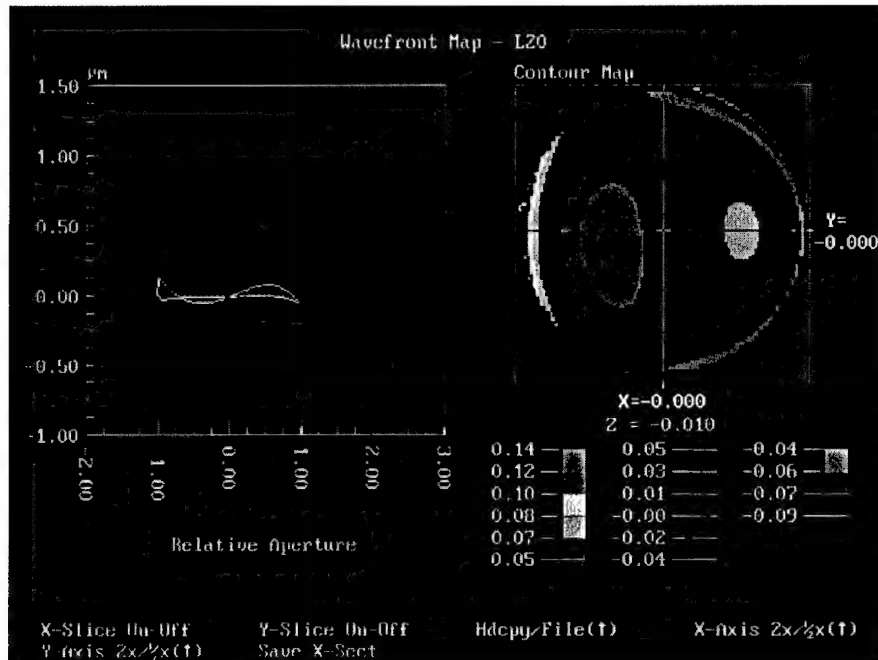
Figure 5.3   Reference Mirror Wavefront Map

Table 5.1   System Calibration Results, Deviation from reference, μm

Test	PV deviation	RMS deviation	Spherical Aberration	Coma	Astigmatism
Interferometry	0.26	0.05	0.01	0.01	0.01
Wavescope	0.367	0.06	0.03	0.01	0.042
Zygo	0.258	0.035	0.027	0.002	0.016

ometer demonstrated that the measurement system was able to accurately calculate test mirror surface properties.

5.3   Membrane Mirror Analysis

5.3.1   Mirror 1: Upilex only.   The first membrane mirror was made using Upilex coated with aluminum to enhance reflectivity and avoid intensity losses. The mirror was tensioned using only the weight of its mounting ring on the inverted stretching ring "drum head." Even though mirror deflection was not possible, the mirror produced the best surface quality results. No significant aberrations were noted upon viewing the surface, and reflected images retained image quality as shown in Figure 5.5.

5-3

GRADIENT VECTOR DISPLAY

OPD WIRE DIAGRAM

STREHL RATIO
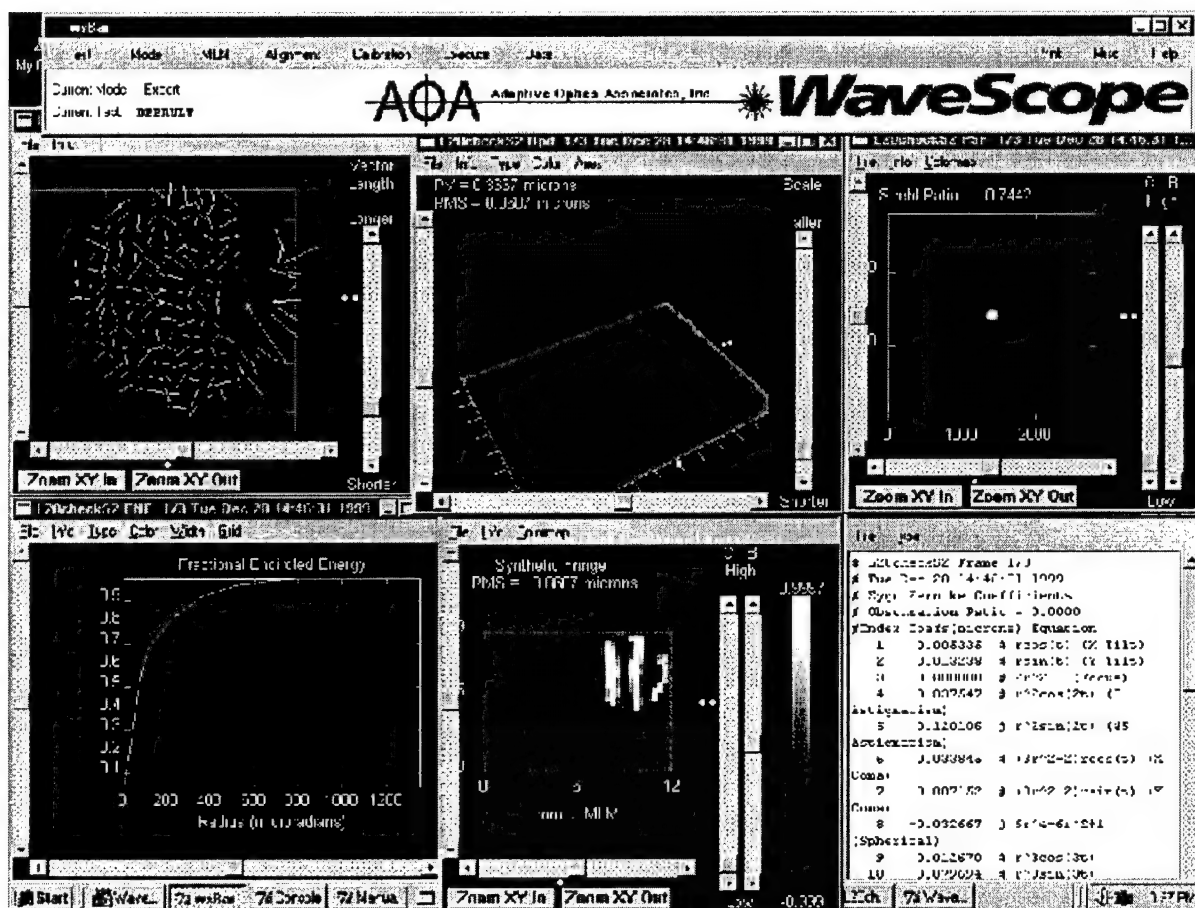
FRACTIONAL ENCIRCLED ENERGY

SYNTHETIC FRINGE DATA

ZERNIKE COEFFICIENTS

Figure 5.4   Wavescope Example Results

Figure 5.5   Reflected Image in Upilex-only Membrane Mirror

Interferometric surface fringes resemble those of the $\frac{\lambda}{20}$ mirror, as shown by the relatively straight fringe pattern spacing in Figure 5.6, with some aberration. Fringe spacing was maximized by minimizing mirror tip/tilt. The nine fringes near the center of the aperture indicate only a 4.5μm deviation over this area. This fringe spacing was the widest possible using the tip/tilt measurements on the mirror mount to reduce wavefront tip and tilt to a minimum. If the membrane mirror was planar, the fringes would disappear under this condition, and show either an all bright or all dark region. This "maximized" fringe spacing was too close for the APEX fringe analysis program to calculate the wavefront from the fringe patterns. Therefore, surface characterization was performed using the Wavescope system. Wavescope calculated surface deformation properties as shown in Table 5.2, with Wavescope output in Appendix B.

Table 5.2   Upilex-only Membrane Surface Metrology

Membrane Surface Property	Upilex-only Membrane
PV Deviation	10.25 μm
RMS Deviation	2.54 μm
Spherical Aberration	1.43 μm
Coma	3.56 μm
Astigmatism	4.86 μm

Figure 5.6   Interference Fringes on Upilex-only Membrane

Additional data was gathered on this membrane with a magnified pupil (as described in Section 5.3.4). The magnified pupil enabled more Wavescope subapertures, and thus a more accurate surface depiction according to the Wavescope output, Figure B.3 in Appendix B. This run indicated more surface deviation, but also provided a clearer picture of the cause. Nearly all this deviation is astigmatism, with the greatest aberration in 45 deg astigmatism, which is also observed when viewing the interferogram of the pupil (Figure B.2) . The fringes from the boundary represent those for astigmatism in Figure 3.14.

Table 5.3   Upilex-only Membrane, Magnified Pupil

Membrane Surface Property	Deviation from $\frac{\lambda}{20}$ reference (microns)
PV	30.88
RMS	5.3
0 deg Astigmatism	5.11
45 deg Astigmatism	-7.19
Coma (Y)	-1.55
Spherical	0.16

5.3.2   Mirrors 2,3,4: Full PVDF Membrane.

The second, third, and fourth membrane mirrors produced were all Upilex polyimide film membranes coated with aluminum and bonded to a PVDF sheet over the entire aperture using Super-77 and a brayer to provide even bonding. Construction of membrane two involved curing the mounting ring over a thin strip of copper tape as shown in Figure 5.7 to contact the conductive NiCu layer on the PVDF side bonded to the Upilex and provide a surface for a wire lead. However, the thin copper tape strip disrupted the uniform contact surface and imparted a significant deviation from planarity at the boundary of the membrane. As a result, the wavefront error was too large to even obtain an image, much less obtain interference fringes. However, wire lead contact with electrodes on each side of the PVDF is required, as PVDF motion is actuated due to the electric potential difference through the PVDF film thickness. The alternate method of bonding a wire to the membrane side of the PVDF was developed by extending the material to form a "flap" which was not bonded to the Upilex, to form a wire bond area. This method was used on membranes two and three in place of the copper tape. The mounting ring continued to be cured to
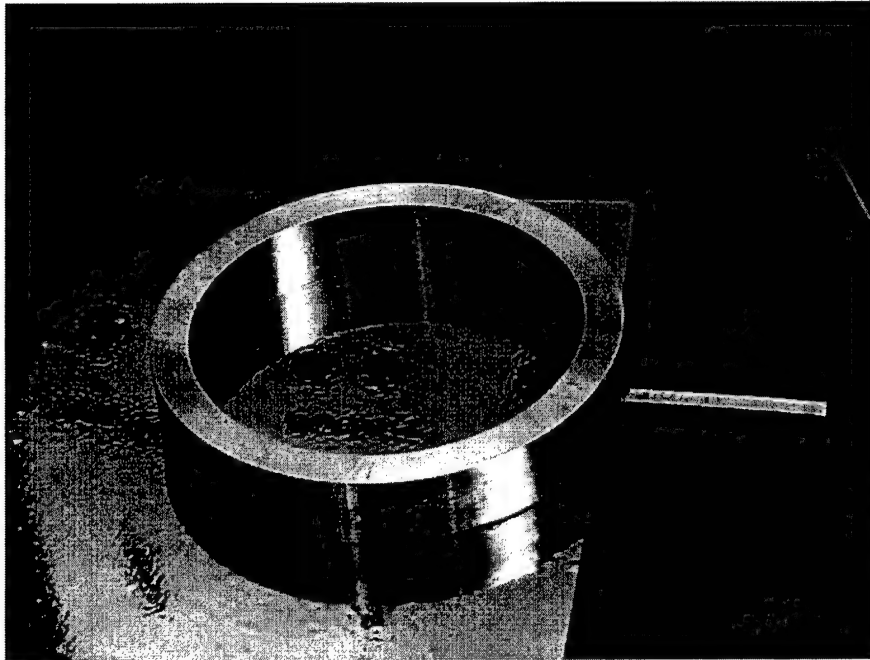
Figure 5.7   Mounting Ring Bonded to PVDF Layer

the PVDF surface, shown in Figure 5.7 (minus the copper strip). More weight (another mounting ring) was added to membrane three in an attempt to impart more surface strain, but both membranes two and three were unable to produce an image.

The problem centered around the mounting ring bond to the PVDF film. After mounting ring cure, the mounting ring with membrane was cut away from the stretching ring using the same procedure that was used in the construction of all other membranes. However, since the ring was bonded to the PVDF film, the Upilex pre-strain imparted from the stretching ring was not captured by the mounting ring. The Super-77 adhesive surmounted to an intermediate material layer between the two film layers which allowed strain relief. To avoid this problem, future membranes were made by only bonding a PVDF film layer to Upilex no greater than the inside diameter of the mounting ring.

5.3.3   *Mirror 5: Full PVDF Membrane.*   The first membrane bonded to PVDF which produced an image was the fifth membrane mirror constructed, which included the process improvements of trimming the PVDF control film to less than the inside diameter of the mounting ring and bonding the mounting ring directly to the Upilex

Figure 5.8   Membrane 5: Direct Bond to Upilex

surface, thereby retaining the pre-strain induced by the stretching ring, and extending an extra strip of the PVDF that was not bonded to the Upilex for wire bonding. 3M "Post-It" notes provided ideal protective coverage while applying Super-77 spray adhesive, as well as a temporary hold to the PVDF strip during conductive epoxy cure, as shown in Figure 5.8, which could easily be removed for installation and imaging.

The image of the membrane surface, while interpretable, indicated significantly more wavefront distortion than either the glass surface or the Upilex-only membrane. Interference fringes were obtained (Figure 5.9), indicating more surface deformation than previous surfaces. The cause of surface deformation is directly attributable to PVDF bonding, which produced localized strain "pockets," causing localized surface deformations resembling bubbling. Large surface deformations create phase cancellations in the wavefront and appear as dark areas. The largest of these areas, shown in Figure 5.9, is wire bond area of the input voltage wire to the membrane.

With this information, a different method of bonding PVDF to Upilex was attempted, with less than satisfactory results. Delayed cure epoxy was uniformly applied to the
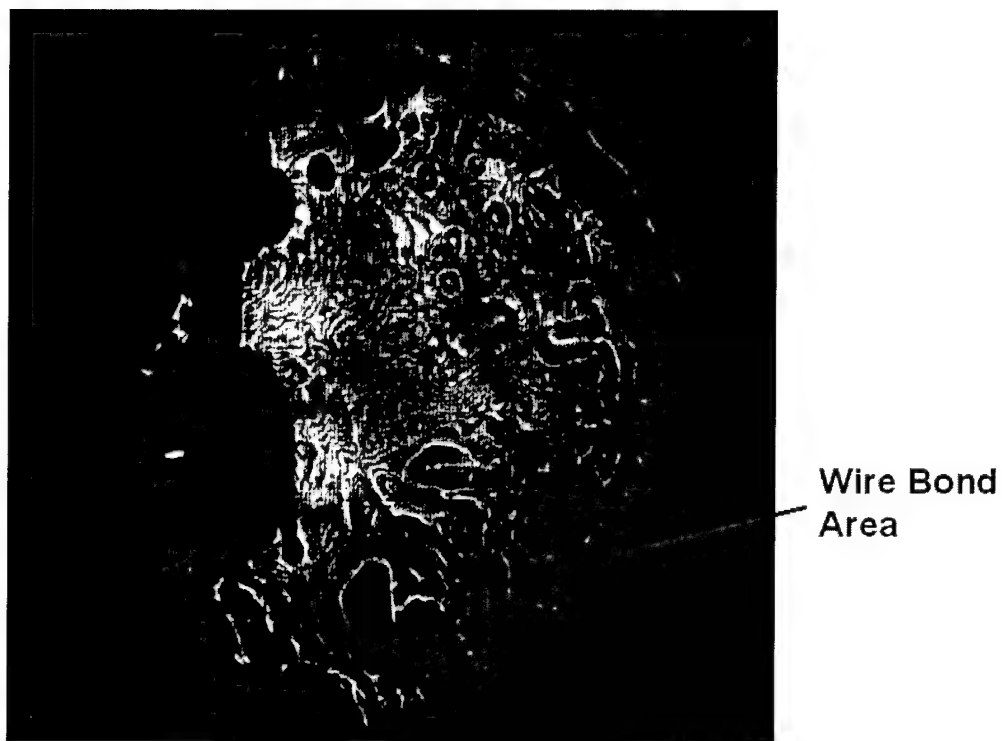
Wire Bond Area

Figure 5.9   Membrane Mirror Interferogram with Full PVDF Coverage

stretched membrane and then PVDF film applied. The brayer was then used in an attempt to uniformly spread the adhesive layer. After the composite cured, it produced more visible wavefront distortion with white light than the spray adhesive method.

Although the image was less than optimal, interference fringe contrast was present and fringes were observed. The PVDF film was then excited with voltage ranging from 100 to 500 volts, and fringe movement was easily noted, directly mapping membrane motion. Fringe motion can be observed in virtually any area of the membrane, but is more noticeable near the center. In Figures 5.10, 5.11, and 5.12, a region is identified which facilitates observation of membrane motion. Thirteen densely packed fringe pairs can be seen in figure 5.10 (a), indicating 7.5λ or 4.7 microns of deviation in this area. As voltage is increased, the fringes disperse, indicating the area is moving towards planar and decreasing local tilt. This trend continues until the 500 volt application (Figure 5.12 (b))

where a circular pattern is easily observed. The four central fringes in this area indicate a 2λ or 1.26 micron deviation, and a localized pocket creating circular fringes.

Wavescope data on this membrane was obtained (Figures B.4, B.5, B.6, B.7, B.8, and B.9 in Appendix B) which documents membrane motion. This data, however, was limited to the number of subapertures, or individual lenslet arrays, which were uniformly illuminated through the imaging system by the membrane. The pupil image, as seen by Wavescope (Figure 5.13), was not uniform and therefore could not uniformly illuminate all the subapertures in the Wavescope lenslet array. Therefore, data was limited to the lenslet arrays which observed wavefront deviation in the area covered by that specific lenslet. Lenslet coverage is indicated on the OPD diagram on the Wavescope images. These data points provided positive indication of membrane motion. Data is summarized in Table 5.4, and graphically represented in Figure 5.14.

Table 5.4   Wavescope Analysis of Full PVDF Membrane Deformation (microns)

Full PVDF Membrane	PV	RMS	Spherical	Coma	Astigmatism
0 V Input	41.5	11.6	-70.4	-51.5	-7.9
100 V Input	36.8	10.4	-41.7	-50.7	-14.3
200 V Input	33.4	9.4	-23.9	-57.3	-16.6
300 V Input	27.5	7.9	-24.2	-32.5	-15.7
400 V Input	24.5	7.1	-17.5	-44.1	-20.3
500 V Input	9.05	2.7	19.3	-40.1	-24.6

The Wavescope data indicates a flattening of the surface as voltage is applied, with a pronounced change in RMS deviation. There was a slight increase in the magnitude of astigmatism, and a pronounced change in spherical aberration. This indicates a "cupping" of the membrane, which was expected considering the fixed position of the membrane on the mounting ring boundary.

5.3.4   Mirror 6: PVDF Membrane with Square Etch Pattern.

Mirror six was constructed with the process improvements used to build mirror five, with another mounting ring added for extra weight during the Mirror 6 mounting ring cure. The interferogram, however (Figure 5.15), revealed even more surface deformation than

was apparent on Mirror 5, and was again largely attributed to the PVDF film to Upilex film bonding layer.

Fringe spacing was again too close for interferometry, and Wavescope was chosen to determine surface deformation. However, due to large light level variations across the aperture of Mirror 6, Shack-Hartmann analysis was not possible. The Wavescope system was able to produce only a few subaperture calculation areas over the membrane aperture and would therefore not be reliable as measurement data. Therefore, the optical system was rearranged to magnify the pupil in order to focus on the uniform light level in the center of the membrane aperture. Lenses L3 and L4 were reversed, and all elements from L2 to L4 were repositioned in order to produce an enlarged image. Image location calculations were performed with Mathcad (Figure A.2, Appendix A) and ZEMAX to verify image position with the new system. From this data, the splitter cube (and correspondingly M4 and M5) were shifted in the positive x direction to produce an image post L4. The system was rearranged and was recalibrated using the Newport six inch round (60Z40) mirror. Interferometric data (Figure 5.16) showed surface improvement over previous values, likely due to a significant image size increase, where the CCD camera sampled only the center of the mirror:

- Peak-valley surface deviation: 0.12 μm

- Root-mean-squared surface deviation: 0.02 μm

Wavescope data (Figure 5.17) nearly reproduced earlier system results (Table 5.1), and was able to evaluate more subapertures over the mirror:

- Peak-valley surface deviation: 0.391 μm

- Root-mean-squared surface deviation: 0.059 μm

With this recalibration, the magnified system was tested and the overall system performance was validated with the good correlation to earlier results.

With the membrane now magnified, interference fringes were apparent on Mirror 6, despite surface roughness, and translated with applied voltage in similar fashion to Mirror 5. Particularly of significance was the fact that center fringes showed the most

motion, proving that zonal control is possible with an etched PVDF film. With a 400 V sinusoidal applied voltage input to only the center square (etched) portion of the PVDF, the interference fringes in the center of the aperture moved a significant amount. The motion was easily seen with a 1 Hz input. Figure 5.18 shows interference fringes at +400 V. A dark region indicates local wavefront deviation outside the resolution of the optical system. This correlates to the direction of the poling direction of the PVDF which was across the aperture and slightly inclined. What we see is a "cupping" of the material, creating some 45 deg astigmatism across the aperture (due to curvatures of opposite sign (28)), along with 5-7 fringes of curvature next to this dark region. As the membrane cycled back to zero voltage , the deformation became resolvable and the dark area was replaced by approximately eleven fringes again indicating some astigmatism. The many circular fringes disappear and we see only two fringes over a large area. A noticeable change occurs when the membrane cycles to −400V, and a large (15 fringe) elliptical deformation is apparent with its major axis normal to the PVDF poling direction. This indicates a protrusion isolated to the active square region of the PVDF, which overcomes the astigmatism which was present in this region at 0V and enhanced at +400V.

Table 5.5   Wavescope Analysis of Center Square Etch Membrane Deformation(microns)

Voltage	PV Deviation	RMS Deviation	Focus	Astigmatism	Coma	Spherical
0	0.026	0.013	-0.03	0.024	-0.326	-0.13
100	1.041	0.52	2.97	-7.21	0.91	6.62
200	2.006	1.003	18.72	6.12	31.96	14.81
300	3.434	1.717	46.94	33	70.76	36.65
400	4.56	2.28	54.07	39.5	101.38	40.85
500	5.385	2.69	31.3	45.8	100.31	26.36

The revised system setup produced Wavescope subapertures in the center of the membrane, over the square etch and some just to the left of the square. Membrane deformation was calculated using the planar (0V) membrane as the reference. This had the effect of ignoring initial membrane shape and only tracking the deformation. Table 5.5 and Figure 5.21 document the motion observed by Wavescope, and show significant increases in coma, focus, spherical, and astigmatism aberrations, along with measured increase in PV and RMS deviation. The large coma value appears to arise from the location of Wavescope

subapertures which were used to calculate the measurement, which were biased on the left side of the square. With more even illumination, given less local surface discontinuities, a more accurate depiction of surface deformation would be obtained. The Wavescope image is inverted from the CCD image due to the additional lens on the Hartmann Sensor. The left side of the square corresponds to the (inverted) right side of Figure 5.18. The many fringes in this area give rise to the coma values obtained by Wavescope, which are caused by the increased astigmatism due to membrane bending normal to the PVDF poling direction. A snapshot in a small area near the border of the square, which amounts to a subaperture calculation, would indicate an increased coma.

5.3.5 *Mirror 7: PVDF Membrane with Four Square Etch Pattern.*

Mirror seven was constructed similar to mirrors 5 and 6, with the exception of additional wire bonding to the membrane. PVDF with the four square (Figure 4.26) etch pattern was bonded to the Upilex membrane using the Super-77 bonding technique. Upon composite membrane cure, a wire lead was bonded to the center of each square and a negative lead to the membrane side of the PVDF via the PVDF "flap." The composite membrane pupil image displayed more localized surface deviations, or bubbling, than previous membrane mirrors. The Wavescope pupil image (Figure 5.22) clearly shows this effect, which can only be attributed to the Super-77 PVDF to membrane bonding technique. The edge effects from the mounting ring bond are seen at the edge of the membrane, but dissipate fairly quickly into the even lighting area of the Upilex only membrane. Further towards the center, the PVDF diameter is clearly seen, along with the resultant effects of the PVDF bond. Wire bonding areas are observable, but not as apparent as on previous membranes, due to the many deformations caused by the PVDF bond.

Interferogram analysis of this membrane was achieved with the magnified optical system setup used to obtain Wavescope data for Mirror 6. Fringes were readily apparent and were able to indicate membrane motion. Each square region was excited independently to near ±650V, with PVDF poling direction in the negative Y direction, or horizontal across the membrane surface. Figure 5.23 shows the fringe pattern of the magnified membrane, with the four-square etch pattern superimposed, at 0 voltage. Localized bubbling is ap-

parent as circular fringes, with the largest deformations appearing as dark circular regions with many circular fringes. The upper left square in Figure 5.24, corresponding to the lower left square on the membrane surface, shows membrane motion after application of 650V to this area. The large ten fringe circular deformation in the positive Z direction (bump) was seen to disappear in the transition from 0 to 650V, and become replaced by a two fringe circular deformation in negative Z (dip). This motion is localized to the upper left square, and neighboring fringe patterns remain largely unchanged except for a two fringe difference near the border of the upper right square. When negative 650V was applied, each circular fringe (bump) region was accentuated, as shown in Figure 5.25, by at least three fringe pairs (3λ). Other regions experienced up to a two fringe increase in circular fringe areas, but motion was largely localized.

The intermittent nature of the spray adhesive creates pockets where the adhesive is not bonded to the Upilex. As the PVDF tension increased with positive voltage along the poling direction, these pockets were pulled taught with some localized bending. When the PVDF tension decreased with negative voltage, the pockets were accentuated. Each of the other square regions were activated with both positive and negative voltage, with corresponding figures in Appendix C, providing further indication of localized deformation.

Apparent on each interferometry plot was tight fringe spacing and areas of large circular deformation resulting in dark circular regions. Each of these conditions contributed to the inability of the optical system to determine degree of deformation, with the former condition hampering interferometry program analysis and the latter disrupting adequate Wavescope surface analysis due to uneven aperture lighting. The Wavescope run produced many subapertures over the outer Upilex-only region of the membrane and some in the interior surface which indicated deformation with applied voltage. However, adequate subaperture coverage of the membrane to indicate regional deformation was not possible due to the roughness induced by PVDF bonding. Therefore, additional Wavescope run information does not add to this analysis. Mirror 7 validated the zonal control ability of PVDF film. The degree of deformation and associated Zernike modes of PVDF film etched in a similar manner to Mirror 7 can be shown on future membrane mirrors once the PVDF bonding to membrane problem is solved.

5.4 Summary

The Twyman-Green optical system produced excellent results on the polished $\frac{\lambda}{20}$ reference mirror. Using different wavefront measurement techniques, the system produced similar results which compared favorably to Zygo interferometer data. System performance was validated after rearranging optical components, as reference mirror calculations were nearly reproduced.

Seven membrane mirrors were assembled using the techniques discussed in Chapter Four. Analysis by the optical system proved that membrane mirror deformation and zonal control is possible with PVDF film. Mirror 1 produced the best image, and all subsequent mirrors produced a degraded image as a result of the PVDF bond layer. However, even with degraded imaging, motion of 32 μm PV and 8.9 μm was identified using Mirror 5. Mirror 6 produced 5.1 μm PV and 2.7 RMS. Mirror 7 validated the ability to control local areas with a PVDF etch pattern, while Mirrors 2,3, and 4 helped establish membrane assembly techniques.

(a)
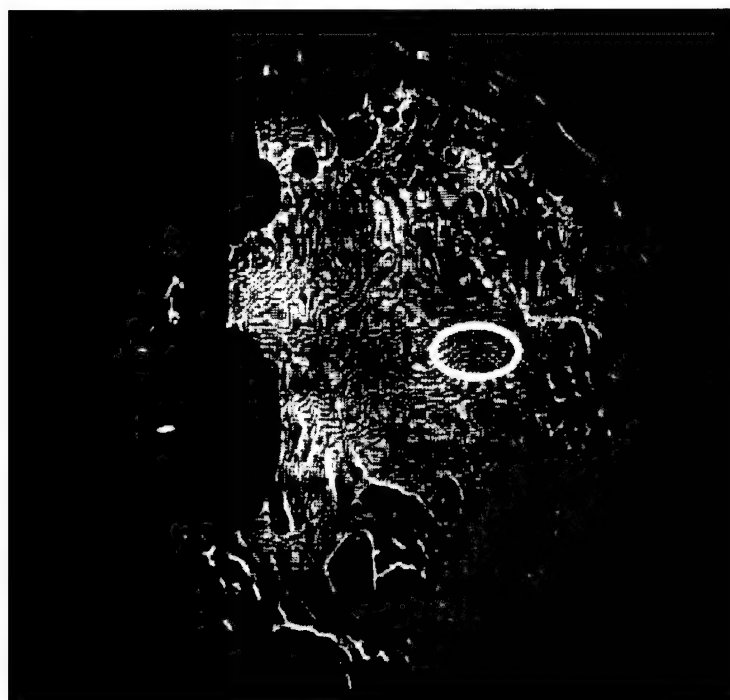
(b)

Figure 5.10   Membrane Mirror Fringes on PVDF with:(a) 0V input, (b) 100V input
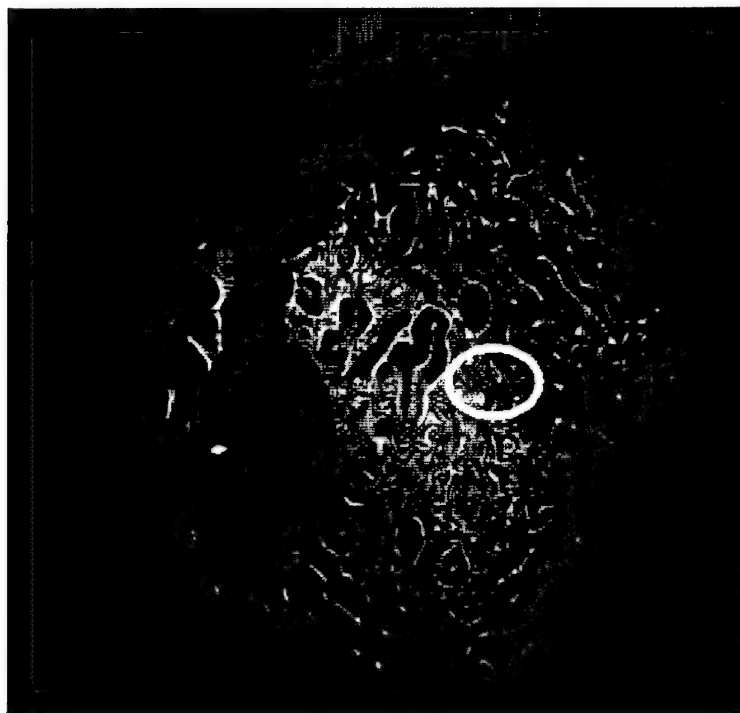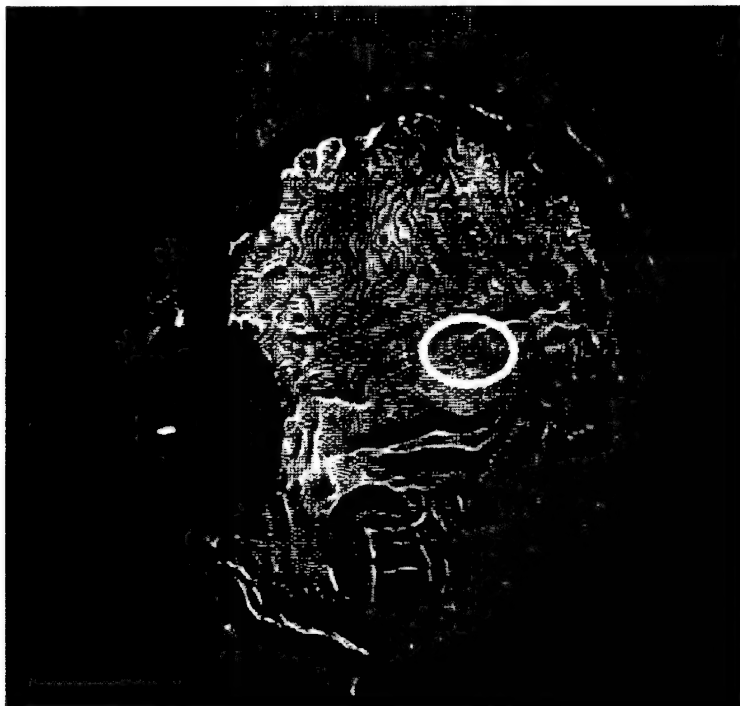
5-17

(a)

(b)

Figure 5.11   Membrane Mirror Fringes on PVDF with: (a) 200V input, (b) 300V input

(a)

(b)

Figure 5.12   Membrane Mirror Fringes on PVDF with: (a) 400V input, (b) 500V input
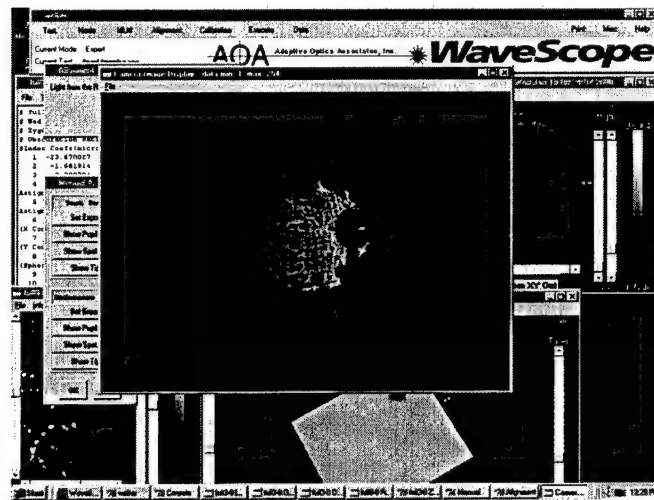
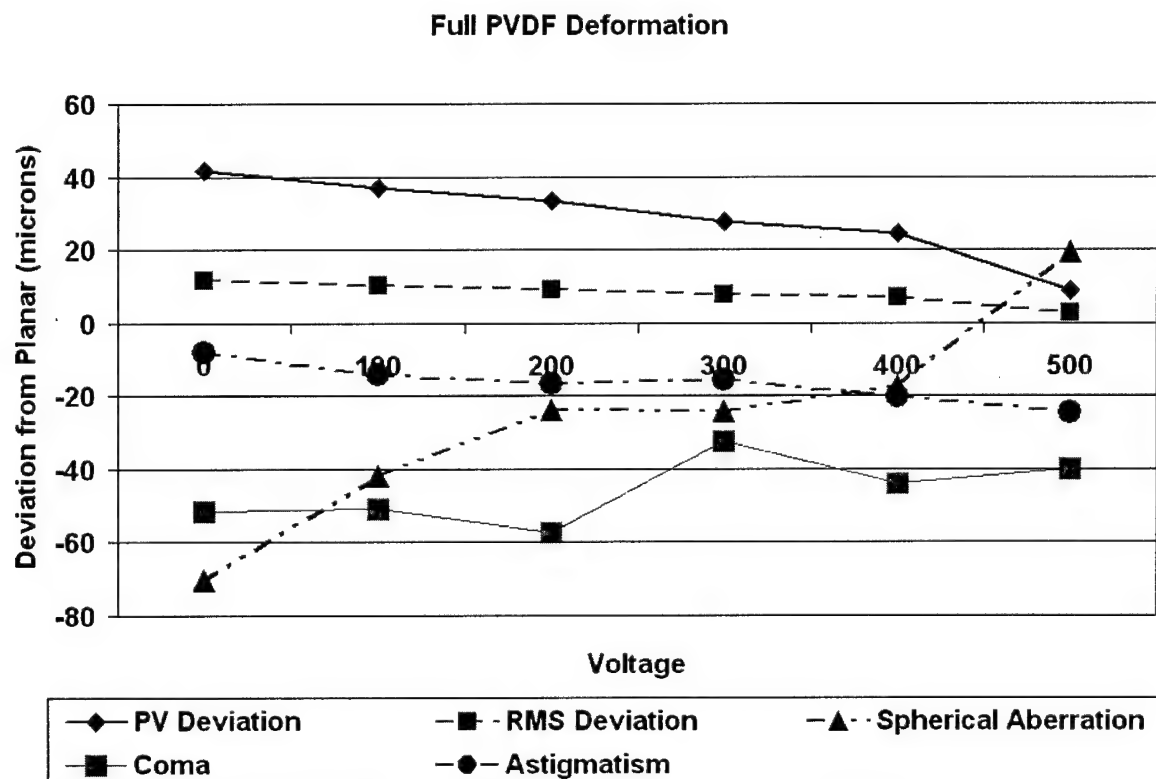Figure 5.13   Pupil of Membrane With PVDF as Seen by Wavescope

Full PVDF Deformation

Figure 5.14   Wavescope Analysis of Full PVDF Membrane Deformation

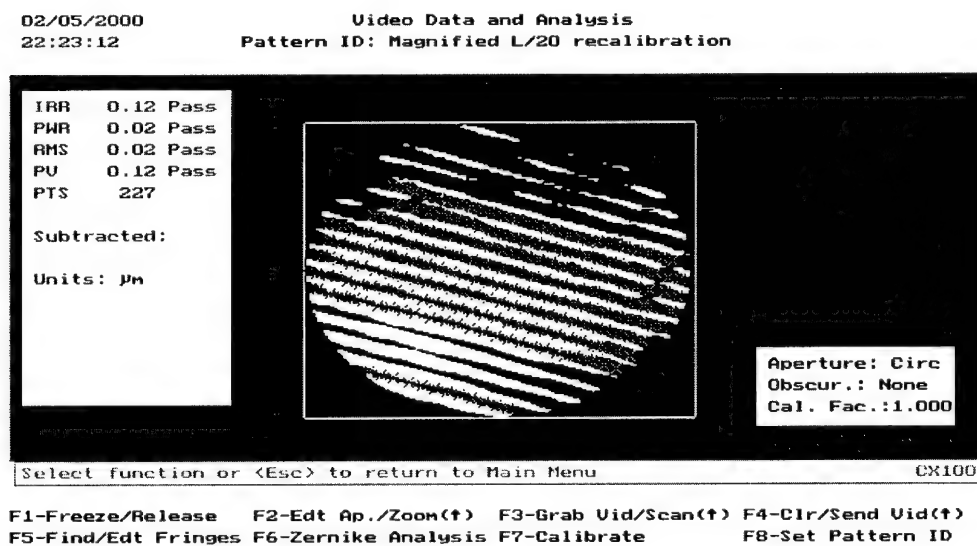Figure 5.15   Interferogram of Mirror 6: Full PVDF with Center Square Etch Pattern

Figure 5.16   APEX Recalibration Data, Magnified System

5-21

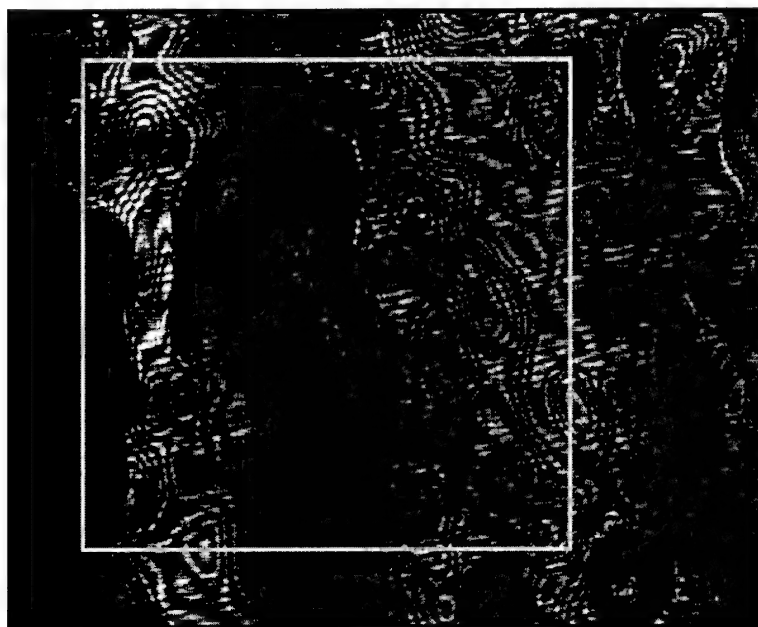Figure 5.17   Wavescope Recalibration Data, Magnified System
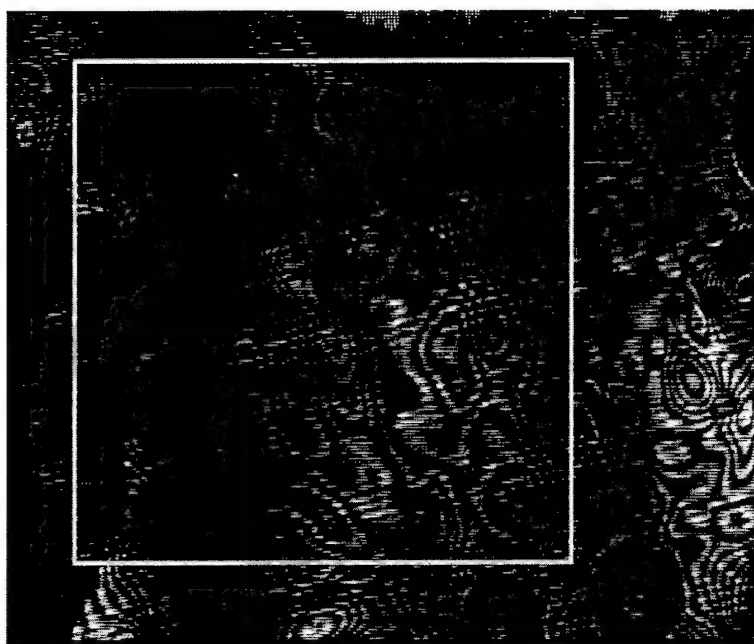

Figure 5.18   Square PVDF Region: 400V

Figure 5.19   Square PVDF Region: 0V

Figure 5.20   Square PVDF Region: -400V

**Wavescope Tracked Center Square Membrane Motion
(0V Membrane as Reference)**

Legend:
- —◆— PV Deviation
- ▲ RMS Deviation
- —■— ·Focus
- —※— Astigmatism
- —●— Coma (x)
- - + - Spherical

Y-axis: Deviation (microns)
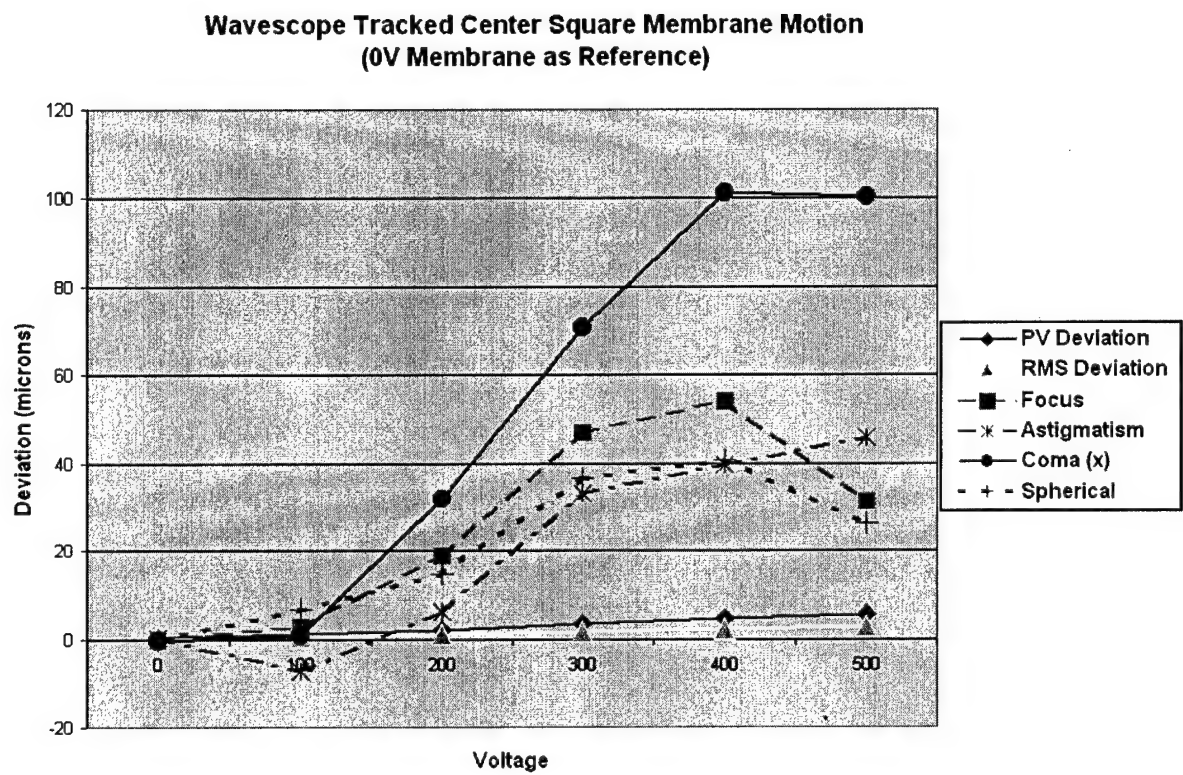X-axis: Voltage

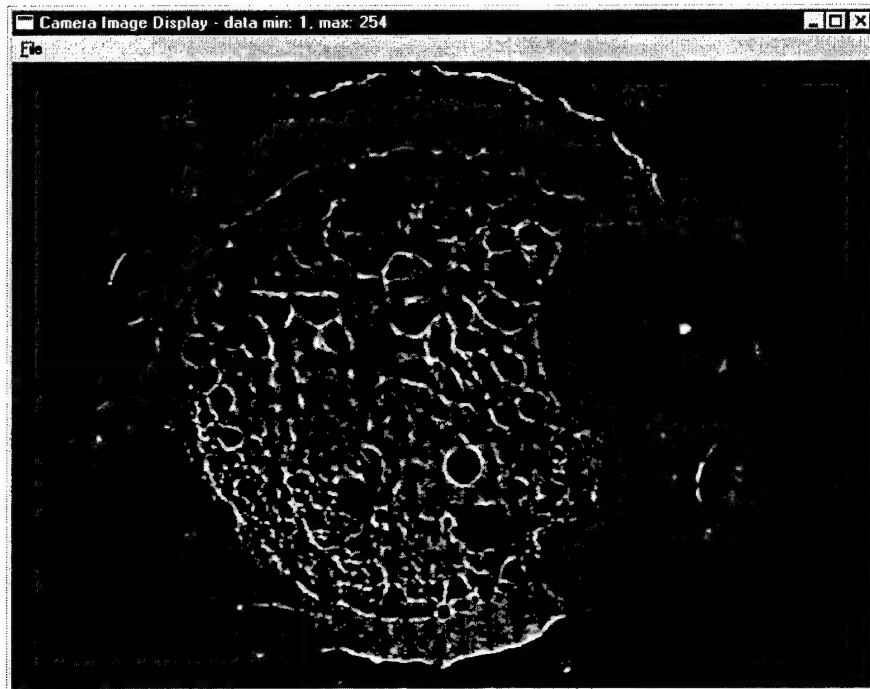Figure 5.21   Deformation of Square Etch with Membrane as Reference

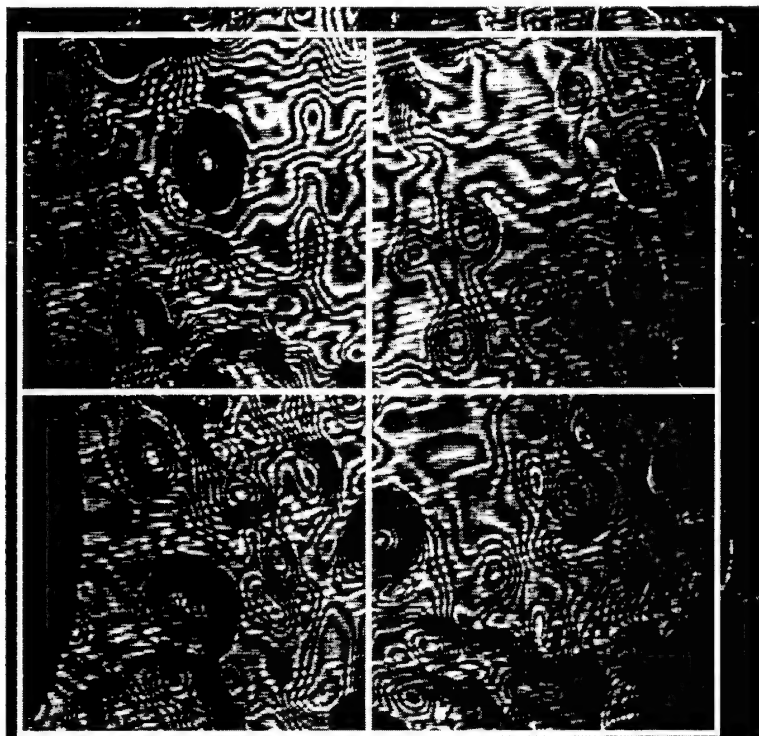Figure 5.22   Wavescope Observed Pupil of 4 Square Pattern

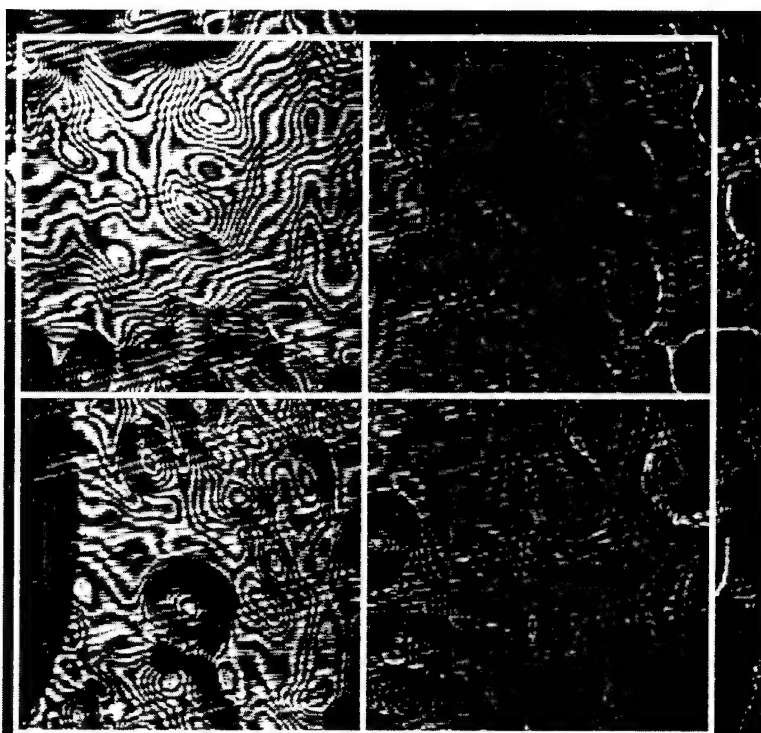Figure 5.23   Four Square PVDF Membrane, 0 V

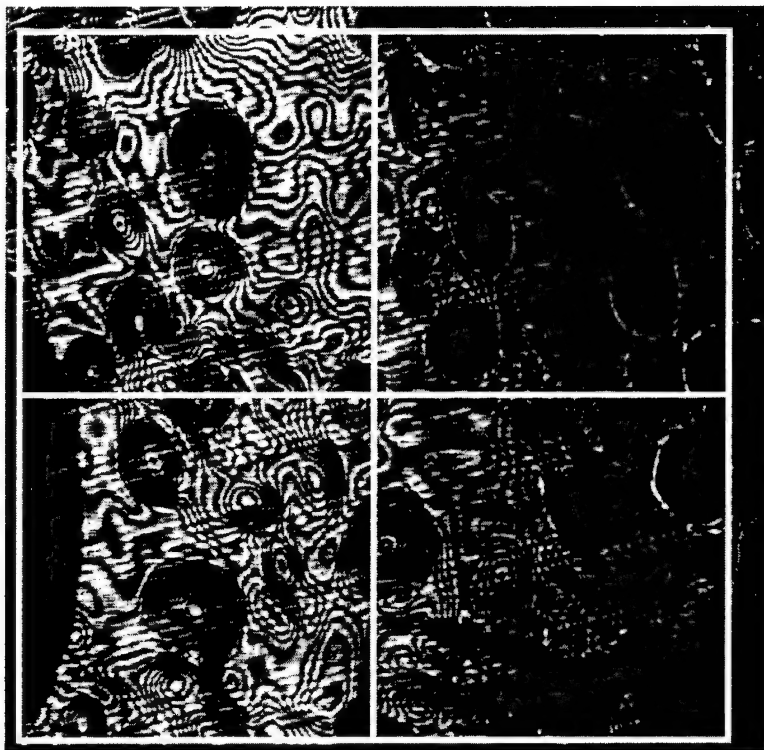Figure 5.24   Four Square PVDF Membrane, 650 V (Upper Left Quadrant)

Figure 5.25   Four Square PVDF Membrane, -650 V (Upper Left Quadrant)

VI. Conclusions and Recommendations

6.1 Conclusions

The objective of this research was to design and construct a system that will categorize surface properties of optical quality membrane material and be able to interpret membrane mirror deformation. The system constructed exceeds this objective by not only interpreting membrane deformation, but also providing indications of the degree of movement and the resultant deformation shape as indicated by aberration modes, and is able to provide membrane deformation data for mirrors up to 12 inches in diameter. This system was calibrated using a mirror with known surface properties, and the system was validated with the duplication of results even after rearranging system components.

Membrane mirror test tooling, including a membrane stretching ring and eight membrane mounting rings were designed and built, providing AFIT the ability to assemble membrane mirrors well into the future. Initial large aperture (six inch diameter) membranes were constructed, with varying degrees of controllability. These membranes exhibited minimal edge effects due to imparting pre-strain to the membrane material and optically polishing mounting ring surfaces which became the membrane boundary condition. PVDF etching techniques were developed along with experimental bonding methods of PVDF to membrane film and wire bonding to PVDF.

The optical system was able to resolve both membrane mirror image and membrane mirror deformation. Data was generated which tracks membrane mirror motion from planar along with comparison data to a flat reference surface. Maximum mirror motion was $32~\mu$, somewhat smaller than the 100μm recorded by Salama (37) at different inflation pressures. This thesis contains this data along with a theoretical tutorial of wavefront evolution through an optical system and consolidates other research involving both membrane mirror and inflatable systems.

6.2 Lessons Learned

Bonding the PVDF layer to the membrane proved to be the largest single obstacle to obtaining perfect membrane motion analysis. The effects of this bond produced minor surface discontinuities resembling "bubbling" which were easily observed in Figure 5.22. Non-contact deformation analysis, such as the optical interferometry and Shack-Hartmann wavefront sensing used in this research, depends upon continuous shape surfaces. These surfaces can either be planar, such as plate glass or a flat mirror, or have some radius of curvature, such as a spherical mirror or a lens. This enables even fringe spacing that can be adjusted with tip/tilt. When small discontinuities increase in number across the surface shape, fringes correspondingly become more dense, representing increased phase (and thus surface) information. Even when fringe spacing is maximized by removing all tip/tilt, fringes are spaced too tightly to be resolved by traditional interferometric analysis programs. Shack-Hartmann analysis encounters similar problems on these surfaces, as the bubbling detracts from even surface lighting, which is required to maximize system subapertures and thus full analysis. The adhesive spray bonding method provided the best PVDF to membrane bond, but the bond was not uniform over the two materials and imparted membrane surface deformation. This bond needs to either be improved or eliminated altogether. Another significant bonding lesson learned involved the holding ring to membrane bond. Direct bond to the stretched membrane material retains the prestretch which is critical to obtaining a membrane image. The mounting ring should only be bonded to prestretched material.

Wire bonding improved during the course of this research, but it remains an area of needed improvement. Experimentation with direct bonds using materials which deform the PVDF surface, such as soldering or direct epoxy proved unsuccessful. Various tape methods were tried, from thin copper tape soldered to the wire to direct application of the wire to the surface were successful, with the degree of success corresponding to the thinness of the material and least surface area. Simple scotch brand tape provided the least observable bond.

Optical lessons learned involved spatial filtering and lens matching. The spatial filter provides the key element to beam expansion. However, to ensure an even distribution of

the beam, which is essential for distributed intensity required by Wavescope, the primary laser mode should be captured in the system and all other modes (and noise) filtered by the pinhole. Additionally, acromatic lens position should match the desired wavefront. If a collimated beam is the desired output of the lens, the planar side of the acromat is the side that faces the input. This was contrary to initial intuition where a collimated output was thought to occur by placing the planar side of the acromat at the output.

Photoetching produced many lessons learned, for all involved, as it was a process designed for rigid material (such as a circuit board) and not a thin flexible membrane. Two of the most important deserve mention here. Removal of the film from the photoresist is a delayed process as the exposure of the photoresist to air cures it on the film. To achieve the required even coat, the film must be removed at a continual slow rate. Uneven coating of this material will result in an uneven pattern etch and resultant bad electrode, and thus control area(s). After exposure to the desired control pattern, the film must be put in an 65 degC oven to remove residual moisture before pattern etching, or the moisture will lift areas of the photoresist which will destroy the desired etch pattern.

6.3   Recommendations for Future Research

1. Refine/eliminate the PVDF to membrane bonding layer. This would improve surface analysis efforts and provide more accurate deformation information over the entire aperture

2. Refine wire bonding to the PVDF surface. It was found that bonding a wire to the aperture imparts significant deviation to the membrane. Therefore, a method needs to be developed which applies voltage to the target areas while keeping wire bonds outside the aperture. A candidate solution may be photoetching electrical pathways to each pattern from a wire contact area outside the aperture, similar to electrical routing on a circuit board.

3. Utilize bi-directional PVDF as the control film and improve control patterns. This research has proven the ability to control a membrane mirror with a PVDF film, along with zonal control after etching patterns into a PVDF electrode. However, the

6-3

directional nature of the PVDF causes aberrations in the wavefront as the material expands/contracts in only one direction. This can be improved by using bi-directional PVDF. Additionally, research into control pattern optimization and design is needed before full membrane control can be achieved. An interlaced series of hexagonal elements may be a candidate solution.

4. Investigate membrane prediction computer algorithms, such as those mentioned in Section 2.3.2, for application to the PVDF deformable membrane. Modifications to these programs will be required for PVDF and not pressure membrane actuation, but may provide a model to determine PVDF diameter on the membrane for optimum acutation, optimum PVDF shapes, and other parameters.

Appendix A. Image Location Calculations

Refract L4	Translate L3 to L4	Focus L3	Translate BS to L3	Focus BS	Translate BS	Focus BS	Translate L2 to BS	Focus L2	Translate Parabola to L2	Focus Parabola

$$M := \begin{bmatrix} 1 & -\dfrac{1}{7.5} \\ 0 & 1 \end{bmatrix} \cdot \begin{bmatrix} 1 & 0 \\ 19.3 & 1 \end{bmatrix} \cdot \begin{bmatrix} 1 & -\dfrac{1}{12} \\ 0 & 1 \end{bmatrix} \cdot \begin{bmatrix} 1 & 0 \\ 8.5 & 1 \end{bmatrix} \begin{bmatrix} 1 & 0 \\ 0 & 1 \end{bmatrix} \cdot \begin{bmatrix} 1 & 0 \\ \dfrac{5.08}{1.518} & 1 \end{bmatrix} \cdot \begin{bmatrix} 1 & 0 \\ 0 & 1 \end{bmatrix} \begin{bmatrix} 1 & 0 \\ 14.6 & 1 \end{bmatrix} \cdot \begin{bmatrix} 1 & -\dfrac{1}{10} \\ 0 & 1 \end{bmatrix} \cdot \begin{bmatrix} 1 & 0 \\ 199 & 1 \end{bmatrix} \cdot \begin{bmatrix} 1 & -\dfrac{1}{190.5} \\ 0 & 1 \end{bmatrix}$$

$$M = \begin{bmatrix} 30.405 & 1.384 \cdot 10^{-3} \\ -181.76 & 0.025 \end{bmatrix}$$

$f := \dfrac{-1}{M_{0,1}}$ $\qquad f = -722.4$ $\qquad$ System focal length (cm)

$H1 := \dfrac{1 - M_{0,0}}{-M_{0,1}}$ $\qquad H1 = 2.124 \cdot 10^{4}$ $\qquad$ 1st principle plane lies
H1 cm to right of vertex
of m1

$H2 := \dfrac{M_{1,1} - 1}{-M_{0,1}}$ $\qquad H2 = 704.618$ $\qquad$ 2nd principle plane lies
H2 cm to right of vertex
of L3

$S := H1 - 259$ $\qquad S = 2.098 \cdot 10^{4}$ $\qquad$ Object lies S cm to the left of principle plane H1

$S1 := \dfrac{1}{\left(\dfrac{1}{f} - \dfrac{1}{S} \right)}$ $\qquad S1 = -698.357$ $\qquad$ Image lies S1 cm to the right of the 2nd principle plane H2

$Image := H2 + S1$ $\qquad Image = 6.262$ $\qquad$ Image lies Pi cm to right of the last lens in the train (L3)

Figure A.1   Image Location Calculations, Standard System

Refract L4	Translate L3 to L4	Focus L3	Translate BS to L3	Focus BS	Translate BS	Focus BS	Translate L2 to BS	Focus L2	Translate Parabola to L2	Focus Parabola

$$M := \begin{bmatrix} 1 & -\dfrac{1}{12} \\ 0 & 1 \end{bmatrix} \cdot \begin{bmatrix} 1 & 0 \\ 18.24 & 1 \end{bmatrix} \cdot \begin{bmatrix} 1 & -\dfrac{1}{7.5} \\ 0 & 1 \end{bmatrix} \cdot \begin{bmatrix} 1 & 0 \\ 3.79 & 1 \end{bmatrix} \cdot \begin{bmatrix} 1 & 0 \\ 0 & 1 \end{bmatrix} \cdot \begin{bmatrix} 1 & 0 \\ \dfrac{5.08}{1.518} & 1 \end{bmatrix} \cdot \begin{bmatrix} 1 & 0 \\ 0 & 1 \end{bmatrix} \cdot \begin{bmatrix} 1 & 0 \\ 10 & 1 \end{bmatrix} \cdot \begin{bmatrix} 1 & -\dfrac{1}{10} \\ 0 & 1 \end{bmatrix} \cdot \begin{bmatrix} 1 & 0 \\ 199 & 1 \end{bmatrix} \cdot \begin{bmatrix} 1 & -\dfrac{1}{190.5} \\ 0 & 1 \end{bmatrix}$$

$$M = \begin{bmatrix} 11.576 & 1.223 \cdot 10^{-3} \\ -165.908 & 0.069 \end{bmatrix}$$

$f := \dfrac{-1}{M_{0,1}}$ $\qquad$ $f = -817.643$ $\qquad$ System focal length (cm)

$H1 := \dfrac{1 - M_{0,0}}{-M_{0,1}}$ $\qquad$ $H1 = 8.648 \cdot 10^3$ $\qquad$ 1st principle plane lies H1 cm to right of vertex of m1

$H2 := \dfrac{M_{1,1} - 1}{-M_{0,1}}$ $\qquad$ $H2 = 761.344$ $\qquad$ 2nd principle plane lies H2 cm to right of vertex of L3

$S := H1 - 259$ $\qquad$ $S = 8.389 \cdot 10^3$ $\qquad$ Object lies S cm to the left of principle plane H1

$S1 := \dfrac{1}{\left(\dfrac{1}{f} - \dfrac{1}{S}\right)}$ $\qquad$ $S1 = -745.026$ $\qquad$ Image lies S1 cm to the right of the 2nd principle plane H2

$Image := H2 + S1$ $\qquad$ $Image = 16.319$ $\qquad$ Image lies Pi cm to right of the last lens in the train (L3)

Figure A.2 $\quad$ Image Location Calculations, Magnified System
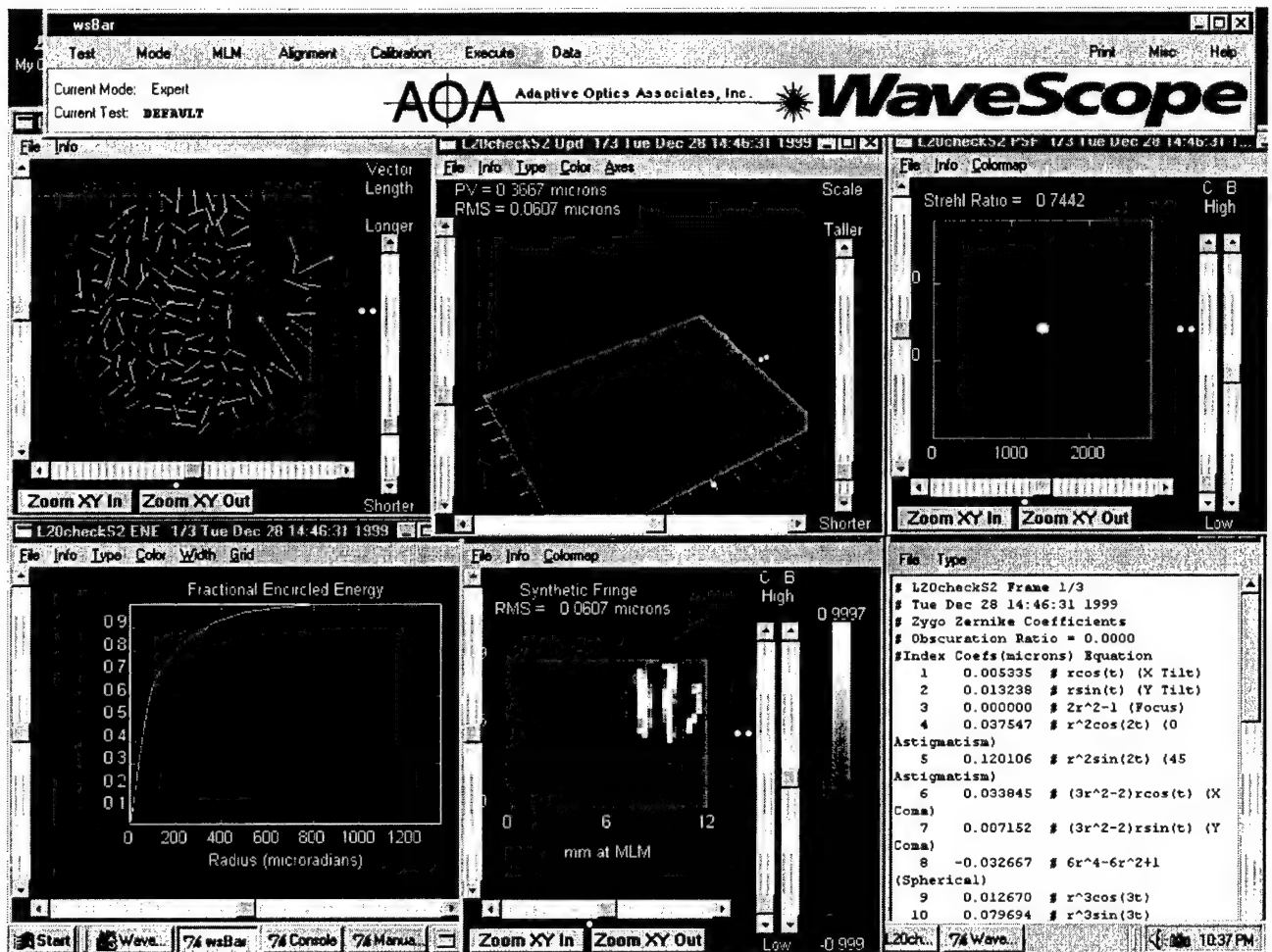
Appendix B. Wavescope Output Data
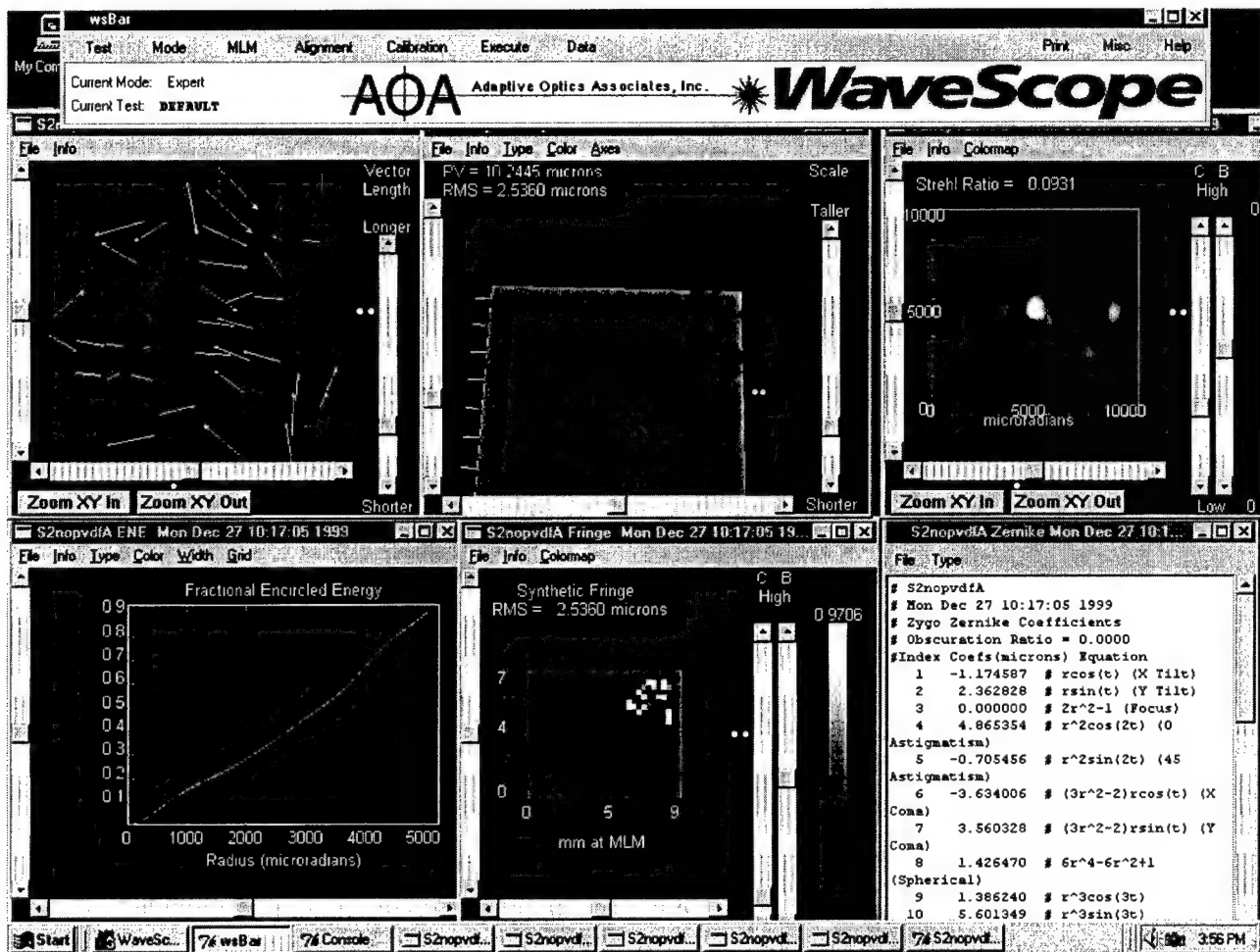
Figure B.1   Wavescope Calibration Data

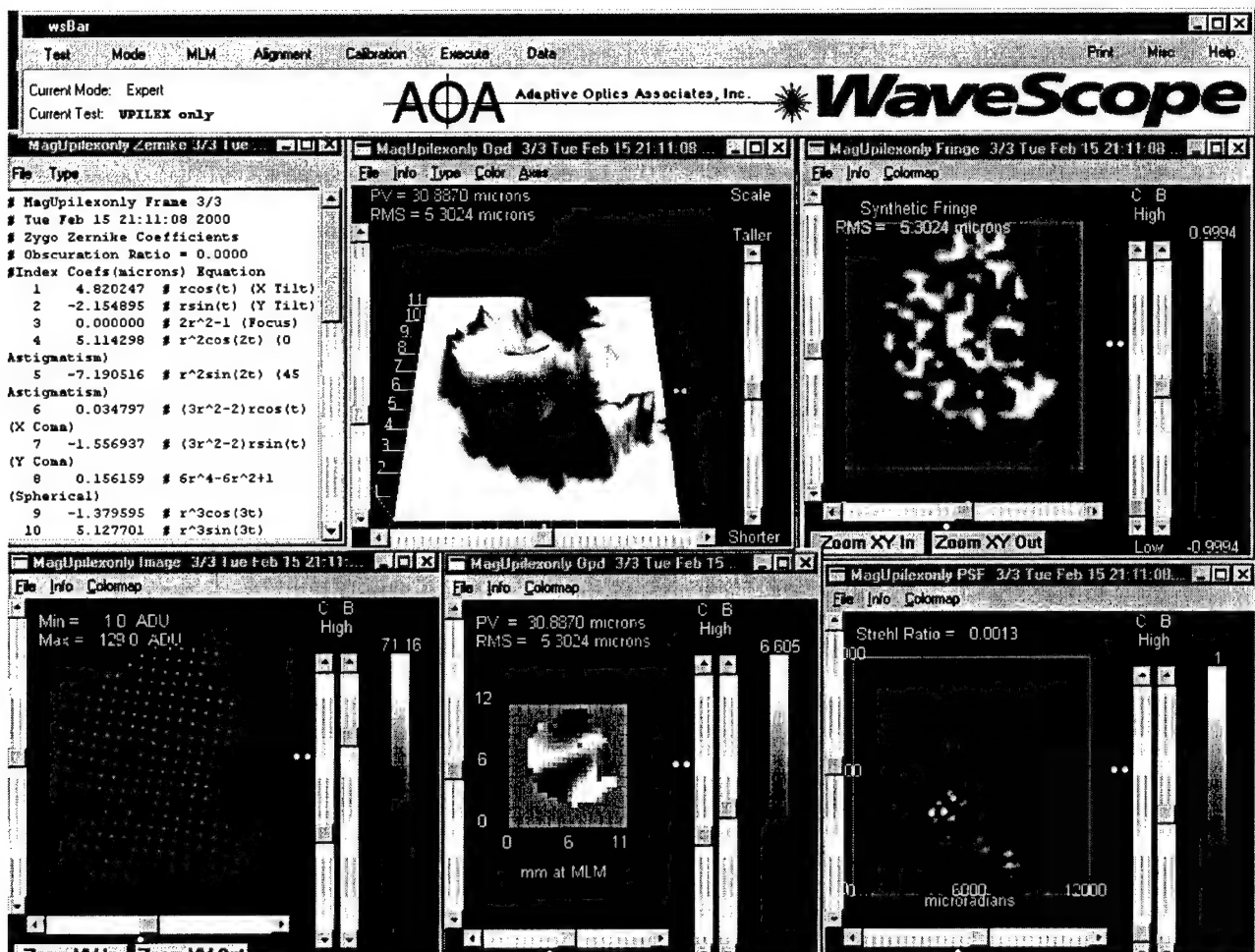Figure B.2   Upilex-only Wavescope Output

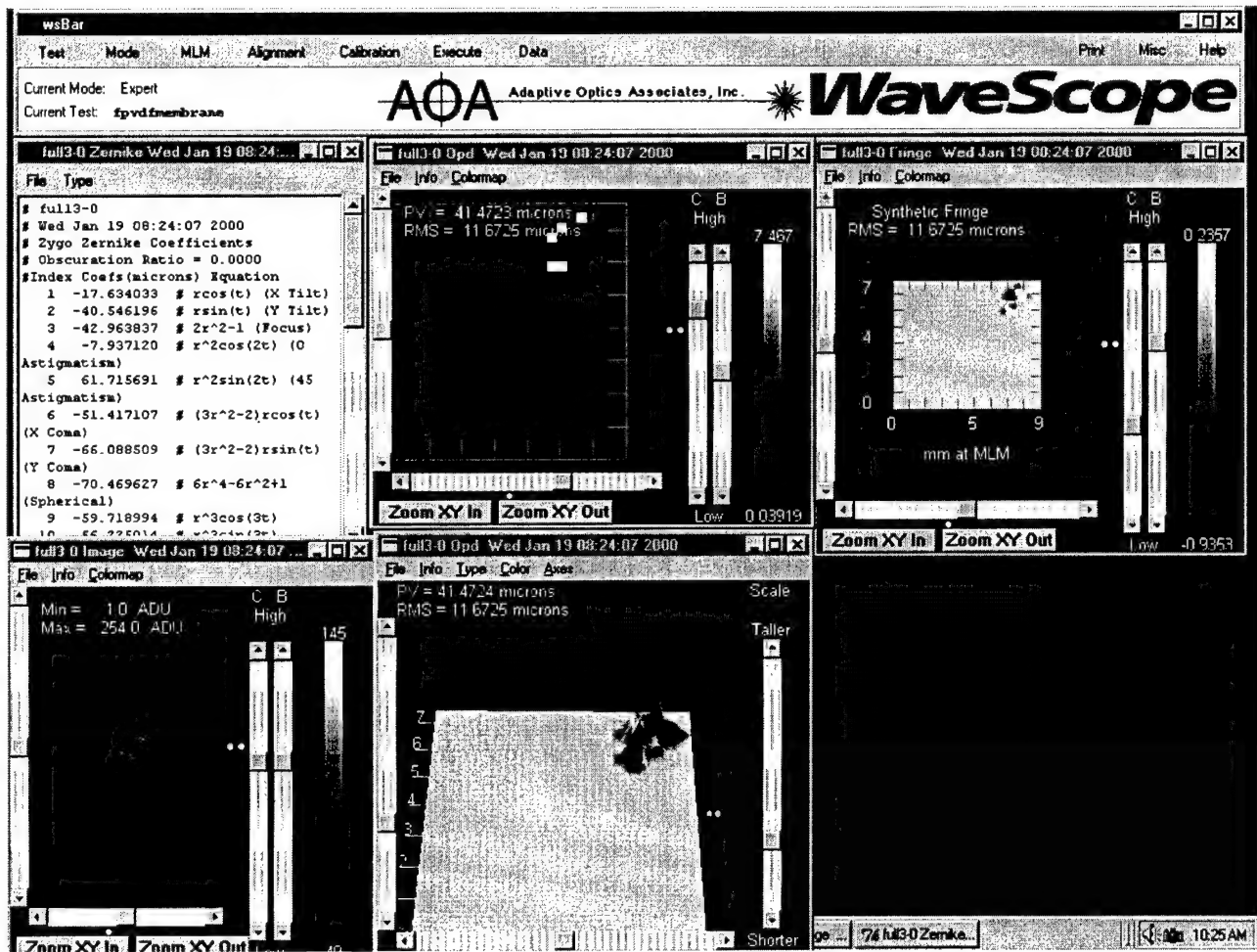Figure B.3 Upilex-only Membrane, Magnified Wavescope pupil

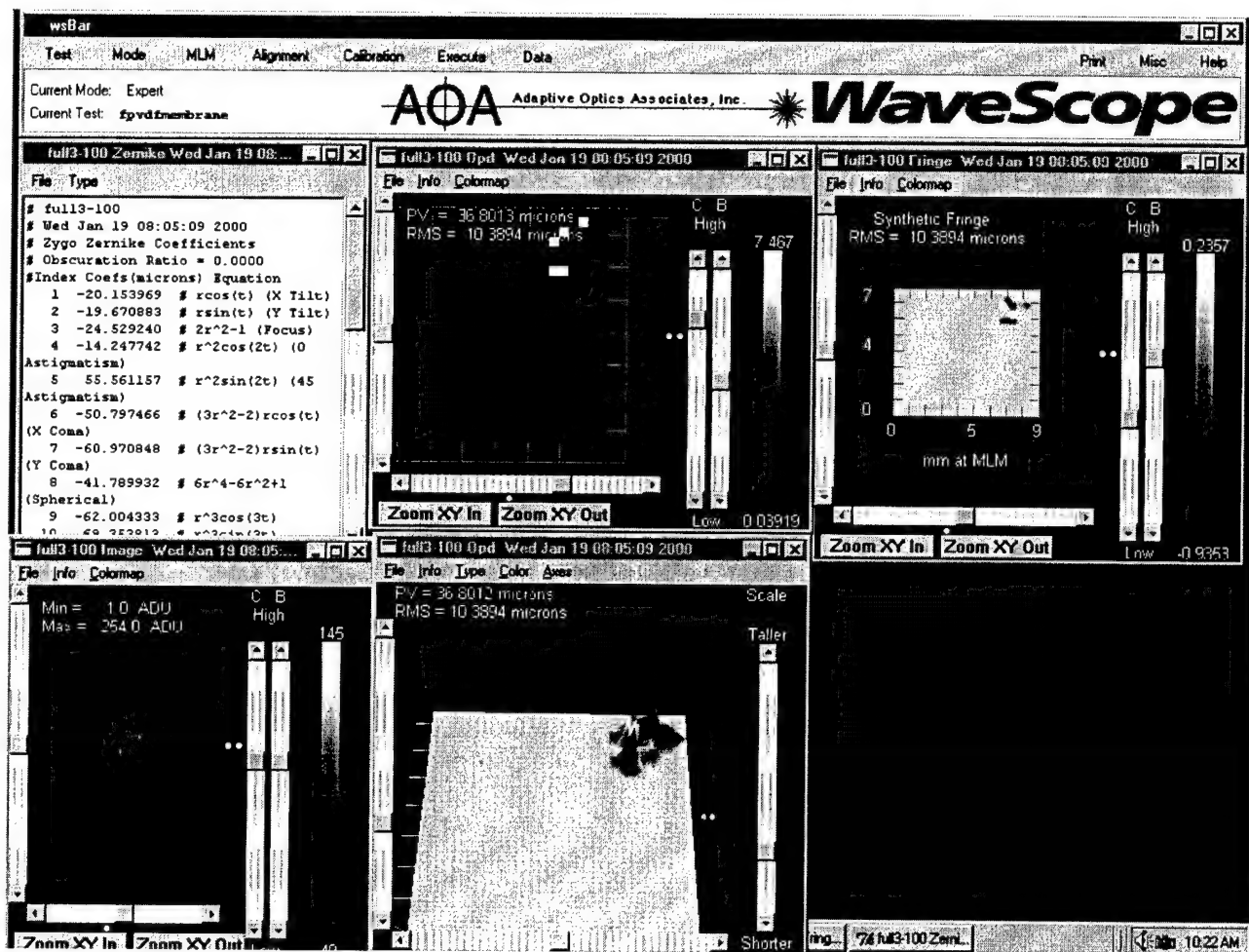Figure B.4   Wavescope Data: Full PVDF on Membrane, 0 V

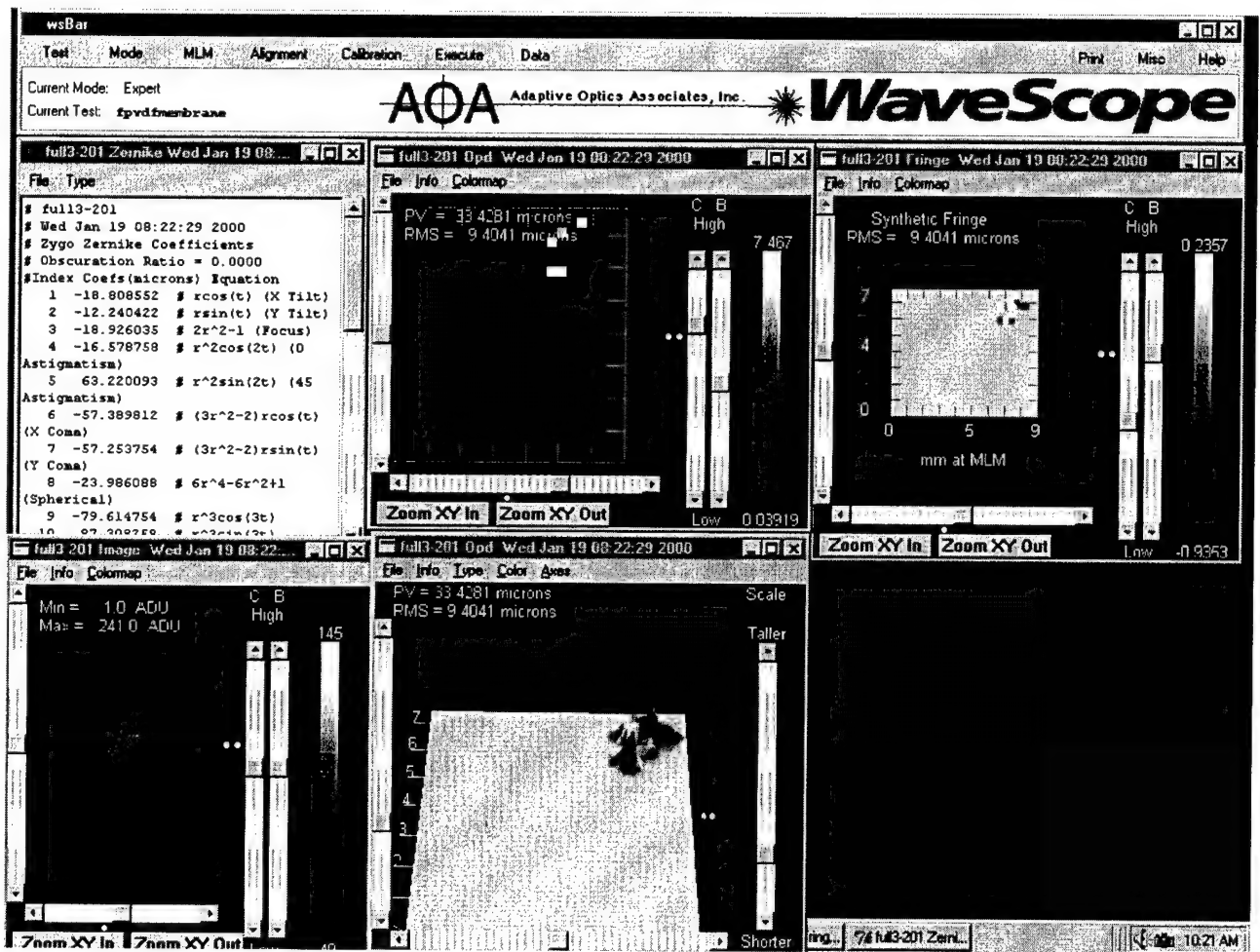Figure B.5   Wavescope Data: Full PVDF on Membrane, 100 V

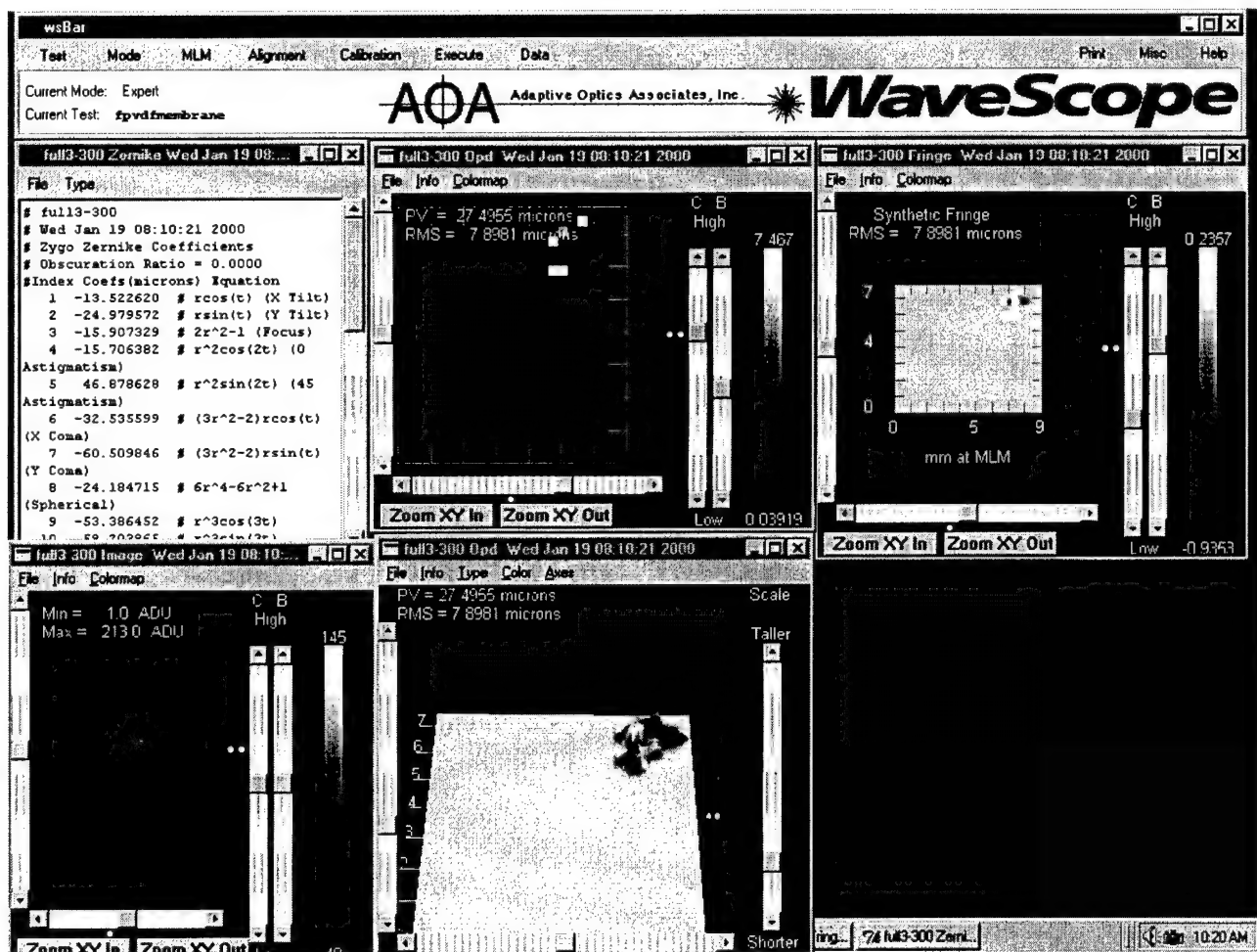Figure B.6   Wavescope Data: Full PVDF on Membrane, 200 V

Figure B.7   Wavescope Data: Full PVDF on Membrane, 300 V
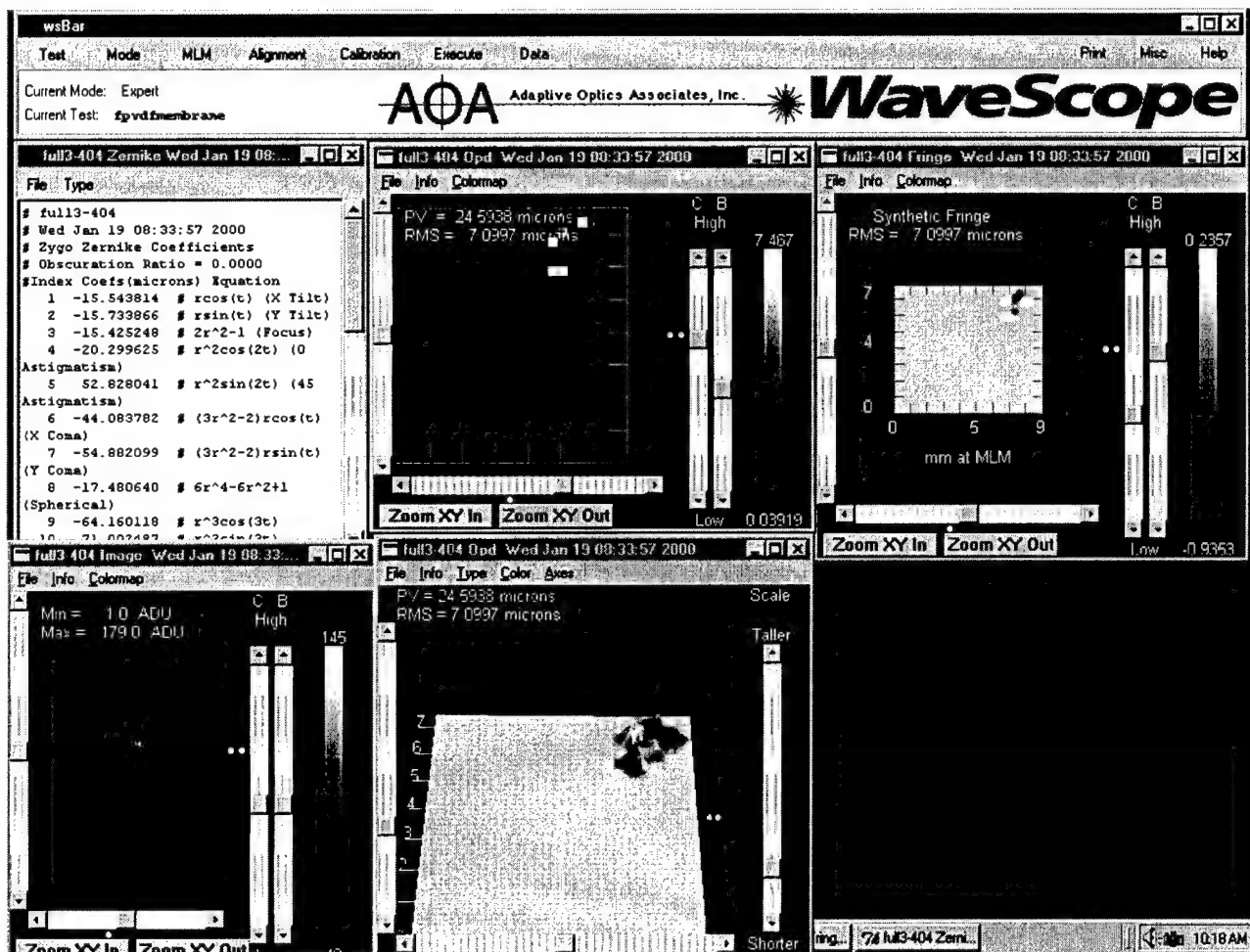
Figure B.8   Wavescope Data: Full PVDF on Membrane, 400 V
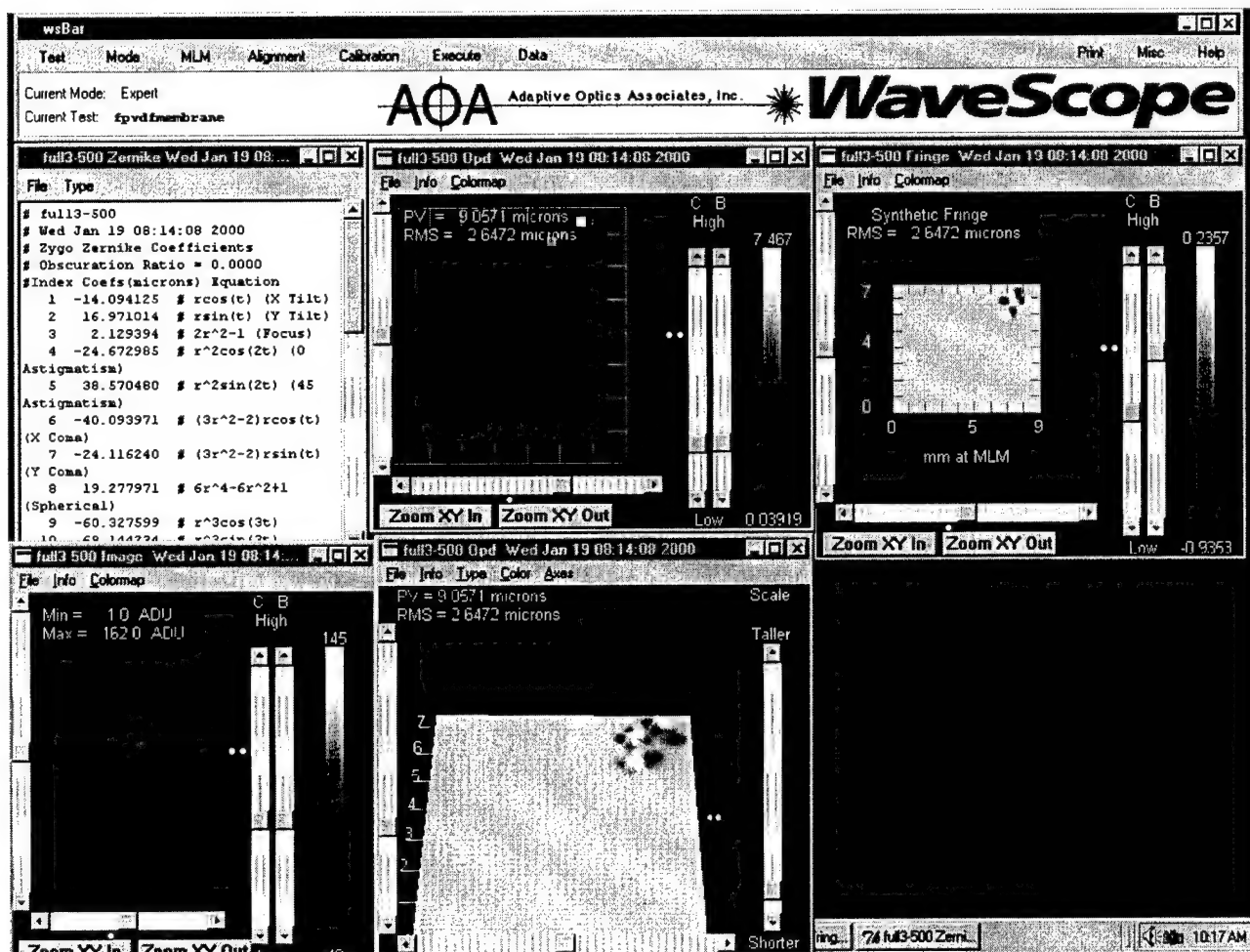
Figure B.9   Wavescope Data: Full PVDF on Membrane, 500 V

Appendix C. Interferometric Data, Zonal Membrane Deformation
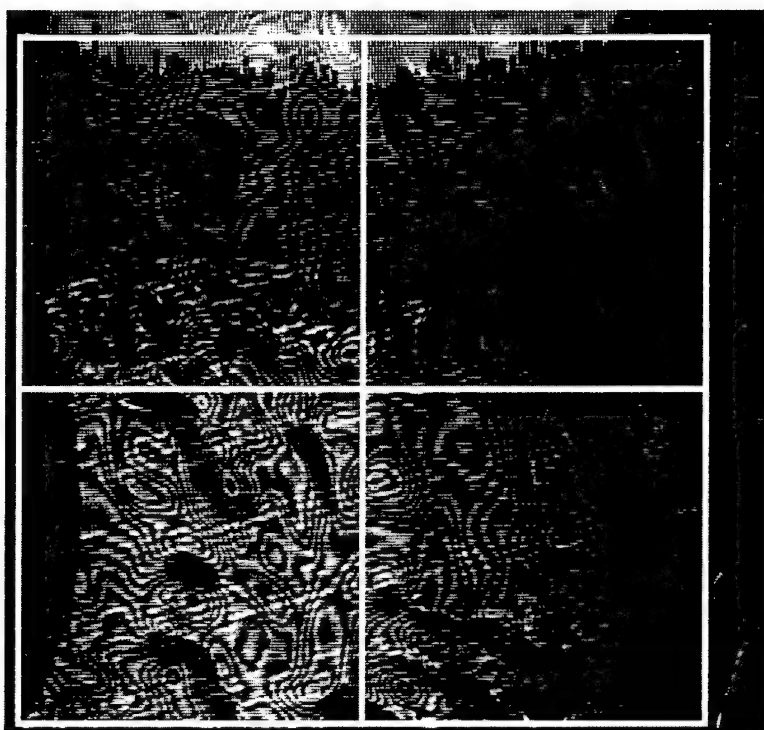
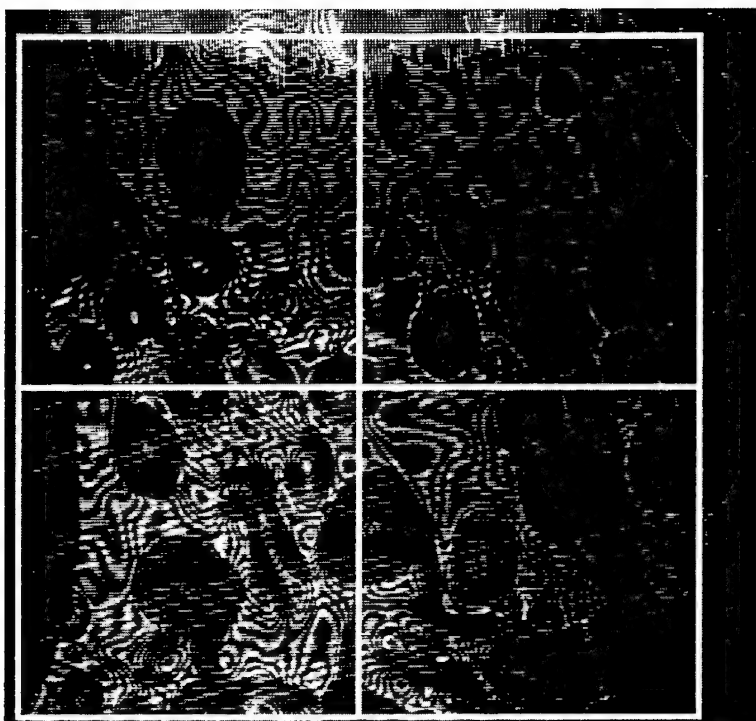Figure C.1   Lower Left Quadrant, 650V

Figure C.2   Lower Left Quadrant, -650V
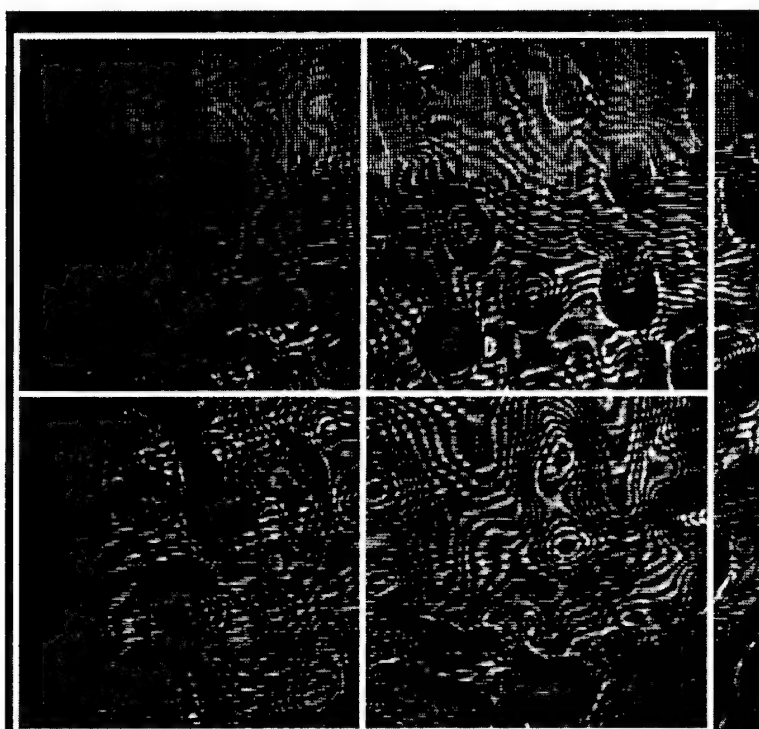
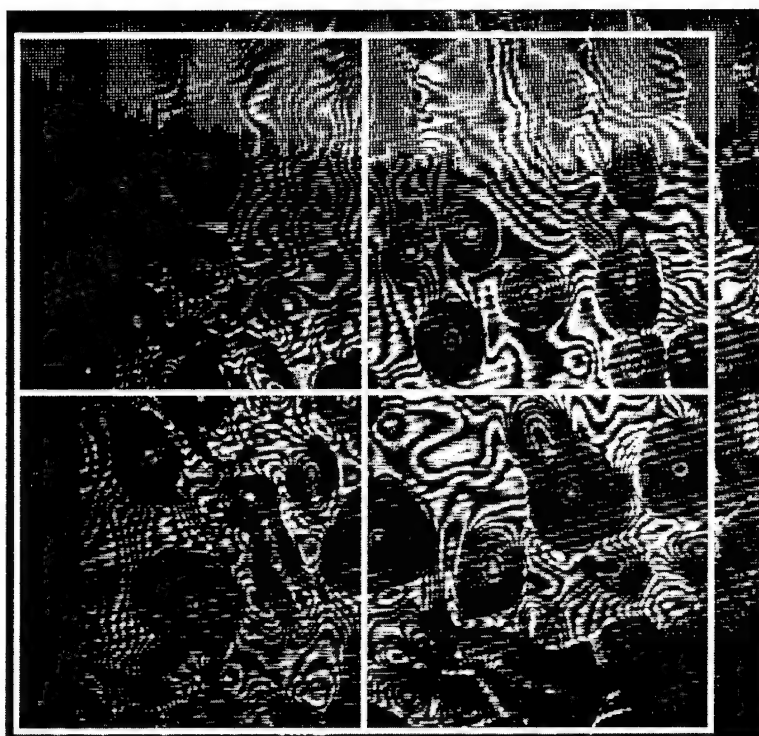Figure C.3   Lower Right Quadrant, 650V
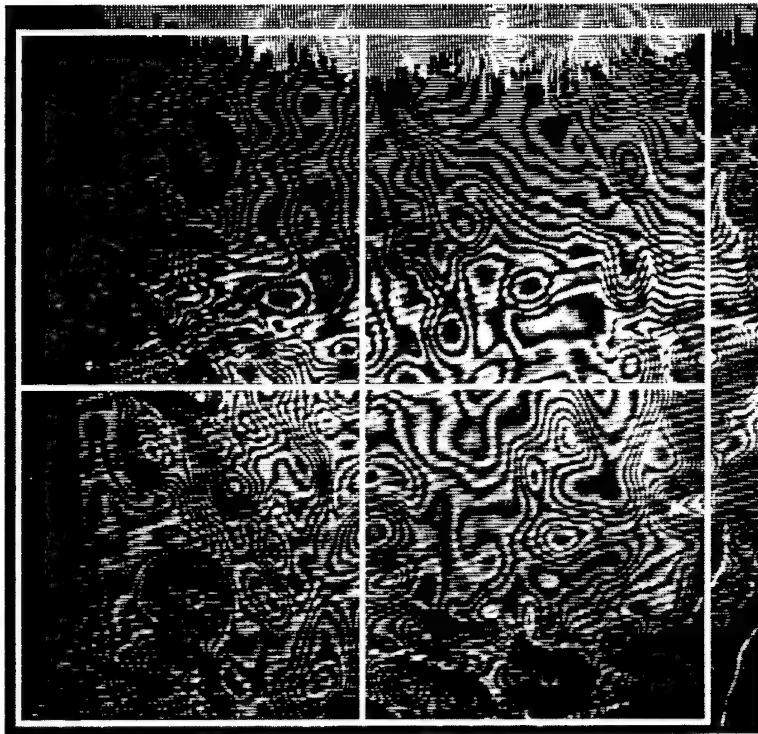
Figure C.4   Lower Right Quadrant, -650V

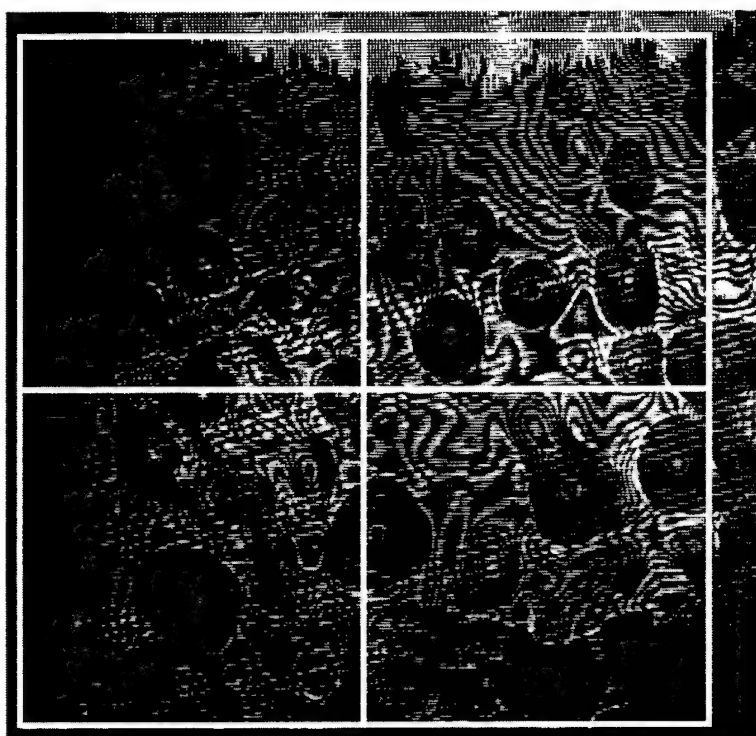Figure C.5   Upper Right Quadrant, 650V

Figure C.6   Upper Right Quadrant, -650V

Bibliography

1. *APEX Features and Specifications*. On-Line Product Information. Lambda Research Corporation, www.lambdares.com/PRODUCTS/apex/apex6.html, 2000.

2. Bishop, J.A. "Shape Correction of Initially Flat Inflated Membranes by a Genetic Algorithm," *AIAA/ASME/ASCE/AHS/ASC Structures, Structural Dynamics, and Materials Conference, Long Beach, CA*, (AIAA 98-1984) (1998).

3. Carreras, Richard A. and others, "Tunable Membrane Mirrors Used With Real Time Holography." Research Briefing, 1999.

4. Cassapakis, Constantine G. and others. "Inflatable Space Antennas - A Brief Overview." *1998 IEEE Aerospace Conference Proceedings*. 453–9. New York: IEEE Press, 1998.

5. Cassapakis, Costa and Mitch Thomas. "Inflatable Structures Technology Development Overview," *AIAA 1995 Space Programs and Technologies Conference, Huntsville, AL*, (AIAA 95-3738) (1995).

6. Commercial, Kodak and Government Systems, "Building The Back Up Hubble Space Telescope Mirror." http://www.kodak.ch/US/en/government/ias/heritage/hubble.shtml.

7. Department of the Air Force. *New World Vistas: Air and Space Power for the 21st Century*. Technical Report. Washington: USAF Scientific Advisory Board, 1995.

8. Dornheim, M.A. and J.C. Anselmo. "Complex Antenna is Star of Mission 77," *Aviation Week and Space Technology*, 58–9 (May 27,1996).

9. Dunemann, Dennis and Dan Marker. Personal interview, AFRL/DE, 18 August 1999.

10. *Frame Grabber Product Specification Sheets*. On-Line Product Information. Imagenation Corporation, www.imagenation.com/spec.htm, 1999.

11. Freeland, R.E. and others. *Large Inflatable Deployable Antenna Flight Experiment Results*. Technical Report, 48th International Astronautical Federation Congress: Turin, Italy IAF-97-1.3.01, International Astronautical Federation, 1997.

12. Freeland, R.E. and others. *Inflatable Deployable Space Structures Technology Summary*. Technical Report, 49th International Astronautical Federation Congress: Melbourne, Australia IAF-98-1.5.01, International Astronautical Federation, 1998.

13. Gasvik, Kjell J. *Optical Metrology* (Second Edition). John Wiley & Sons, 1995.

14. Geary, Joseph M. *Introduction to Wavefront Sensors*. Bellingham, Washington: SPIE-The International Society for Optical Engineering, 1995.

15. Glover, Daniel R., "NASA Experimental Communications Satellites." http://sulu.lerc.nasa.gov/dglover/echo.html, 1998.

16. Goodman, Joseph W. *Introduction to Fourier Optics* (Second edition Edition). McGraw-Hill Electrical and Computer Engineering Series, McGraw Hill, 1996.

17. Gruneisen, Mark T. and others. "Correction of Large Dynamic Aberrations by Real-Time Holography using Electro-Optical Devices and Nonlinear Optical Media," *Proceedings of SPIE-The International Society for Optical Engineering, High-Resolution Wavefront Control: Methods, Devices, and Applications*, *3760*:207–212 (July 1999).

18. Gruneisen, M.T. and others. "Holographic Compensation of Severe Dynamic Aberrations in Membrane-Mirror Based Telescope Systems," *Proceedings of SPIE-The International Society for Optical Engineering, High-Resolution Wavefront Control: Methods, Devices, and Applications*, *3760*:142–151 (July 1999).

19. Guthals, Dennis and others. "Real-Time Holographic Compensation of Large Optics for Space Deployment," *Proceedings of SPIE-The International Society for Optical Engineering, High-Resolution Wavefront Control: Methods, Devices, and Applications*, *3760*:162–171 (July 1999).

20. Hariharan, P. *Optical Interferometry*. New South Wales, Australia: Academic Press Australia, 1985.

21. Hecht, Eugene. *Optics* (Third Edition). Reading, Massachusetts: Addison Wesley Longman, Inc., 1998.

22. Janning, John L. Personal interview, JLJ Inc., 21 December 1999.

23. J.R., Rotgé and others. "Large Opticlly Flat Membrane Mirrors," *Proceedings of SPIE-The International Society for Optical Engineering, High-Resolution Wavefront Control: Methods, Devices, and Applications*, *3760*:207–212 (July 1999).

24. Kato, Sumio and others. "Research on a Reflector Structure Composed of Inflatable Elements," *Proceedings of the Seventeenth International Symposium on Space Technology and Science* (1990).

25. Klein, Miles V. and Thomas E. Furtak. *Optics* (Second Edition). New York: John Wiley & Sons, 1986.

26. Kokorowski, S.A. "Analysis of Adaptive Optical Elements Made From Piezoelectric Bimorphs," *Journal of the Optical Society of America*, *69*(1) (1979).

27. Lou, M.C. and others. "Development of an Inflatable Space Synthetic Aperture Radar," *AIAA/ASME/ASCE/AHS/ASC Structures, Structural Dynamics, and Materials Conference, Long Beach, CA*, (AIAA 98-2103) (1998).

28. Malacara, Daniel. *Optical Shop Testing*. John Wiley & Sons, 1978.

29. Marker, D.K. and others. "Minimum Strain Requirements of Optical Membranes," *Proceedings of SPIE-The International Society for Optical Engineering, High-Resolution Wavefront Control: Methods, Devices, and Applications*, *3760*:224–231 (July 1999).

30. Marker, D.K. and others. "Summary: Optical Membrane Workshop," *Proceedings of SPIE-The International Society for Optical Engineering, High-Resolution Wavefront Control: Methods, Devices, and Applications*, *3760*:192–194 (July 1999).

31. Noor, Ahmed K. and Samuel L. Venneri, editors. *State of the Art and Technology Needs for Large Space Structures*, chapter by Mikulas, Martin M. Jr., and Thompson, Mark, 173–238. Flight-Vehicle Materials, Structures, and Dynamics Series, The American Society of Mechanical Engineers, 1994.

32. *Optics and Mechanics*. Product Catalog. Newport Corporation, Irvine CA, 1999/2000.

33. Palisoc, Arthur L. and Uli Huang. "Design Tool for Inflatable Space Structures," *AIAA/ASME/ASCE/AHS/ASC Structures, Structural Dynamics, and Materials Conference, Kissimmee, FL*, (AIAA 97-1378) (1997).

34. *Piezo Film Sensors Technical Manual*. Product Manual. Measurement Specialties, Inc., Valley Forge, PA, 1998.

35. Rappaport, Ed, "National Hurricane Center Preliminary Report: Hurricane Andrew, 16-28 August 1992." http://www.nhc.noaa.gov/1992andrew.html, December 1993.

36. Ruze, John. "Antenna Tolerance Theory–a Review," *Symposium of the IEEE Group on Antennae and Propagation*, *54*(4) (1965).

37. Salama, M. and others. "On-Orbit Shape Correction of Inflatable Structures," *1994 AIAA/ASME Adaptive Structures Forum*, (AIAA-94-1771-CP) (1994).

38. Sato, Takuso and others. "Adaptive PVDF Piezoelectric Deformable Mirror System," *Applied Optics*, *19*(9) (1980).

39. Satter, Celeste M. and Robert E. Freeland. "Inflatable Structures Technology Applications and Requirements," *AIAA 1995 Space Programs and Technologies Conference, Huntsville, AL*, (AIAA 95-3737) (1995).

40. Shannon, R.R. and J.C. Wyant. *Applied Optics and Optical Engineering*, *XI*. Academic Press Limited, 1992.

41. Trop, Bill. Personal interview, AFIT/ENG, 13 December 1999.

42. Tyson, Robert K. *Principles of Adaptive Optics*. San Diego, California: Academic Press, Inc., 1991.

43. *UBE Specialty Materials On Line Catalogs: Upilex-S*. On-Line Product Information. UBE Corporation, http://www.orbital-e.co.jp/ube-labo/upilex-s.html, 2000.

44. Vasil'ev, M.V. and others. "Imaging Bypass System with Correction for Primary Mirror Distortions," *Proceedings of SPIE-The International Society for Optical Engineering, High-Resolution Wavefront Control: Methods, Devices, and Applications*, *3760*:153–161 (July 1999).

45. Veal, Gordon and Robert Freeland. "IN-STEP Inflatable Antenna Description," *AIAA 1995 Space Programs and Technologies Conference, Huntsville, AL*, (AIAA 95-3739) (1995).

46. *Wavescope Product Brochure*. Product Manual. Adaptive Optics Associates, Cambridge MA, 1999.

47. *Wavescope Users Manual*. Product Manual. Adaptive Optics Associates, Cambridge MA, 1999.

48. Wilkes, J.M. and others. "Concave Membrane Mirrors from Aspheric to Near-Parabolic," *Proceedings of SPIE-The International Society for Optical Engineering, High-Resolution Wavefront Control: Methods, Devices, and Applications, 3760*:213–223 (July 1999).

Vita

Captain John W. Wagner was born on 6 January 1969 in Battle Creek, Michigan. He received an appointment to the United States Air Force Academy upon graduation from St. Philip High School, where he majored in Astronautical Engineering and conducted focused research in hybrid rocket propulsion. He was presented with his Bachelor of Science in Astronautical Engineering by President George Bush in May, 1991.

His first Air Force assignment was Propulsion Systems Engineer for the Titan IV space launch vehicle program at Cape Canaveral AFS, Florida, providing technical oversight liquid rocket engine and propellant transfer system procedures, and was responsible for system launch go/no-go decisions. He then transitioned to Titan Payload Fairing Engineer, responsible for Titan payload integration, payload fairings, airborne mechanical systems, contamination prevention, and vehicle transporter systems. In 1994, he was selected for Chief, Launch Operations Training at the 45th Operations Support Squadron, where he directed development and implementation of wing training programs for Atlas II, Delta II, and Titan IV launch vehicles.

In 1995 he was selected to crossflow into space operations and completed Undergraduate Space and Missile Training at Vandenberg AFB as a Distinguished Graduate. Upon completion of Crew Commander training, he served as a Flight Commander at the 3rd Space Communications Squadron, Kapaun, Germany from 1996 to September 1997, then Commander, Operations Support Flight until August 1998. While serving in these capacities, he became both instructor and evaluator, and earned a Masters Degree in Business Administration from the University of Maryland-Europe.

In August 1998, he began the Graduate Astronautical Engineering program at the Air Force Institute of Technology. Upon graduation he will be reassigned to the Engineering and Analysis Directorate at the Space Warfare Center, Schriever AFB, CO.

He is married to the former Jennifer Schmidt of Piqua, OH, and they have two boys, Jeffrey and Jacob.

Permanent address: 3866 Chalet Circle North
Beavercreek, Ohio 45431

REPORT DOCUMENTATION PAGE

Form Approved
OMB No. 0704-0188

1. AGENCY USE ONLY *(Leave blank)*	2. REPORT DATE	3. REPORT TYPE AND DATES COVERED
	March 2000	Thesis, Master of Science

4. TITLE AND SUBTITLE

OPTICAL METROLOGY OF ADAPTIVE MEMBRANE MIRRORS

5. FUNDING NUMBERS

99-159

6. AUTHOR(S)

John W. Wagner, Captain, USAF

7. PERFORMING ORGANIZATION NAME(S) AND ADDRESS(ES)

Air Force Institute of Technology
Graduate School of Engineering and Management (AFIT/EN)
2950 P Street, Building 640
WPAFB OH 45433-7765

8. PERFORMING ORGANIZATION REPORT NUMBER

AFIT/GA/ENY/00M-05

9. SPONSORING/MONITORING AGENCY NAME(S) AND ADDRESS(ES)

Air Force Office of Scientific Research (Maj Brian Sanders)
801 North Randolph Street, Room 732
Arlington VA 22203-1977

10. SPONSORING/MONITORING AGENCY REPORT NUMBER

11. SUPPLEMENTARY NOTES

Advisor: Capt Greg Agnes, ENY, DSN: 785-3636, ext. 4317, gregory.agnes@afit.af.mil

12a. DISTRIBUTION AVAILABILITY STATEMENT

APPROVED FOR PUBLIC RELEASE; DISTRIBUTION UNLIMITED

12b. DISTRIBUTION CODE

13. ABSTRACT *(Maximum 200 words)*

Current space-based imaging platforms are significantly constrained in both size and weight by the launch vehicle. Increased payload size and weight results in increased cost and a decrease in launch responsiveness. The USAF Scientific Advisory Board (SAB) identified "Large lightweight structures for optics and antennas" as a revolutionary primary technology to be developed for the Air Force of the 21st Century. A membrane primary mirror in a space-based imaging system has the ability to overcome current payload constraints and meet evolutionary needs of the future.

The objective of this research was to develop a system to categorize surface properties of optical quality membrane material with the ability to interpret membrane mirror deformation. Coincident with this objective was the design and construction of membrane mirrors and associated test tooling, the design and application of in-plane zonal control for membrane mirrors, and mirror deformation analysis. The system provides wavefront analysis with both optical interferometry and Shack-Hartmann wavefront sensing, with good correlation, and compares favorably to Zygo interferometer data.
Results from membrane static testing will be presented.

14. SUBJECT TERMS

adaptive optics, membrane mirrors, imaging, piezoelectric, deformation, zonal control, space based imaging, inflatable apertures

15. NUMBER OF PAGES

156

16. PRICE CODE

17. SECURITY CLASSIFICATION OF REPORT	18. SECURITY CLASSIFICATION OF THIS PAGE	19. SECURITY CLASSIFICATION OF ABSTRACT	20. LIMITATION OF ABSTRACT
UNCLASSIFIED	UNCLASSIFIED	UNCLASSIFIED	UL

Standard Form 298 (Rev. 2-89) (EG)
Prescribed by ANSI Std. 239.18
Designed using Perform Pro, WHS/DIOR, Oct 94

GENERAL INSTRUCTIONS FOR COMPLETING SF 298

The Report Documentation Page (RDP) is used in announcing and cataloging reports. It is important that this information be consistent with the rest of the report, particularly the cover and title page. Instructions for filling in each block of the form follow. It is important to *stay within the lines* to meet *optical scanning requirements.*

Block 1. Agency Use Only *(Leave blank)*.

Block 2. Report Date. Full publication date including day, month, and year, if available (e.g. 1 Jan 88). Must cite at least the year.

Block 3. Type of Report and Dates Covered. State whether report is interim, final, etc. If applicable, enter inclusive report dates (e.g. 10 Jun 87 - 30 Jun 88).

Block 4. Title and Subtitle. A title is taken from the part of the report that provides the most meaningful and complete information. When a report is prepared in more than one volume, repeat the primary title, add volume number, and include subtitle for the specific volume. On classified documents enter the title classification in parentheses.

Block 5. Funding Numbers. To include contract and grant numbers; may include program element number(s), project number(s), task number(s), and work unit number(s). Use the following labels:

C - Contract	**PR** - Project
G - Grant	**TA** - Task
PE - Program Element	**WU** - Work Unit Accession No.

Block 6. Author(s). Name(s) of person(s) responsible for writing the report, performing the research, or credited with the content of the report. If editor or compiler, this should follow the name(s).

Block 7. Performing Organization Name(s) and Address(es). Self-explanatory.

Block 8. Performing Organization Report Number. Enter the unique alphanumeric report number(s) assigned by the organization performing the report.

Block 9. Sponsoring/Monitoring Agency Name(s) and Address(es). Self-explanatory.

Block 10. Sponsoring/Monitoring Agency Report Number. *(If known)*

Block 11. Supplementary Notes. Enter information not included elsewhere such as: Prepared in cooperation with....; Trans. of....; To be published in.... When a report is revised, include a statement whether the new report supersedes or supplements the older report.

Block 12a. Distribution/Availability Statement. Denotes public availability or limitations. Cite any availability to the public. Enter additional limitations or special markings in all capitals (e.g. NOFORN, REL, ITAR).

DOD - See DoDD 5230.24, "Distribution Statements on Technical Documents."
DOE - See authorities.
NASA - See Handbook NHB 2200.2.
NTIS - Leave blank.

Block 12b. Distribution Code.

DOD - Leave blank.
DOE - Enter DOE distribution categories from the Standard Distribution for Unclassified Scientific and Technical Reports.
NASA - Leave blank.
NTIS - Leave blank.

Block 13. Abstract. Include a brief *(Maximum 200 words)* factual summary of the most significant information contained in the report.

Block 14. Subject Terms. Keywords or phrases identifying major subjects in the report.

Block 15. Number of Pages. Enter the total number of pages.

Block 16. Price Code. Enter appropriate price code *(NTIS only)*.

Blocks 17. - 19. Security Classifications. Self-explanatory. Enter U.S. Security Classification in accordance with U.S. Security Regulations (i.e., UNCLASSIFIED). If form contains classified information, stamp classification on the top and bottom of the page.

Block 20. Limitation of Abstract. This block must be completed to assign a limitation to the abstract. Enter either UL (unlimited) or SAR (same as report). An entry in this block is necessary if the abstract is to be limited. If blank, the abstract is assumed to be unlimited.